

INFORMATION TO USERS

This manuscript has been reproduced from the microfilm master. UMI films the text directly from the original or copy submitted. Thus, some thesis and dissertation copies are in typewriter face, while others may be from any type of computer printer.

The quality of this reproduction is dependent upon the quality of the copy submitted. Broken or indistinct print, colored or poor quality illustrations and photographs, print bleedthrough, substandard margins, and improper alignment can adversely affect reproduction.

In the unlikely event that the author did not send UMI a complete manuscript and there are missing pages, these will be noted. Also, if unauthorized copyright material had to be removed, a note will indicate the deletion.

Oversize materials (e.g., maps, drawings, charts) are reproduced by sectioning the original, beginning at the upper left-hand corner and continuing from left to right in equal sections with small overlaps. Each original is also photographed in one exposure and is included in reduced form at the back of the book.

Photographs included in the original manuscript have been reproduced xerographically in this copy. Higher quality 6" x 9" black and white photographic prints are available for any photographs or illustrations appearing in this copy for an additional charge. Contact UMI directly to order.

U·M·I

University Microfilms International
A Bell & Howell Information Company
300 North Zeeb Road, Ann Arbor, MI 48106-1346 USA
313/761-4700 800/521-0600

Order Number 9211550

Membrane deformation rate and geometry of subducting slabs

Chiao, Ling-Yun, Ph.D.

University of Washington, 1991

U·M·I
300 N. Zeeb Rd.
Ann Arbor, MI 48106



**Membrane Deformation Rate and Geometry of Subducting
Slabs**

by

Ling-Yun Chiao

A dissertation submitted in partial fulfillment
of the requirements for the degree of

Doctor of Philosophy

University of Washington

1991

Approved by _____

Kenneth C. Creager

(Chairperson of Supervisory Committee)

Program Authorized
to offer Degree _____

Geophysics Program

10/8/1991

Date _____

Doctoral Dissertation

In presenting this dissertation in partial fulfillment of the requirements for the Doctoral degree at the University of Washington, I agree that the Library shall make this copies freely available for inspection. I further agree that extensive copying of this dissertation is allowable only for scholarly purposes, consistent with "fair use" as prescribed in the U.S. Copyright Law. Requests for copying or reproduction of this dissertation may be referred to University Microfilms, 300 North Zeeb Road, Ann Arbor, Michigan 48106, to whom the author has granted "the right to reproduce and sell (a) copies of the Manuscript in microform and/or (b) printed copies of the manuscript made from microform."

Signature Longyun Chuan

Date 10/22/91

University of Washington

Abstract

Membrane Deformation Rate and Geometry of Subducting Slabs

By Ling-Yun Chiao

Chairperson of Supervisory Committee: Professor Kenneth C. Creager

Graduate Program in Geophysics

The subduction process forces the oceanic lithosphere to change its geometric configuration from a spherical shell to the geometry delineated by the Wadati-Benioff seismicity. This change induces lateral membrane deformation within the slab in addition to the bending deformation typically analyzed in two dimensional cross sections. Observations including the along-arc variations of slab geometry, seismic activity, and orientation of earthquake focal mechanisms suggest that this membrane deformation is an important mechanism in controlling the evolution of the subduction zone structure and seismic generation pattern. To quantify this type of slab deformation, we assume that subducting slabs behave like thin viscous sheets with either Newtonian or Power-Law rheology flowing into a mantle with significantly lower viscosity. A non-linear optimization scheme is developed to find the slab geometry and the subduction flow field minimizing the integrated total dissipation power by fixing boundary conditions constrained by the Wadati-Benioff seismicity and the relative plate convergence. The rationale behind this optimization is that since the subducted slab has strong resistance to membrane deformation and relatively little strength to respond to slab normal forces, finding the optimal configuration with the least amount of membrane deformation rate will thus provide insights on both the slab structure and the pattern of slab deformation. Experiments on the Cascadia subduction zone suggest that the proposed arch structure is

a natural consequence of the subducted slab responding to the concave-oceanward trench. The arch also provides a plausible explanation for the origin of the Olympic Mountains accretionary prism in the context of the *Critical Taper Theory*. The concentration of seismicity beneath the Puget Sound area may be the result of bending the already arched slab. The computed deformation rate is dominated by along-arc compression under Puget Sound and the peak compressional strain-rate is around $2 \times 10^{-16} \text{ sec}^{-1}$ which is comparable to the value estimated from the total intraplate seismic moment release during the last century. In both the Alaska-Aleutian and NW-Pacific subduction zones, preliminary experiments predict similar arch structures. Also, modelling results provide plausible explanations for along-arc variations of the deformation regime within slabs that are not resolvable by 2-D approaches.

Table of Contents

	Page
List of Figures	iv
List of Tables	viii
Chapter 1 Introduction	1
1.1 Shell effects and subduction process	1
1.2 Observations requiring a three-dimensional treatment	3
1.2.1 Arcuate shape of Island "Arcs"	3
1.2.2 Oceanward concave trench traces and slab arches	4
1.2.3 "Space Problem" and the "Table Cloth Analogy"	13
1.3 Recent efforts in quantifying slab membrane deformation	13
1.4 Motivation and preview of this study	17
Chapter 2 Theoretical formulation	21
2.1 Decomposition of membrane- and bending-deformation rate	24
2.2 Bending deformation in the simplified two-dimensional case	26
2.3 Membrane deformation rates: Forward Problem	29
2.3.1 Conceptual view of the membrane strain rate tensor	29
2.3.2 Gaussian Curvature	33
2.3.3 The projection operator	36
2.3.4 Mapping the 3-D problem to 2-D space	40
2.4 Membrane deformation rates: Inverse Problem	42
2.4.1 Integrated total Dissipation Power	42
2.4.2 Inverting for flow field only	44
2.4.2.a Linear inversion for the Newtonian Rheology	44
2.4.2.b Nonlinear inversion for the Power-law Rheology	45
2.4.3 Inverting for both the flow field and slab geometry	45
2.4.3.a The nonlinear inversion	45
. <i>Creeping vs. Jumping iteration</i>	46
. <i>Damping vs. Smoothing regularization</i> ..	46
2.4.3.b Parameterization and the Finite Element Method .	48
. <i>Linear C^0 element</i>	49
. <i>Quadratic C^0 element</i>	51
. <i>Clough-Tocher cubic C^1 element</i>	51

2.4.3.c Setting up the inversion	52
2.4.4 The <i>Simple</i> experiment	54
Chapter 3 Cascadia Subduction Zone	61
3.1 Tectonic framework and observations	61
3.2 Effect of the backward-curved trench	69
3.2.a Inverting for the optimal flow field: The <i>Constant-Dip</i> experiment	69
3.2.b The full Inversion: The <i>Shallow-Dip experiment</i>	69
3.3 Effect of bending an arch: The <i>Arch-Bending</i> experiment	77
3.4 Incorporating information of a steeper secondary bend: The <i>Steep-</i> <i>Dip</i> experiment	78
3.5 Conclusions and Discussions	82
Chapter 4 Preliminary experiments on Alaska-Aleutian and NW- Pacific subduction zones	84
4.1 Alaska-Aleutian Subduction Zone	84
4.1.1 Slab seismicity, slab geometry and focal mechanisms	84
4.1.2 Previous models	87
4.1.3 Modeling efforts in this study	89
4.1.3a The <i>Constant-dip</i> and <i>Contionuous-slab</i> experiments	89
4.1.3b Alaska Zone: The <i>Alaska</i> experiment	92
4.1.3c Aleutian Zone: The <i>Aleutian</i> experiment	95
4.2 NW-Pacific Subduction Zone	99
4.2.1 Slab seismicity and slab geometry	99
4.2.2 Deformation regime revealed from focal mechanisms	103
4.2.3 Previous modelling works	103
4.2.4 Modeling efforts in this study	107
Chapter 5 Summary and Discussions	110
Bibliography	115
Appendix A On the shear deformation parallel to the slab surface	124
Appendix B Notes on non-linear optimization	128
Appendix C Mesh generation for curved trench	136
Appendix D Computing the Hessian matrix α^e and the gradient vector β^e	139

List of Figures

	Page
Figure 1.1 Trench configurations in the Circum-Pacific region	5
Figure 1.2 Frank's "Ping-Pong Ball" model	6
Figure 1.3 Qualitative deformation regimes corresponding to trench shapes .	7
Figure 1.4 Along-arc variation of slab geometry suggested by Wadati-Benioff seismicity of the NW-Pacific Subduction Zone	8
Figure 1.5 Examples of arch structure associated with concave-oceanward shape of the trench. Depth contours for Kuril-Japan-Izu region; Cascadia Subduction Zone; New Britain-Solomon Slab; Alaska-Wrangell Subduction Zone and the Peru-Chile Subduction Zone .	10
Figure 1.6 The "space problem" of Cascadia Subduction Zone	14
Figure 1.7 Map view projection of principal axes of 14 CMT solutions below 70 km in the Alaska-Aleutian Subduction Zone	15
Figure 2.1 Local slab-normal coordinate	25
Figure 2.2 Sample slab shapes in 2-D cross section, interpolated by "Minimum curvature" and "Minimum change of curvature"	30
Figure 2.3 Mapping a local patch of particles into a different geometric configuration by the flow field	32
Figure 2.4 A surface flow $\mathbf{u}(x,y,z)$ defined on the non-Euclidean surface $z=z(x,y)$ embedded in the three-dimensional space can be rewritten as a function $\mathbf{u}^*(x,y)$ of x,y only	41
Figure 2.5 Continuity across element boundaries in Finite Element Method ..	49
Figure 2.6 Definition of local area coordinate system	50
Figure 2.7 Nodes location of the quadratic C^0 element	51
Figure 2.8 Nodal variables of the C^1 Clough-Tocher element	52
Figure 2.9 (a) Model surface geometry of the <i>Simple</i> experiment composed by overlying a small round hill on top of a spherical cap. Forward computation for (b) orientations of principal axes of the membrane strain-rates, and (c) distribution of the effective strain rate	57

Figure 2.10	Optimal flow field, distribution of effective strain-rates and orientations of principal axes of membrane deformation obtained by invert for flow field only, Newtonian rheology for the <i>Simple</i> experiment	58
Figure 2.11	Optimal flow field, distribution of effective strain-rates and orientations of principal axes of membrane deformation obtained by invert for flow field only, Power-Law rheology ($n=100000$) for the <i>Simple</i> experiment	59
Figure 2.12	The <i>Simple</i> experiment; full inversion involving both the flow field and the model geometry: the starting model, 15th iteration and 25th iteration	60
Figure 3.1	Tectonic framework of Cascadia Subduction Zone and the simplified Washington coastal geology	63
Figure 3.2	Slab seismicity of the Cascadia Subduction Zone and the proposed arch structure	64
Figure 3.3	Total seismic moment release within the subducting plate of this century in the Cascadia Subduction Zone	65
Figure 3.4	Cross sections of the shallow structure of the Cascadia slab underneath Vancouver Island and the Olympic Mountains	65
Figure 3.5	Cross section of slab seismicity beneath Olympic Peninsula-Puget Sound	67
Figure 3.6	The <i>Constant-Dip</i> experiment of Cascadia Subduction Zone. Model geometry and deformation regime, inversion on flow field only	70
Figure 3.7	The <i>Shallow-Dip I</i> experiment of Cascadia Subduction Zone. Model geometry and deformation regime, full inversion with Newtonian rheology	72
Figure 3.8	The <i>Shallow-Dip II</i> experiment of Cascadia Subduction Zone. Model geometry and deformation regime, full inversion with Power-Law rheology	73
Figure 3.9	Perspective view of the shallow structure of the Cascadia slab, and the comparison between the surface projection of the predicted structure and the regional volcanic trend	74

Figure 3.10	The <i>Arch-Bending</i> experiments on the effects of bending an already arched, non-flat surface	79
Figure 3.11	The <i>Steep-Dip</i> experiment of Cascadia Subduction Zone. Model geometry and deformation regime, full inversion	81
Figure 4.1	Tectonic framework and the seismicity of the Alaska-Aleutian Subduction Zone	85
Figure 4.2	Seismic moment release of the Alaska-Aleutian Subduction Zone	86
Figure 4.3	Model geometry, particle path and accumulated lateral strain of Aleutian Subduction Zone, result from Burbach and Frolich [1986]	88
Figure 4.4	Model geometry, particle path and deformation regime of Aleutian Subduction Zone, result of Creager and Boyd [1991]	90
Figure 4.5	The <i>Constant-Dip</i> experiment in Alaska-Aleutian Subduction Zone: Model geometry, available CMT solutions and deformation regime, inversion for flow field only	93
Figure 4.6	The <i>Continuous-Slab</i> experiment in Alaska-Aleutian Subduction Zone: Model geometry and deformation regime, full inversion ...	94
Figure 4.7	The <i>Alaska</i> experiment: Model geometry, available CMT solutions and deformation regime, inversion for flow field only ..	97
Figure 4.8	The <i>Aleutian</i> experiment: Model geometry, available CMT solutions and deformation regime, inversion for flow field only ..	98
Figure 4.9	Three-dimensional perspective view of the geometry of the subducted slab of Kuril-Japan-Izu-Bonin system and Bonin-Mariana system. [reproduced from Chiu et al., 1991]	100
Figure 4.10	Seismic moment release and the inferred slab structure in the NW-Pacific subduction zones	101
Figure 4.11	Map view of orientations of principal P and T axes (least and most compressive axes) of the CMT solutions in NW-Pacific	104
Figure 4.12	Along arc variations of the P-T transition depth within the slab in the NW-Pacific Subduction Zone, [after Zhou, 1990]	105
Figure 4.13	Modelling results from Burbach and Frolich's (1986) study showing the seismicity, lateral deformation and selected focal mechanisms in the NW-Pacific subduction zones	106

Figure 4.14	NW-Pacific optimization experiment. Model geometry, available CMT solutions and deformation regime, full inversion for flow field only	109
Figure A.1	An ideal slab with viscosity μ_1 is falling vertically into the surrounding mantle with viscosity μ_2	124
Figure A.2	Viscosity ratio of slab versus the ambient mantle	126
Figure B.1	Zigzag path of the steepest descent direction (the bold line) on a quadratic function	130
Figure C.1	Configuration and parameters used in mapping a curved boundary into a straight one	136
Figure C.2	Mapping between the curved x-y domain and the straight d-s domain	137

List of Tables

	Page
Table 1.1 Earthquakes with magnitude 6 or greater that are inferred to be within the subducted Cascadia slab in this century	62

Acknowledgements

Working on this thesis project has been a rewarding process to me mainly because of my advisor Dr. Ken Creager. I would like to thank him not only for the patient guidance and support, but also for the inspiration from his broad interest and enthusiasm toward the Geophysical Science. I would also like to acknowledge Drs. John Booker, Robert Crosson and Bruce Finlayson for serving as my supervisory committee and offering educational suggestions and comments. Dr. Clive Lister helped me in many ways in the first two years when I first got here. My fellow graduate students and office mates Dai McClurg, David Carol, John Vandecar, John Firestone, Tian-Shan Zhang, Yaqi Lee, Hua Hu and Tom Mcsweeney have provided stimulating discussions and pleasant working environment. Discussions with Dr. Roger Delinger have been useful and inspiring. I am also grateful for the professional expertise and kindness offered by the faculty and staff of the Geophysics Program. Special thanks go to my fellow student and good friend Tom Boodle for his precious friendship. Finally, were it not for the tolerance and constant support from my wife and dear friend Lu Hsiao, I would not be able to enjoy studying here this much. This work was supported by U.S. Geological Survey contracts 14-08-001-G-1390 and NSF grant EAR-8917231.

Chapter 1 Introduction

1.1 Shell effects and subduction process

As it spreads out from the mid-ocean ridge and gradually cools down, the oceanic lithosphere formed near the surface of Earth becomes part of a spherical shell. To a good approximation, these spherical shells are observed to form large "plates" where relative motions can be described by rigid body rotations. The paucity of intra-plate seismicity suggests that the internal deformation of the lithospheric plates is generally small.

The lithosphere must, however, deform as it subducts back into the deep mantle. First, the lithosphere must bend and unbend. Bending has been analyzed in detail using a variety of lithospheric rheologies, but these analyses have considered only two-dimensional vertical cross sections, and assumed no variation of geometry in the along-arc direction. This simplification had enabled researchers to examine the evolution and origin of the ocean basin, outer rise, and trench topography [e.g. Caldwell et al., 1976; Turcotte, 1979; Melosh and Raefsky, 1979] and also the state of stress of the subducted slab [e.g. Hanks, 1971; Chapple and Forsyth, 1979; Tsukahara, 1980; Kawakatsu, 1986]. Understanding the deformation regime in the subducted slab is of primary geophysical concern since it is directly related to slab earthquakes and the evolution of arc structures. The two-dimensional approach not only helped in providing insights on the bending mechanism in the shallow part of the subduction, it also leads to the well accepted concept that even in the intermediate and deep depth, the slab behaves like a stress guide that transfers the gravitational pulling and viscous drag as either down-dip extension or down-dip compression [Isacks and Molnar, 1971]. More complete two-dimensional dynamical calculations have led to a greater understanding of stresses and strain rates within subducting slabs owing to the slab's anomalous rheology, negative buoyancy, and viscous drag [eg. Gurnis and Hager, 1988; Kemp and Bird, 1989].

The mechanical thickness of slabs is usually a few tens of kilometers [e.g. Turcotte, 1979; McNutt, 1984], which is small compared to their lateral dimensions of a thousand or so kilometers. Also, because slabs are cold relative to the surrounding mantle, the effective viscosity of the slab is probably at least a few orders of magnitude

higher than the surrounding warm mantle. For those two reasons, Creager and Boyd [1991] argued that slabs should behave like a thin sheet, in the sense that they have strong resistance to in-plane (or membrane) deformation, but relatively little strength for slab-normal forces. As delineated by Wadati-Benioff seismicity, the shapes of the subducted slabs are quite different from the spherical shell of oceanic lithosphere prior to subduction. Simple experiments like bending a sheet of corrugated metal or flattening out a spherical shell tell us that changes of internal geometric configuration of a three-dimensional surface cannot occur arbitrarily without introducing membrane deformation. This implies that the subducting slab must suffer a significant amount of membrane deformation and contortion in addition to the bending deformation as the spherical oceanic lithosphere is forced into the geometry of the subducted slab. In dealing with the geometry of a non-Euclidean surface as the slab structure, the *Gaussian Curvature* concept from the theory of *Differential Geometry* is very useful in examining the deformation imposed by geometric constrains. This concept will be discussed in more detail in chapter 2. In short, it points out that conservation of Gaussian Curvature, product of the two principal curvatures, during a change of configuration is a necessary condition for a general surface structure to be free from membrane deformation. Recognizing the implications of this concept on subduction systems, Bevis [1986] pointed out that all subduction geometries violate this condition, so all slabs suffer membrane deformation. There are dozens of studies on the kinematics and dynamics of subduction which consider only two-dimensional cross sections. Using this assumption, the curvature of any slab surface vanishes in the along-arc direction. Thus, the Gaussian curvature is zero everywhere, and there is no need for membrane deformation in either the along-arc or down-dip direction. Of course membrane deformation in the down-dip direction, caused by the dynamics, are the kinematic equivalent of down-dip compressive and extensional stresses so often discussed in the literature. One of the primary goals of this dissertation is to analyze the minimum amount of membrane deformation rate associated with three-dimensional flow corresponding to several subduction geometries, and to demonstrate that both focal mechanism orientations and slab geometries can often be explained by considering these three-dimensional constrains.

An interesting argument based on the concept of Gaussian Curvature is that the success of the theory of Plate Tectonics resides mainly on the fact that we have a nearly

spherical planet, so the Gaussian curvature of Earth's surface is nearly constant. This allows plates to move in a rotational fashion with respect to Euler poles without significant intra-plate deformation. In fact, since Earth is slightly elliptical with an ellipticity of $\epsilon=0.00335$, it leads to speculations that large scale plate motion in the long term may actually induce accumulations of intra-plate straining. Assuming plates behave elastically, Turcotte [1973] estimated membrane stresses of the order of kilobars associated with the membrane deformation induced by change in latitude when plates move about on the surface of the earth. Freeth [1980] also argued that these stresses generated by membrane tectonics may be partially responsible for the initiation of intra-continental rifts. Taking a Young's modulus of 1.72×10^{12} dynes/cm² used in Turcotte's calculation, this would translate into membrane strain on the orders of 10^{-2} . Since a significant change of latitude requires about 10^8 years, it means a strain rate on the order of 10^{-18} sec⁻¹, the deformation rates are thus small and may be taken up by a slow creeping mechanism. The changes of geometric configuration in a subduction zone are more dramatic with a typical strain rate of 10^{-15} sec⁻¹ (Bevis, 1988; Creager and Boyd, 1991), the need to better understand and quantify this type of deformation and its impact on subduction process is then obvious. However, unlike the oblate spheroidal surface of the earth, the subducted slab usually does not have a simple regular geometrical shape. This makes the attempt of quantifying this deformation extremely difficult.

1.2 Observations requiring a three-dimensional treatment

1.2.1 Arcuate shape of Island Arc system

Figure 1.1 shows that the trenches of major subduction zones usually take a concave-oceanward arcuate shape. The origin of this shape has been argued by different hypothesis, e.g the indentation of seamounts on the edges of the trench [Vogt, 1972; Hsui, 1988], although the correlation of cusps between different arcs with the presence of seamounts or other aseismic ridge structures is not always obvious. It is generally believed that the sphericity of the earth plays a role in the forming of such shapes. A simple "Ping-Pong Ball" model [Frank, 1968; see Figure 1.2] accounts for the sphericity

of Earth by pointing out that the oceanic lithosphere can hold its integrity and conserve area if its subducted shape is similar to an indented ping-pong ball. This model predicts that the dip angle of the subducted slab is twice the radius of curvature of the trench, and provides a simple explanation for the general arcuate shape of most oceanic trench-arc systems. Intriguing as it may be, this model is not quite realistic. First, the predicted relationship between the subduction dip angle and the radius of curvature of the trench is seldom met by real subduction systems. Secondly, this model has the slab going to shallower dips with increasing depth, which is nearly never observed. Perhaps the most serious problem with this simple model is the discontinuous dip change right at the trench, which is not only inconsistent with observations but also would generate an unacceptable amount of deformation regardless of what kind of rheology the slab might have. Bevis [1986] points out that this model is actually a particular example that conserves the Gaussian curvature. Several studies in the 70's [Stroback, 1973; Larvie, 1975; Le pichon, 1978; Tovish and Schubert, 1978] attempted to further elaborate this concept, but were unable to quantify the deformation generated within the slab as a result of non-ideal configurations. These models, however, do provide general qualitative pictures of what kind of deformation to expect within the subducted slab given the shape of the trench and the dip angle of the subduction zone (Figure 1.3). Intriguing observations like along-arc extension revealed from intermediate-focus-earthquake focal mechanisms in the central Aleutians and the Mariana slab are two examples showing the effect of lateral membrane deformation within the slab subducting with dip angles that are too steep.

1.2.2 Oceanward concave trench traces and slab arches and cusps

With the general concave landward trench configuration in mind, an interesting comparison is then to examine the slab configuration across "cusps" between different arcs. Arc-arc-junctions form cusps with tight oceanward concave curvature. Invariably the slab dip landward of these cusps is anomalously shallow, and forms an arch structure. For example, shown in Figure 1.4, the slab dip angles of the NW-Pacific subduction zones change gradually from approximately 55° in the Kuril-Kamchatka subduction zone to nearly 30° in the Japan zone and then gets steeper again to Izu-Bonin and eventually

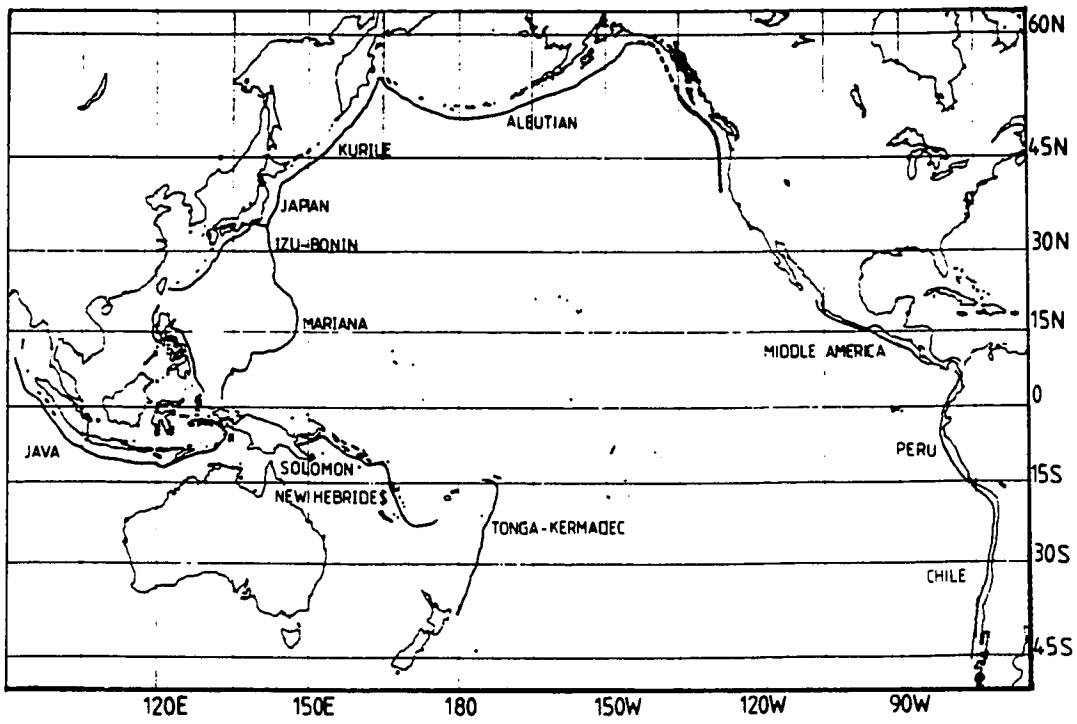


Figure 1.1 Trench configuration of subduction zones in the Circum-Pacific region.

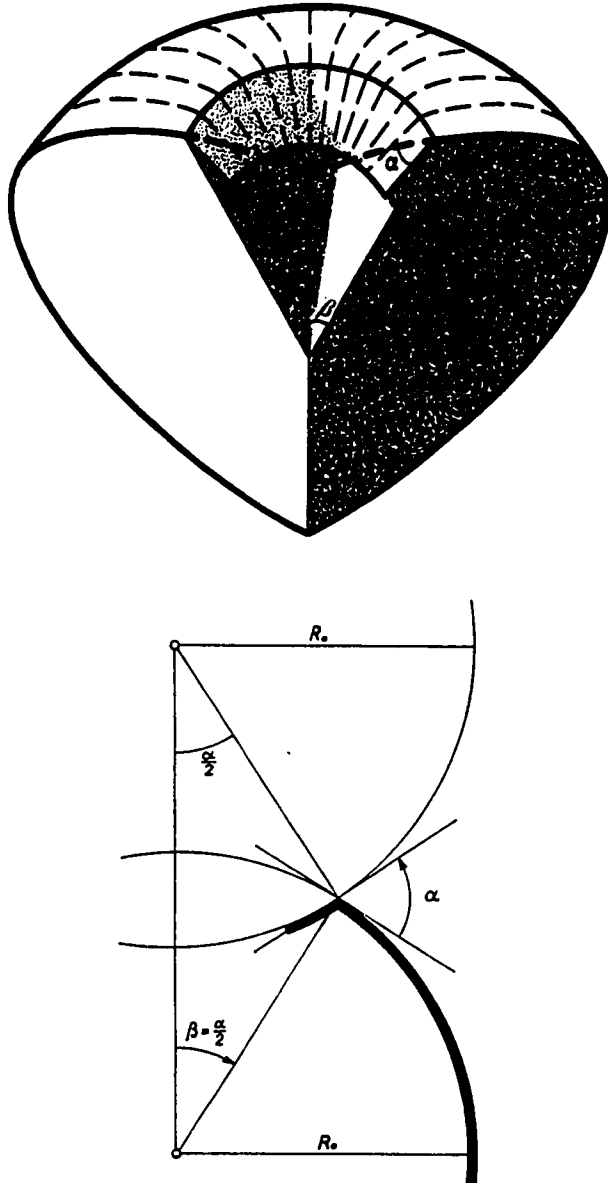


Figure 1.2 Frank's "Ping-Pong Ball" model. The above diagram shows a cut-away view of the earth at an island arc showing the descending slab [after Tovish and Schubert, 1978]. The lower diagram is after Strobach [1973] where the heavy line represents the oceanic plate with down bent slab. It shows the geometric relation, that the dip angle of the subducted slab (α) is twice the radius of curvature of the trench measured in radians (β).

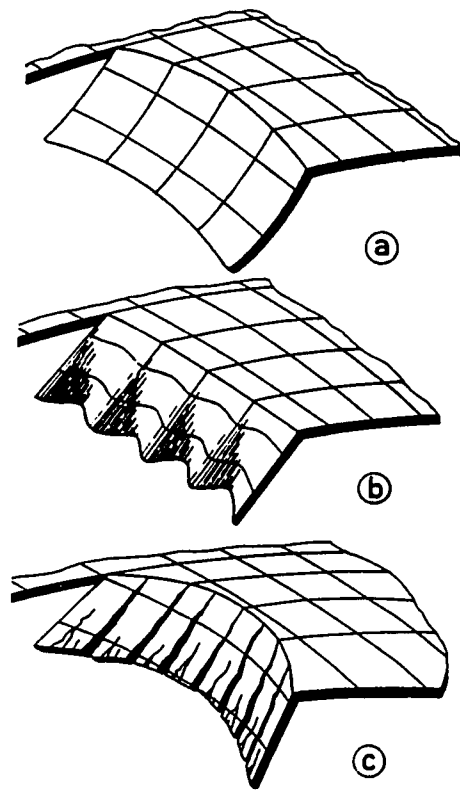


Figure 1.3 Qualitative deformation regimes corresponding to different trench shapes. (a) Frank's strain free configuration. (b) The curvature of the trench is not tight enough, the slab is thus in along-arc compression. (c) The curvature of the trench is too tight, the slab is in along-arc extension [after Stroback, 1973].

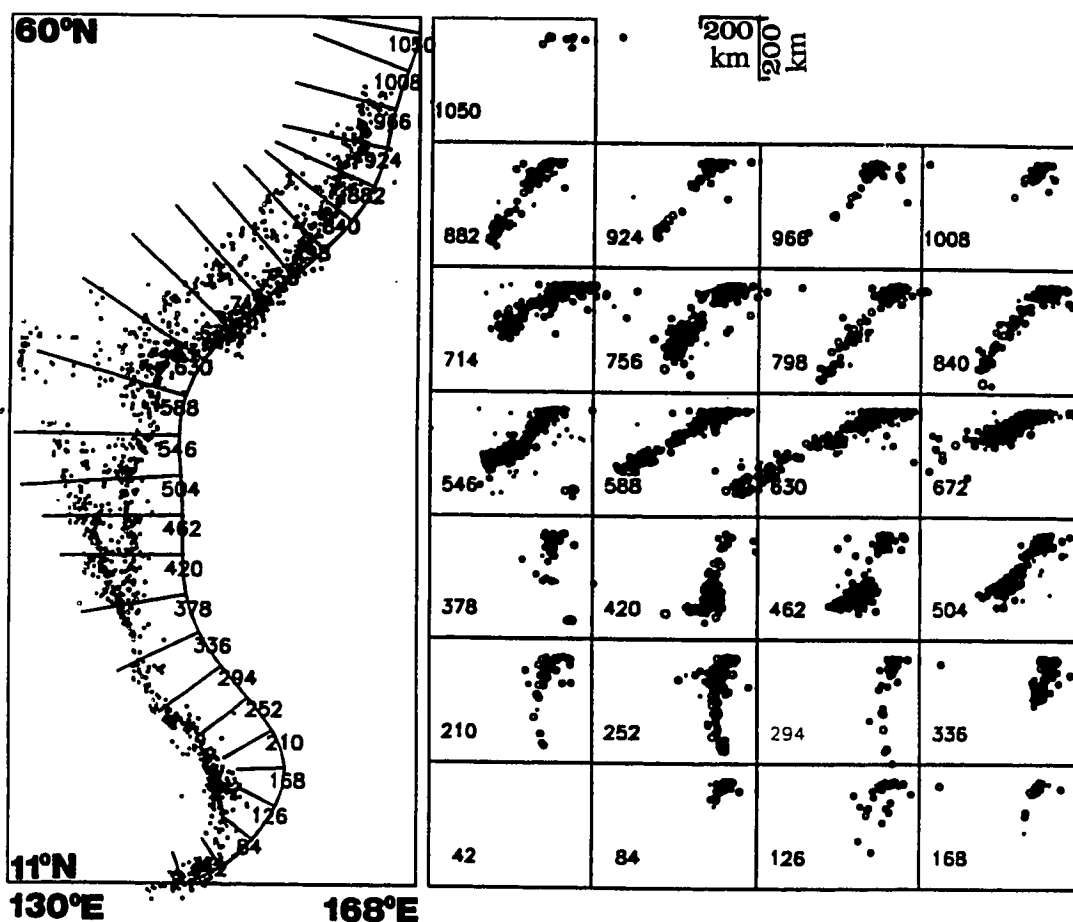


Figure 1.4 Intermediate- and deep-seismicity of the NW-Pacific subduction zones. Cross-sectional views of the seismicity (ISC, 1964-1984, below 70 km) on the right are constructed by dividing the entire subduction zone into small rectangular blocks oriented normal to the trench, seismicity within each block is then projected to the central profile of that block. Notice the gradual variation of the slab dip angle from nearly vertical (Mariana, profile 210, 252) to 30° (Hokkaido corner, profile 588, 630) and then to $\sim 55^{\circ}$ (Kuril, profile 840, 882, 924).

becomes vertical in the Mariana region. When viewed as a series of isolated cross-sections, there are no obvious variations in subduction parameters such as age of oceanic crust, convergence rates, obliqueness of subduction or type of overriding plate, that would explain these systematic changes in dip. Figure 1.5a shows the inferred slab depth contours [after Yamaoka and Fuako, 1987] underneath the Japan area. Notice that both the transition from Kuril to Japan (the Hokaido corner), and the transition from Japan to Izu-Bonin defines two sharp concave oceanward bends in the trench. Coincident with these two close bends the slab has much shallower dip as shown from both the cross-sectional view of seismicity in Figure 1.4, and the inferred depth contour in Figure 1.5a. In the Cascadia subduction zone, a similar arching within the subducted slab associated with a oceanward concave trench shape had been proposed by examining seismic evidence (Figure 1.5b, [after Crosson and Owens, 1987]). Other examples include New Britain-Solomon subduction zone (Figure 1.5c, [after Yamaoka and Fuako, 1987]) and the Alaska Subduction Zone. With a clear oceanward-concave trench wrapping around Gulf of Alaska, the subducted slab between the Wrangell Slab to the east and the Aleutian Slab further west, the Alaska slab has a shallower slab dip (Figure 1.5d, [after Page et al., 1989]). One exception, however, is the Peru-Chile Slab, where the shallow structure has a steeper dip underneath the region with an oceanward concave trench before it shoals to a relatively shallower dip again (Figure 1.5e, [after Isacks and Barazangi, 1977]). These possible arch structures, that are usually coincident with the axes of the concave-oceanward shape of the trench or cusps at the arc-arc junction, had been qualitatively attributed to the buckling of the subducted slab that is subjected to along-arc compression imposed by the shape of the trench.

All these observations mentioned above are directly related to the relationships between membrane deformation rates of a relatively thin slab surface and the geometric configuration of the surface. Due to the large amount of centroid-moment tensor (CMT) solutions available in recent years [Dziewonski et al., 1981; Dziewonski and Woodhouse, 1983; Giardini, 1984; and routinely published solutions in issues of *Physics of the Earth and Planetary Interiors* since 1983], focal mechanism orientations of slab earthquakes have been systematically examined to understand the deformation regime within slabs [e.g. Vassiliou and Hager, 1988; Zhou, 1990; Lundgren and Giardini, 1990]. Although most of these studies confirmed down-dip compression in the

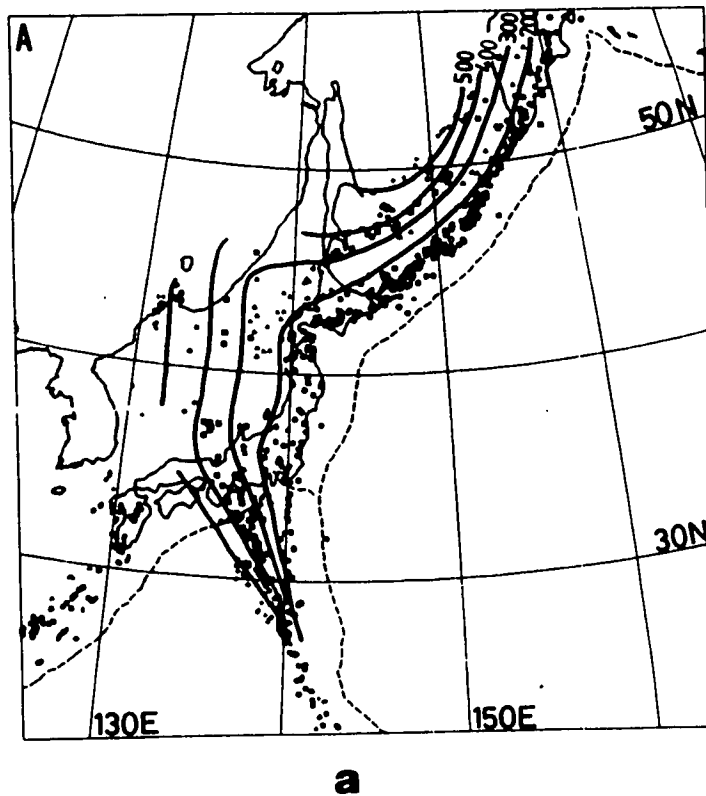


Figure 1.5 Examples of arch structure associated with concave-oceanward shape of the trench. Depth contours of subducted slabs inferred from slab earthquakes for (a) Kuril-Japan-Izu region [after Yamaoka and Fuako, 1987]; (b) Cascadia Subduction Zone [after Crosson and Owens, 1987]; (c) New Britain-Solomon Subduction Zone [after Yamaoka and Fuako, 1987]; (d) Alaska-Wrengell Subduction Zone [after Page et al., 1989]; and (e) Peru-Chile Slab [after Isacks and Barazangi, 1977].

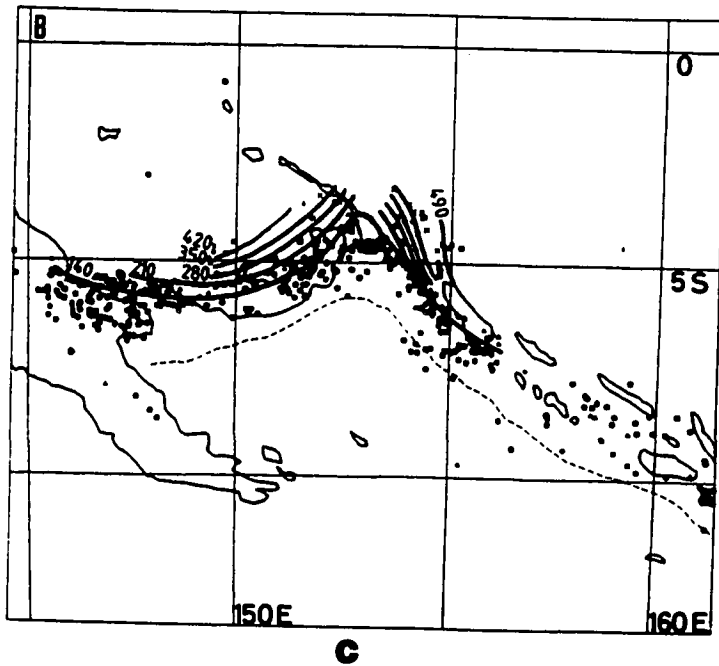
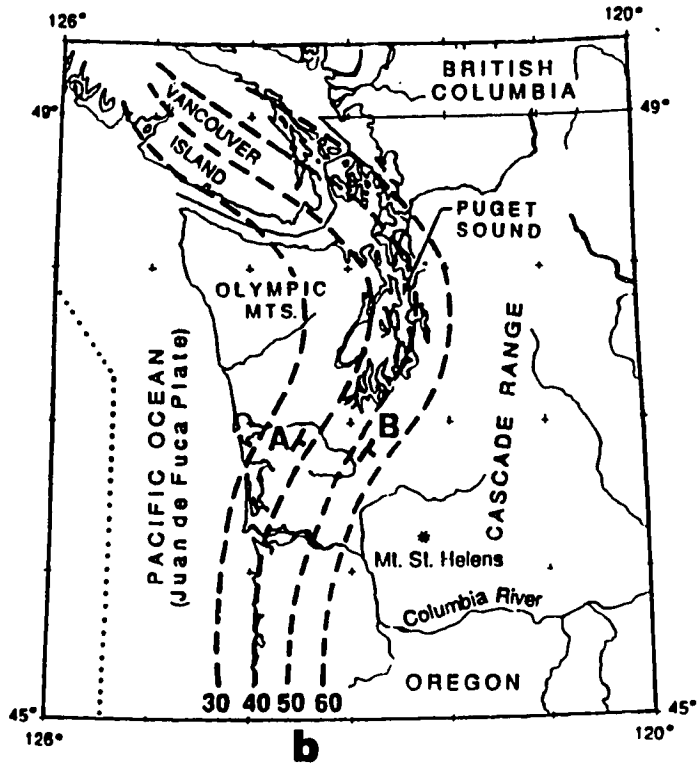
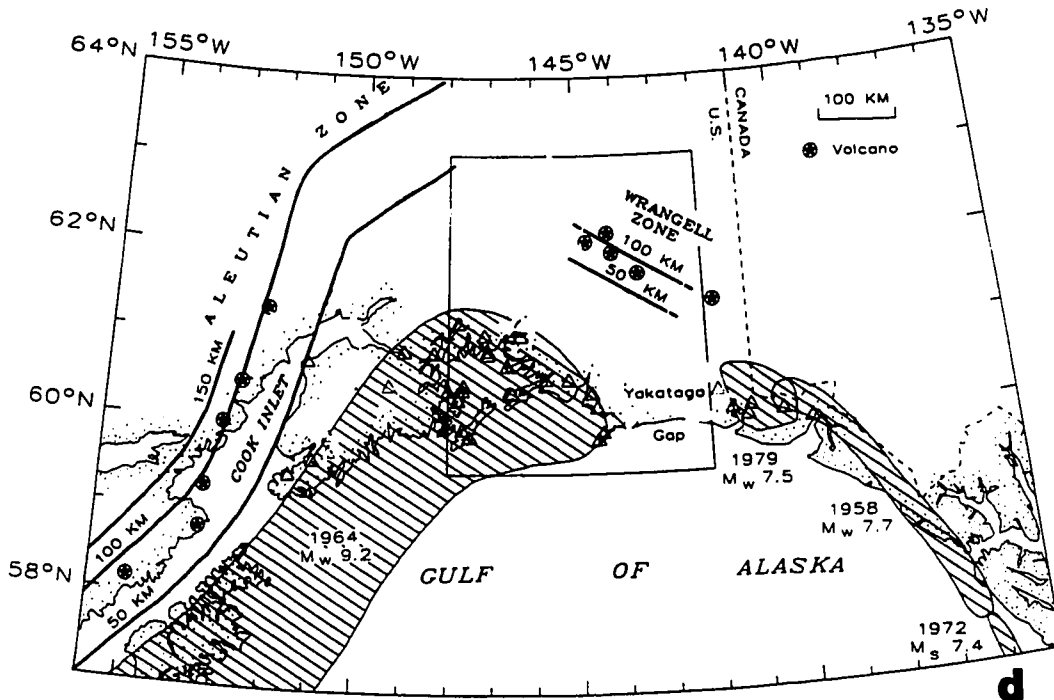
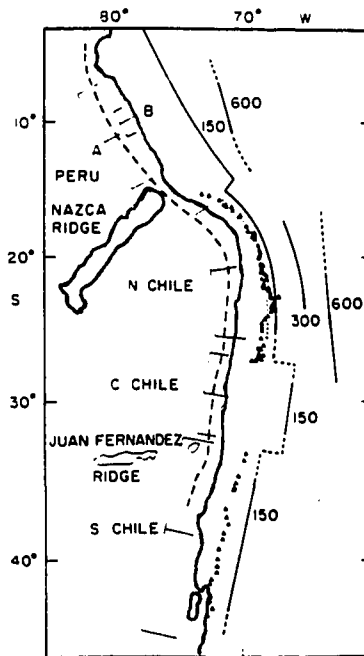


Figure 1.5 (Continued)



d



e

Figure 1.5 (Continued)

slab at depths below 300 km, more and more interesting patterns of lateral variations have been observed. In the Alaska-Aleutian subduction zone, we plot the available CMT solutions for slab earthquakes below 70 km (Figure 1.7). The systematic change from along-arc extension in the central Aleutians to mostly along-arc compression in eastern Alaska is quite consistent when it is put in the context of lateral membrane deformation. Noticeably, this observation is beyond the resolution of the conventional two-dimensional model for examining the deformation regime within subducting slabs.

1.2.3 Space Problem and the Table Cloth Analogy

Another way to think about this type of possible deformation of the subducted slab imposed by geometric constrains had been addressed by Rogers [1983]. In his extensive study of the seismotectonics of Cascadia Subduction Zone, he noticed a *space problem* that because of an unusual concave oceanward bend in the trench of this subduction zone, there is not enough room for the subducted slab material to fit into while subducting (Figure 1.6). In trying to accommodate this, the slab would experience along-strike compression and possibly some kind of contortion in order to reduce this deformation. An easier way to visualize this problem is the *Table Cloth Analogy* by noticing the folds of a table cloth hanging over the corner of a table. Note that the folds can be removed by pulling the table cloth away from the table corner to give it a shallow dip or arch off the corner.

1.3 Recent efforts in quantifying slab membrane deformation

As mentioned earlier, while the two-dimensional idealization of subduction zones might be appropriate for studying bending deformation in the shallower depth, it is not capable of examining the possible membrane deformation imposed by the geometric constrains. The Gaussian Curvature is a good indication of whether this internal deformation is necessary, but it lacks the power of actually quantifying this deformation. Recognizing the importance of these shell effects, Yamaoka et al. [1986] suggest the use of the term "shell tectonics" instead of "plate tectonics". In exploring the three

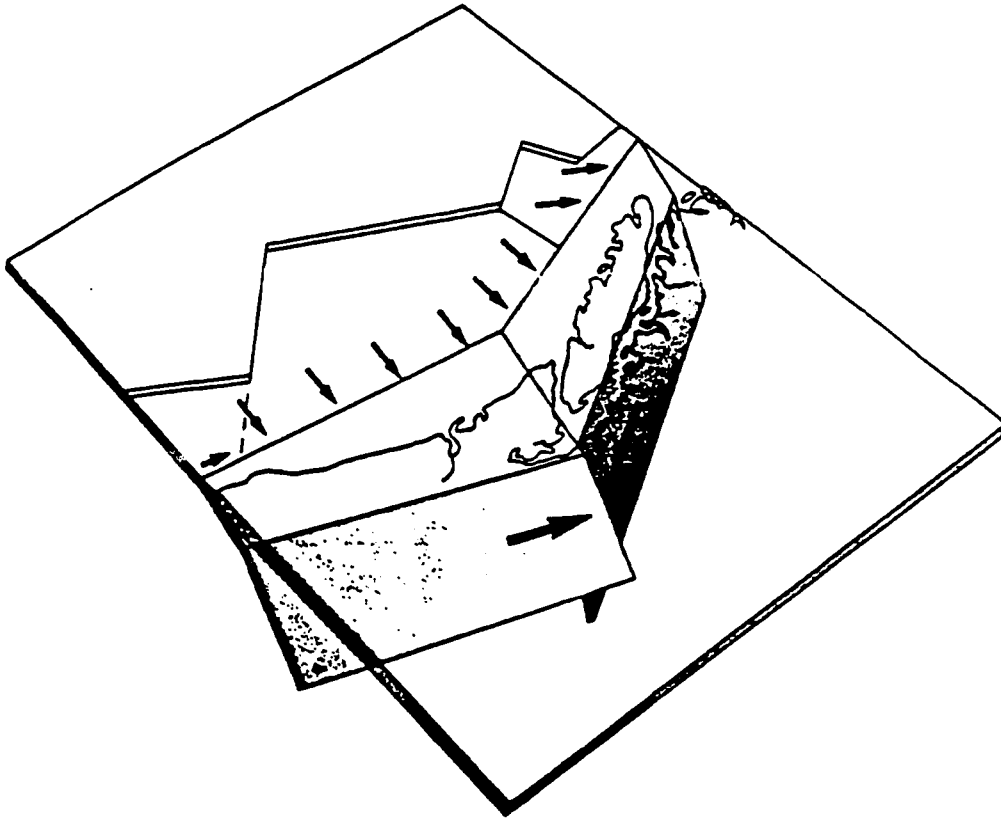


Figure 1.6 Roger's [1983] "Space Problem" of the Cascadia Subduction Zone points out that there are not enough room under this subduction system for the slab material to fit in.

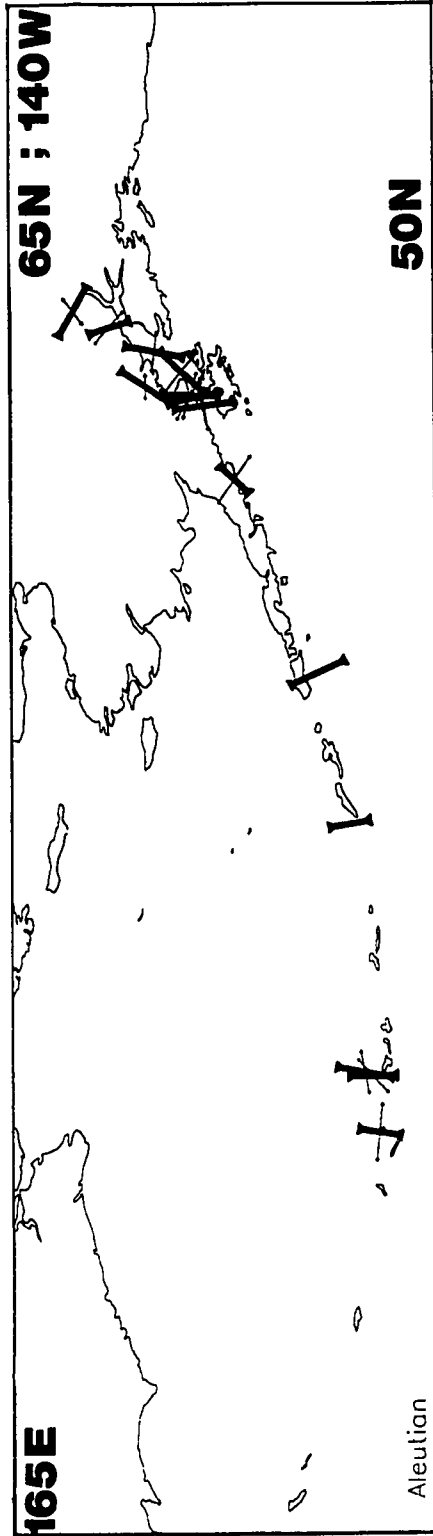


Figure 1.7 Map view projections of 14 CMT solutions (1977-1986) below depth 70 km in the Alaska-Aleutian Subduction Zone. Thick bars with arrows pointing inward are compressional axes while thin line segments bounded by outward pointing arrows are extensional axes. Notice that the three events in the central Aleutians have the compressional axes normal to the trench, and are in along-arc extension. The nine events in the Alaska region, however, are mostly in along-arc compression. The transition occurs near the Shumagin Islands where the two events have their null axes along arc.

dimensional nature of the subduction process and quantifying membrane deformation of the subducting slab, they use plaster to construct miniature model shapes of Wadati-Benioff zones by using International Seismological Center (ISC) earthquake locations. Oceanic lithosphere is then simulated by an inextensible spherical shell made of polyvinyl chloride resin. They perform analog experiments by forcing the spherical shell to fit the miniature of the Wadati-Benioff zone. They find that while most of the Wadati-Benioff zone shapes can be fit reasonably well without significant membrane deformation, there are regions of poor fit where tearing of the spherical shell or large membrane strains are needed to achieve an acceptable fit. Following this analog experiment, they use a finite element code to perform numerical experiments in order to examine the buckling of an open spherical shell under end loading and hypothesize that a buckling mechanism is responsible for forming the cusps at arc-arc junctions [Yamako and Fuako, 1987].

Pioneer work by Burbach and Frohlich [1986] adopted a quite different approach. In their inspiring study, they devised a simple algorithm to track the particle paths of subduction processes. First, they use Wadati-Benioff seismicity from ISC bulletins to define a smooth surface and thus get the local slab dips. Secondly, they define the flow field representing the subduction process by letting the velocity vector prior to subduction be consistent with the relative plate convergence. For a particle at the trench, they rotate the particle velocity vector through the local slab dip about the trench strike direction. Using this scheme, they estimate along-arc strain from the difference between separation distances of two neighboring particles at the trench and between the same two particles after 10 million years of subduction. Their results indicate that the observed geometry of most subduction zones involve relatively little lateral strain which is consistent with Yamaoka et al.'s experiment. But there are places like the western Aleutians, where the accumulated strain is as high as 50%.

Both of these two studies suggest that, first of all, although no observed subduction zone has the ideal strain free configuration predicted by Frank's model, there is actually a wide range of geometries with relatively small strain and that most subduction zones seem to fall in one of these configurations. Secondly, a lot of the previously proposed segmentations of subducted slabs, with different Wadati-Benioff

zone geometries or seismicity patterns, are most likely features of continuous contortion rather than being separated by tears or hinge faultings.

In the study of the geometry of Aleutian Subduction Zone, Creager and Boyd [1991] presented a method of quantifying this type of in-plane deformation by utilizing an optimization principle. They first constrain the slab geometry by local seismic array data and residual sphere analysis. Assuming the slab behaves similar to a thin viscous sheet, they set the surface flow field representing the slab motion to be consistent with the relative plate motion on the surface of the earth and adjust the flow field representing the motion of the subducted slab to go through the fixed slab geometry and at the same time minimize the in-plane deformation. They predict along-arc stretching deformation in the Aleutians and a maximum strain of 10% in the Central Aleutians, each of which are consistent with seismic observations. Also, their calculated strain rates in the Western Aleutians are ten times smaller than those calculated by Burbach and Frohlich.

To summarize these previous works: Bevis' [1986] Gaussian Curvature argument indicates that all slabs have to suffer a certain amount of membrane deformation from the subduction process, although the Gaussian Curvature criteria is not capable of quantifying how much that membrane deformation might be. Both the analog fitting experiment of Yamaoka et. al [1986] and Burbach and Frohlich's [1986] algorithm implies most of the previously proposed tears in slabs are possibly continuous, contorted features. Also, slabs have strong resistance to membrane deformation and seem to be able to find configurations with relatively small lateral straining. Creager and Boyd's [1991] study is an improvement of Burbach and Frohlich's algorithm in that they consider more realistic slab geometry, and invert for the flow field which minimizes in-plane deformation rate, whereas Burbach and Frohlich specified the flow field a priori and consider geometries in which a particle changes dip abruptly at the trench and then subducts 10 my at that dip.

1.4 Motivation and preview of this study

This study is primarily motivated by the non-uniformly distributed patterns of various kind of subduction related features, i.e. the along-strike variations of the

geometry of the subducted slab, especially the arch structures generally associated with the concave-oceanward shape of the trenches, the pattern of intra-slab seismic activity and their correspondence with the shape of the trench. Based on the same philosophy as in Creager and Boyd's study [1991] we are going to quantify the least amount of membrane deformation rates required by the geometric and kinematic constrains and examine the pattern of membrane strain rates distributed within the slab. But instead of using the Lagrangian description of the flow field in their work, we reformulate the problem using the Eulerian description implemented by the Finite Element interpolation so that the flow would be able to anticipate the effects of the slab geometry in the down dip direction just as it has memory of the configuration above. Also, instead of fixing the slab geometry completely, except at places where we have accurate constrains of slab geometry (mainly by Wadati-Benioff seismicity) we let the slab geometry adjust itself along with the flow field so that we can study how the slab geometry responds to the shape of the trench. In short, the main objectives of this study are:

(1). To formulate a quantitative measure of membrane deformation rates imposed by geometric and kinematic constrains associated with subduction processes.

(2). To fine tune the flow field and the slab geometry subject to constraints setup by known plate motion, Wadati-Benioff seismicity and other geophysical observations in order to construct the optimal configuration with the least amount of membrane deformation rate required for a subduction system. We examine the correlation between the pattern of deformation of this optimal configuration and those indicated by various geophysical observations in order to understand how important a role the membrane deformation plays in the subduction process.

(3). Interpolating the large scale structure of the subducted slab based on the criteria of minimizing the membrane deformation rates.

(4). Obtain a better understanding of why slabs have their observed shapes, and why focal mechanisms have their observed orientations.

In pursuit of a better understanding of the subduction process, this study will provide a systematic way of examining the fundamental problem of the geometric effects of the subduction process and their correlation with the intermediate and deep seismic activity.

The first main difficulty in formulating a feasible numerical modeling scheme in this study is that, since it is in general not possible to construct a two-dimensional global Cartesian coordinate system on an arbitrary curved surface [Aris, 1962; Pearson, 1990], the velocity gradient tensor and strain rate tensor usually have to be defined in a general curvilinear coordinate system using general tensor calculus. To avoid the complexity resulted from this, we will formulate the problem in a fixed Cartesian coordinate frame, and define the strain-rate tensor in terms of a properly defined projection operation based on the fact that our non-Euclidean 2-space (the slab surface) is embedded in the Euclidean 3-space. Chapter 2 describes the way we formulate the problem, especially how we apply the projection operator to get the membrane strain rate tensor for an arbitrary surface and then evaluate the integrated total dissipation power for a general flow with power-law rheology. We will then be equipped with a well defined optimization problem, in the sense that we invert for both the complete flow field and the surface geometry swept out by this flow field which minimize the integrated total dissipation power. The second difficulty is that, although the variation of flow field with respect to a fixed slab geometry is linear, the variation of geometry is highly non-linear. Three different kinds of Finite element configurations used to parameterize both the surface geometry and the flow field are discussed. The numerical iteration algorithm used to solve the non-linear inversion is outlined.

In chapter 3, observations related to geometric constraints in Cascadia Subduction Zone are discussed. Successive modeling efforts designed for examining the pattern of membrane deformation rates and the slab geometry and their relations with the trench configuration were undertaken. The main features of the modeling experiments in terms of their capability to offer plausible explanation toward major observations are described.

Chapter 4 presents preliminary modeling results on two well documented subduction zones: Aleutian-Alaska and NW-Pacific. Experiments generally adopt highly simplified trench shapes in order to understand the dominant first order observations, e.g. the arch structures in the subducted slabs associated with slab subducting in a oceanward concave geometry, and the general orientations of earthquake focal mechanisms.

In Chapter 5, conclusions on experiments for different subduction zones are discussed. The application of this modeling technique for studying subduction processes in general is appraised. Improvements and future work are discussed.

Chapter 2 Theoretical Formulation

Chapter 1 described the observations concerning the three-dimensional nature of the subduction process and the reason we believe that the lateral membrane deformation is of fundamental importance in understanding these observations. A full three-dimensional treatment of the subduction process covering all aspects including the dynamics and the thermal and rheological structure is not computationally feasible and also impractical because of unknown parameters and possible chaotic flow. Instead of taking such a brute force approach and with the basic physics buried deeply in a complicated model, we simplify the problem based on certain assumptions so that we can concentrate on examining the lateral membrane deformation of subducting slabs required by geometric and kinematic boundary conditions. This chapter shows our basic philosophy and efforts in formulating the problem of quantifying the membrane deformation during subduction process. By developing a scalar measure of the membrane deformation rates, we devise an inverse scheme to explore how subducting slabs respond to different geometric and kinematic constraints.

As already discussed in chapter 1, the mechanical thickness of subducting slabs is very small comparing to their lateral dimensions. In other words, subducting slabs are geometrically analogous to thin sheet like structures. The exact rheology of subducting slabs is still largely unknown. Although the mechanical response of the oceanic lithosphere to loads may be represented by the flexure of an elastic plate (Forsyth, 1989), it had been argued that an elastic-perfect plastic rheology might be more appropriate for studying bending of oceanic lithosphere near the trench [e.g. Turcotte et al., 1978]. It is not realistic to assume elastic behavior, however, when dealing with the subducting slab as a whole. First of all, the strain-rates associated with the subduction process are usually on the order of $10^{-15} \text{ sec}^{-1}$ [Bevis, 1988; Burbach and Frohlich, 1986; Creager and Boyd, 1991] which amounts to several tens of percent of accumulated strain within a typical 10 my of subduction. The shear modulus of the upper most mantle is 1300 kbar [Dziewonski and Anderson, 1983], so shear strains of 10% would produce shear stresses of 260 kbar, which is well above the material strength of subducting slabs. Secondly, the slab earthquakes cause irreversible change of slab geometry, these macroscopic processes together with microscopic creeping mechanisms during the

geological time period, make the rheological behavior of subducting slabs resembles viscous flow in a bulk average, long term average sense. General Power-Law rheology will be used in the modelling experiment in this study as standard rheological models. Since the Power-Law rheology with the power $n \rightarrow \infty$ approximates plastic behavior, the cases $n=1$ (Newtonian) and $n=\infty$ thus represent two end members of possible flow laws. In short, the first assumption we make is that subducting slabs can be treated like thin viscous sheets with either Newtonian or general Power-Law rheology.

Because slabs are cold relative to the surrounding mantle, the effective viscosity of the slab is probably at least a few orders of magnitude higher than the surrounding warm mantle [e.g. Vassiliou and Hager, 1988]. In Appendix A we show that this assumption leads to the conclusion that the shear strain rates parallel to the slab, evaluated at the cold core of the slab is a few orders of magnitude less than in the ambient mantle. In other words, the shear deformation parallel to the slab surface would essentially be taken up by the surrounding mantle. This is analogous to the Kirchhoff's hypothesis in studying the deformation of elastic shells [e.g. Calladine, 1988]. In essence, this implies that we can characterize the deformation of a thin sheet structure by the membrane deformation within the mid-surface and the bending deformation.

Now that we are simulating the subduction process by a viscous thin sheet structure subducting in a much less viscous environment, a proper mass conservation law is needed to complete the kinematic description of the system. We do this by assuming that the mantle is incompressible. This is, of course, neglecting important effects of the major transition zones (basalt-eclogite, olivine-spinel). Since the details of how materials deform when going through a phase transition are still largely unknown, it is premature to include these effects. However, the compressibility condition in our model is implemented computationally in a very flexible way such that other kinds of compressibility can be incorporated very easily.

The last important assumption we make is that the flow field representing subduction process is in steady state. This is in general not true, since transient evolution of subduction system configurations have been reported in terms of the migration of both the trench and converging plates. However, it has been argued that during the last 15 my

or so, the subduction processes are relatively stable for the two major subduction zones we are going to examine: Aleutian Subduction Zone [Creager and Boyd, 1991]; and Kuril-Japan Subduction Zones [Lundgren and Giardini, 1990]. It is, however, not the case for the other subduction system of interest, i.e. Cascadia Subduction Zone [Nishimura et. al., 1984; Riddihough, 1984; Vandecar, 1991]. Our calculation are thus performed based on the current configuration of the subduction system. This allows us to examine how the subducting slab responds to the current configuration and the possible deformation regime within the slab. However, we admit that the deformation in this subduction zone is likely to be complicated by the change of relative plate convergence during the past 10 my.

In summary, the main assumptions in our formulation are:

- (1). *Slab can be treated as a thin viscous sheet.*
- (2). *Slab effective viscosity is orders of magnitude higher than the surrounding mantle.*
- (3). *The mantle is incompressible.*
- (4). *The flow field representing subduction is in steady state.*

Based on the preceding assumptions, we can then get the full three-dimensional strain-rate tensor by taking the symmetric part of the velocity gradient tensor evaluated at the mid-surface of the slab. Section 2.1 will show that a simple expansion with respect to the mid-surface decomposes the full strain-rate tensor into two parts describing the membrane- and the bending-deformation rate. These two parts interact nonlinearly [Calladine, 1988; Olszak and Sawczuk, 1967]. In the limiting case when the thickness approaches zero, the bending part of the deformation rate can be ignored. Since subducting slabs have finite thickness, the bending deformation rate is important. On the other hand, we do examine bending strain rates in 2-D cross section (section 2.2), so we can compare these strain rates with membrane strain rates and see where one is likely to dominate over the other. We build boundary conditions for the subducting slab geometry by considering hypocenters of Wadati-Benioff earthquakes and bending deformation rate in simplified two-dimensional cross sections (Section 2.2). In the calculation of membrane deformation rate, the bending deformation rate is not explicitly incorporated however.

Evaluating the full velocity gradient tensor requires information of the flow field not only on the mid-surface, but also the flow outside the surface. Although Assumption 2 enables us to concentrate on the deformation of the slab surface itself, because of the irregular shape of the surface, there is no easy way to reduce the calculation within the surface except by using curvilinear coordinate system on the non-Euclidean 2-space representing the slab surface. The surface projection operator that will be described in Section 2.3, however, serves as a convenient tool to extract the deformation rates confined in the surface (i.e. the membrane deformation rates). The elegance of the projection operator is that it can be easily defined in a simple three-dimensional Cartesian coordinate system. It also helps to map the three-dimensional problem into a two-dimensional space. This not only greatly simplifies the computation but also concentrates the efforts of calculation within the surface while avoiding the complexity of performing general non-Cartesian tensor calculus.

Having properly quantified the membrane strain-rate tensor, we can thus evaluate the integrated total dissipation power. For Newtonian flow, this scalar quantity is mathematically proportional to the L^2 norm of the membrane strain-rate tensor integrated over the slab surface. For the Power-Law flow with the power $n=\infty$, on the other hand, it corresponds to the L^1 norm. This quantity then serves naturally to be a measure of the total membrane deformation rate. In section 2.4, we use this measure to compare membrane deformation rates for different subduction configurations. This enables us to devise an inversion scheme which seeks the slab geometry and corresponding flow field with the least amount of membrane deformation rate while satisfying the prescribed boundary conditions. The general dissipation power functional that is minimized depends linearly on the flow field but non-linearly on the slab geometry. The full optimization to seek the optimal slab geometry and the corresponding flow field is thus a non-linear inversion.

2.1 Decomposition of membrane- and bending-deformation rate

Now consider a local slab coordinate (t,s,n) shown in Figure 2.1. According to the assumptions above, we can then approximate the strain rate tensor \mathbf{D} by expanding it in the slab normal direction:

$$\mathbf{D}(t,s,n) = \mathbf{D}^{pp}(t,s,0) + n \frac{\partial \mathbf{D}^{pp}(t,s,0)}{\partial n} + \mathbf{o}(n^2) \quad (2.1.1)$$

where $n=0$ corresponds to the cold thermal core of the slab, referred to here as the "slab surface". \mathbf{D}^{pp} is the membrane strain rate tensor that is the primary deformation rate targeted in this study, while $\frac{\partial \mathbf{D}^{pp}}{\partial n}$ can be shown to be related to the bending part of the deformation rate. More discussion on the decomposition of the strain rate tensor into the membrane strain rate tensor and the bending strain rate tensor can be found in Creager and Boyd [1991].

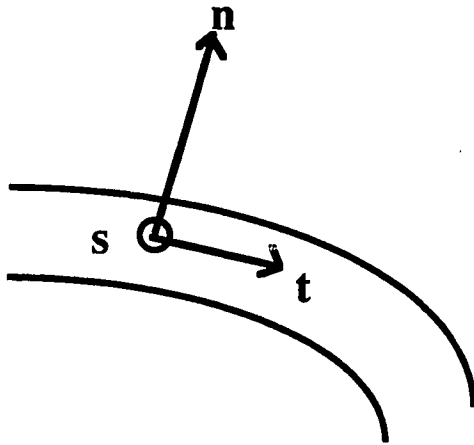


Figure 2.1 Local slab-normal coordinate, t : down-dip tangent, n : slab normal, s : along strike tangent.

Equation (2.1.1) shows that the bending deformation is in fact a second order phenomena as compared with the membrane deformation. As discussed in chapter 1, the two-dimensional simplification for modelling slab bending assumes implicitly that the membrane strain rate tensor \mathbf{D}^{pp} of the *mid-surface* is zero and concentrates on the bending strain rate $\frac{\partial \mathbf{D}^{pp}}{\partial n}$. This is generally not true, considering the three-dimensional

nature of subduction processes. Again, it is the basic goal of this dissertation to not only point out the fundamental importance of this usually ignored mechanism but also devise a scheme to quantify the membrane deformation rates associated with the subduction process.

2.2 Bending deformation in simplified two-dimensional case

Even in this simplified situation, to determine a self-consistent slab shape and quantifying slab deformation regime is not an easy task, mainly because of the various dynamic controlling factors involved, e.g. the gravitational pulling; the thermal straining; the viscous drag induced by the coupling of the down going slab with the mantle and the effects of mantle wind, and the macroscopic rheological character of the slab material. Instead of pursuing the complete dynamics of the process, since we usually have some information on the slab shape (given that the Wadati-Benioff zone delineate the low wavenumber structure of the slab), a kinematic or geometric approach is sometimes used to serve the purpose toward interpolating the slab shape and estimating the deformation regime associated with that particular geometry. In many situations near the surface of Earth, the mechanical response of the lithosphere to applied loads can be represented by the flexure of an elastic plate. In the simplified two-dimensional case, assuming an initially flat plate with a flexural rigidity D , the integrated strain energy is thus:

$$U = \frac{1}{2} \int D \kappa^2 ds \quad \text{_____} \quad (2.2.1)$$

where κ is the curvature, ds is the incremental length element along the shape of the slab in the down-dip direction

For constant D , U is then proportional to

$$I = \int \kappa^2 ds \quad \text{_____} \quad (2.2.2a)$$

It had been shown that "minimum strain energy" is the appropriate variational principle governing the elastic plate bending (e.g. Timoshenko and Goodier, 1970; Lee and Forsyth, 1973). In other words, Minimizing I defined in Equation 2.2.2a is then the variational principle for interpolating the shape of a bending elastic plate in the simplified two-dimensional case. Notice that when calculating the local curvature κ for the plate with displacement $w(x)$ at a point x , a common practice that is usually not well justified is

to approximate κ by $\frac{d^2w}{dx^2}$, instead of the precise form $\frac{d^2w/dx^2}{\sqrt{1+(dw/dx)^2}}$ i.e.,

$$\int \kappa^2 ds \approx \int \left(\frac{d^2w}{dx^2}\right)^2 dx \quad \text{_____} \quad (2.2.2b)$$

Briggs (1974) showed that minimizing Equation (2.2.2b) leads to the differential equation:

$$\frac{d^4w}{dx^4} = \sum_i f_i \delta(x-x_i) \quad \text{_____} \quad (2.2.3)$$

Minimizing functional (2.2.2) is thus equivalent to solving a particular bending problem with point loadings f_i at $x=x_i$ such that at those points $w=w_i$. This "minimum curvature" algorithm is in fact the well known *Interpolating natural spline* and is widely used in the geophysical community both in its one-dimensional and two-dimensional form (e.g. Briggs, 1974; Smith and Wessel, 1990). In the case of interpolating cross sectional shape of the subducting slab, we have the subducted slab depths constrained by the Wadati-Benioff seismicity at certain points along the cross section. A "minimum curvature algorithm" interpolation scheme based on solving Equation (2.2.3) or minimizing (2.2.2) is, in its essence, minimizing the elastic bending energy subject to the boundary conditions that w have to satisfy the known information. Although other more realistic rheologies have been used to study oceanic lithospheric bending at the trench, e.g. viscoelastic [DeBremaecker, 1977; Melosh, 1978]; elastic-perfectly plastic [Turcotte

et al., 1978; McAdoo et al., 1978]. The minimum curvature algorithm represents one extreme member among the methods used to interpolate the slab shape.

An alternative algorithm is to notice that for a thin plate with finite thickness H , if the subduction can be represented by the convergence rate v , then the bending strain rate

$$\frac{V(d\kappa/ds)H}{4} = \frac{1}{H} \int_{\frac{H}{2}}^{\frac{H}{2}} V(d\kappa/ds)ndn$$

average through thickness is proportional to $d\kappa/ds$, $d\kappa/ds$ is the change of curvature along the path. If both H and v are constants, then to find the minimum bending deformation rate configuration is equivalent to minimizing

$$\int (d\kappa/ds)^2 ds \quad \text{-----} \quad (2.2.4)$$

Notice that this quantity is proportional to the dissipation power owing to bending deformation rates in a viscous flow. This minimum "change of curvature" algorithm is physically more realistic than the minimum curvature scheme described above, since the minimum curvature scheme is only appropriate for pure elastic bending with small displacement field away from the initial flat configuration. More importantly, the minimum curvature algorithm tends to squeeze the curvature into finite narrow regions while the minimum change of curvature algorithm accumulates curvature in a smooth, gradual fashion (Figure 2.2). The concentration of curvature produced by considering bending deformation elastically (minimum curvature scheme) yields typical curvature on the order of 10^{-2} km^{-1} . With a typical mechanical thickness of a few tens of kilometers, this amounts to a typical elastic strain ($\kappa \times H$) on the order of 10^{-1} . Multiplying this by the shear modulus of the mantle gives shear stresses of a thousand kilobars that is again well above the material strength of slabs.

We devised a non-linear iteration scheme to numerically achieve the "change of curvature" optimization subject to the boundary conditions that the slab goes through the trench and be flatten at certain depth, i.e. three boundary conditions: the depth, the slope and the curvature at both ends of our calculation region are specified. In other words, this scheme seeks the solution with the least amount of bending deformation rate, while satisfying the boundary conditions at both ends, the slab thus achieves both bending and

unbending within the region of interest. Our scheme provides a way of obtaining the optimal self-consistent slab shape that can be used in estimating the unbending strain-rate as discussed by Tsukahara [1980] and Kawakatsu [1986]. Figure 2.2 compares the slab shape, the curvature and the change of curvature as functions of the horizontal distance from the trench obtained by both the "minimum curvature" and the "minimum change of curvature" schemes. It is clear that while minimizing curvature results in concentration of curvature and will thus induce extremely large change of curvature, the minimum change of curvature scheme presents a nearly linear change of curvature.

For this study, we are using the algorithm described above to construct cross-sectional shapes, and build the slab surface based on cross sections thus obtained. Once the slab surface is constructed, we will be examining the membrane deformation rate associated with this configuration assuming the slab is infinitely thin. In other words, although the shape of the two-dimensional cross sections are built under consideration of optimal bending deformation regime, the bending deformation rate is not actually considered simultaneously with the membrane deformation rate in examining the optimal deformation regime of the three-dimensional slab surface. This is by no means implying that the bending deformation rate is not an important mechanism, rather, this is the first cut of an attempt to quantify a more fundamental kind of deformation in the three dimensional space.

Note that the in Figure 2.2, the shapes are similar (probably cannot distinguish among shapes by seismicity distributions), but the curvature and the change in curvature are very different. The deformation rate at the edges of a slab average through thickness H with subduction velocity V is $\frac{V(d\kappa/ds)H}{4}$. For each subduction zone examined we can produce diagrams like that shown in Figure 2.2 to estimate the bending strain rate owing to bending. For Cascadia, we obtain a peak bending deformation rate of $2 \times 10^{-16} \text{ sec}^{-1}$, assuming $H=10 \text{ km}$, $V=1.6 \times 10^{-12} \text{ km/sec}$, $(d\kappa/ds)^{\text{max}} = 5 \times 10^{-5} \text{ km}^{-2}$.

2.3 Membrane deformation rates: Forward Problem

2.3.1 Conceptual view of the membrane strain rate tensor

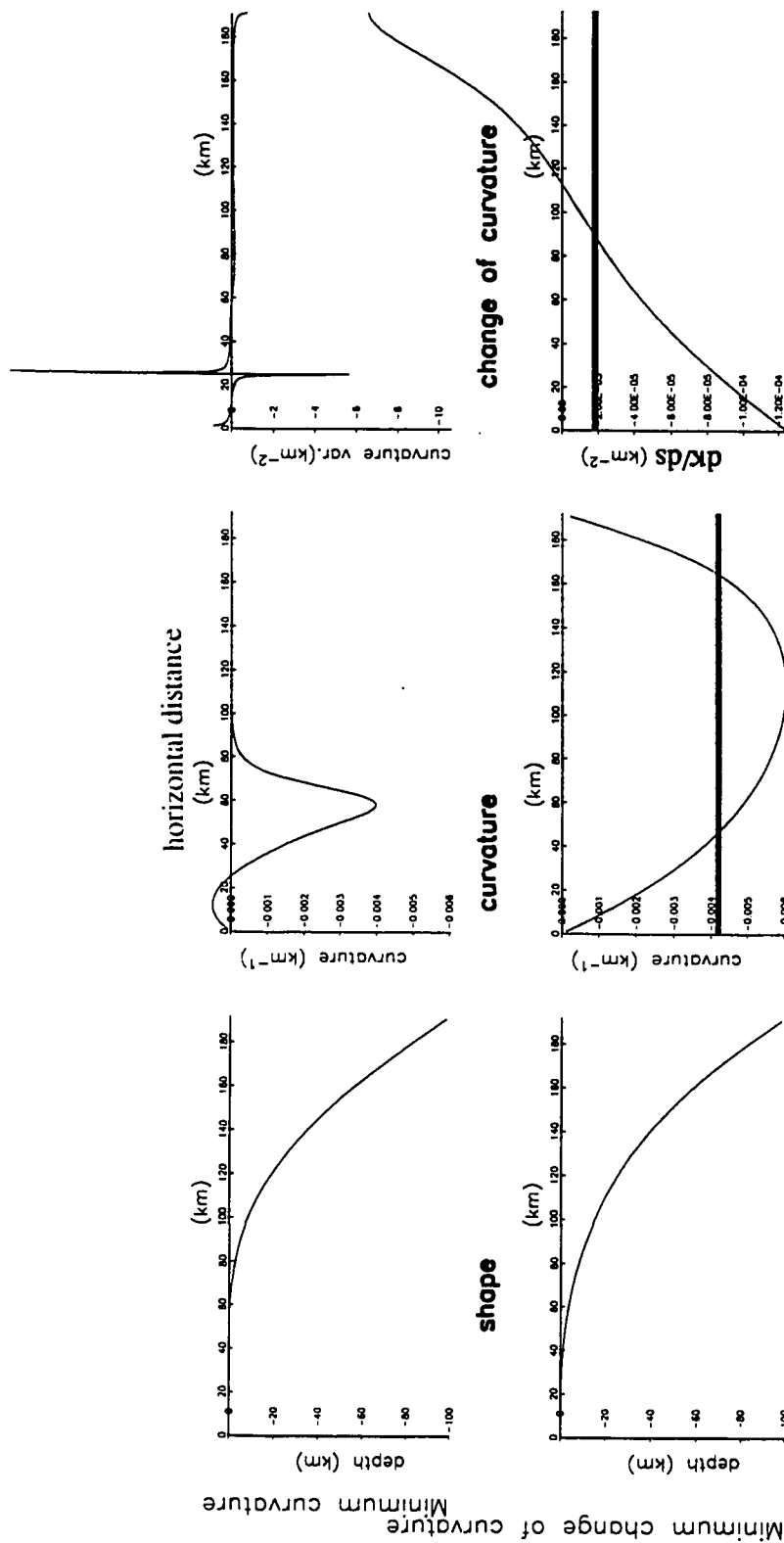


Figure 2.2 Interpolated slab geometry in idealized two-dimensional cross section. Boundary conditions are that the slab's depth, slope and curvature are zero at the trench ($x=0$); 200km landward from the trench, the slab's depth, dip and curvature are 100km, 55° and 0 km^{-1} . The left drawings show the slab shape obtained by minimizing the curvature (upper panel) and the change of curvature (lower panel). The plots in the center show the curvature, while right plot shows the derivative of curvature (κ) with respect to distance along the slab (s). Solid bars show results of Kawakatsu's calculation [Kawakatsu, 1986]. Note that Kawakatsu underestimates change in curvature because his difference scheme does not satisfy boundary conditions that the curvatures at both ends go to zero smoothly.

For a given flow field in the three dimensional space that sweeps out a well defined surface, the first step needed to quantitatively measure its membrane deformation is the evaluation of the membrane strain rate tensor. It represents physically the extension, compression and shearing confined within the surface swept out by the flow field. In the simple case when the surface is flat or is a simple spherical shell, it is straightforward to carry out this calculation. However, for an arbitrary surface embedded in the three-dimensional space, since the surface is generally not *flat* or *developable* (e.g. a cylindrical surface), the Gaussian curvature does not vanish everywhere on the surface, it is then generally impossible to construct a two-dimensional Cartesian system within that surface. This then imposes certain difficulties for mathematically defining and computing the membrane strain rate tensor.

A simple approximation to visualize the membrane strain rate tensor is the following. Suppose we have the complete Lagrangian description of the flow field, i.e. assuming that we can always track any particle path within the region of interest. Then anywhere on the surface swept out by the flow, we can choose three neighboring, non-colinear points that define a plane. In the limit when these points approach one another, this plane approximates the local tangent of the surface. As shown in Figure 2.3, points A, B, C move along the surface to points A', B', C'. In analyzing membrane strain, we are not concerned with rotation of the triangle either about an axis normal to the slab surface, or owing to change in orientation of the surface itself. Membrane deformation is a measure of the change in shape or size of the triangle, a concept that is coordinate system independent.

Define the normalized changes in length :

$$S^\alpha = \frac{\alpha - \alpha'}{\alpha}, \quad \alpha \in \{a, b, c\} \quad (2.3.1.1)$$

for $\alpha = a, b$ and c , let \mathbf{d}^α be the unit vector pointing in the direction of line segment α .

Choose an orthogonal two-dimensional coordinate system in the ABC plane and let d_i^α and e_{ij} be the components of the unit vector \mathbf{d}^α and the strain rate tensor \mathbf{e} .

$$d_i^\alpha e_{ij} d_j^\alpha = S^\alpha, \quad \text{sum over } i, j \text{ but not } \alpha. \quad (i, j \in \{1, 2\}, \alpha \in \{a, b, c\}) \quad (2.3.1.2)$$

which represents three equations that can then be solved for the three independent components of the symmetric two-dimensional strain rate tensor \mathbf{e} . This approximation is physically simple to visualize, it points out that whatever the orientation might be, the membrane strain tensor is simply the extension, compression and shearing that occurs within the surface.

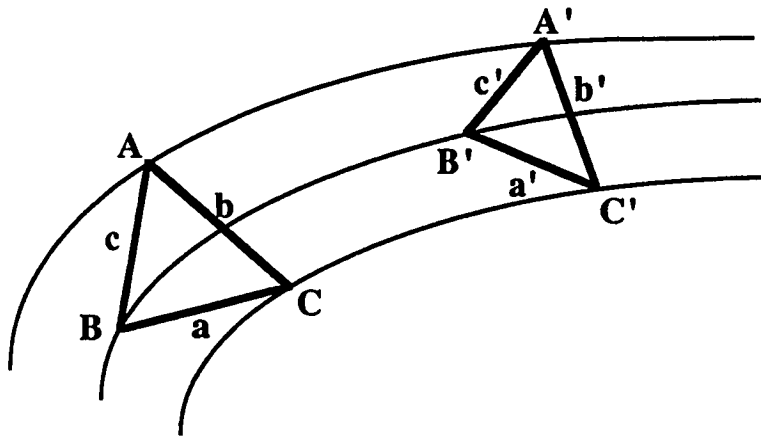


Figure 2.3 A, B, C are three non-colinear points embedded in a surface flow which form a triangle with sides of length a,b and c. After a short period of time, these points are mapped to points A', B' and C' by the flow field.

The scheme to estimate Lagrangian strain tensor formulated above can be written in a more general fashion, in that we can construct a general two-dimensional curvilinear coordinate system say (x_1, x_2) on the surface swept out by the flow field, then the length element at any point is

$$dS = C_{ij} dx_i dx_j, \quad (i, j \in \{1, 2\}) \quad (2.3.1.3)$$

C_{ij} is the local metric tensor at that point.

Now for a small patch of the material, we construct a general curvilinear coordinate system having the metric tensor C^0_{ij} as that mentioned above and we fix this coordinate frame to the material particles. After a short period of time, this patch of material would be mapped into a different configuration by the flow field just like the triangles shown in Figure 2.3. The coordinate frame that was constructed before the mapping would now be distorted and have a different metric tensor C_{ij} . The Lagrangian strain tensor can

now be very conveniently written [e.g. Pearson, 1990; Grundland and Niewiadomski, 1986] in the form as

$$e_{ij} = \frac{1}{2}(C_{ij} - C_{ij}^0) \quad (2.3.1.4)$$

Note that if the surface is flat or developable then we can always choose the Cartesian coordinate as the initial coordinate system, the metric tensor C_{ij}^0 is equal to the identity tensor and e_{ij} then reduces to the usual definition of strain tensor in Cartesian coordinate system, i.e.

$$e_{ij} = \frac{1}{2}\left(\frac{\partial u_j}{\partial x_i} + \frac{\partial u_i}{\partial x_j}\right) \quad (2.3.1.5)$$

This is of course not applicable in evaluating membrane strain (rate) tensor in general, since the surfaces we are dealing with are generally not flat. In fact, covariant derivatives have to come in and replace the normal partial derivatives.

2.3.2 Gaussian curvature

The foregoing discussion on Lagrangian description highlights some important constraints on the deformation regime posed by the geometry of an arbitrary surface (a non-Euclidean 2-space where the metric tensor is not necessarily fixed everywhere). A useful indication or measure of that constraint is an intrinsic property of the surface called the "Gaussian curvature". The simplest definition of the Gaussian curvature is the product of the two principal curvatures measured in two mutually orthogonal directions at a local point. The "Gauss' theorem", in the theory of Differential Geometry, states that the Gaussian curvature of a surface is bending invariant. In other words, conservation of Gaussian curvature before and after a mapping is the necessary condition for the surface to be free from any local internal deformation. This is not surprising, if we notice that Gaussian curvature is directly related to the metric tensor and its first derivatives. Although it is generally impossible to construct a Cartesian coordinate system on an arbitrary surface, an orthogonal curvilinear coordinate system called geodesic coordinate

system can always be built for such a surface. For this orthogonal system (ξ, η) , the metric tensor reduces to a diagonal form:

$$C_{11}=\alpha, C_{12}=C_{21}=0, C_{22}=\beta \quad \text{_____} \quad (2.3.2.1)$$

and the line element will be

$$ds^2 = \alpha^2 d\xi^2 + \beta^2 d\eta^2 \quad \text{_____} \quad (2.3.2.2)$$

on that surface. It can then be shown [Pearson, 1990] that

$$\frac{\partial}{\partial \xi} \left(\frac{1}{\alpha} \frac{\partial \beta}{\partial \xi} \right) + \frac{\partial}{\partial \eta} \left(\frac{1}{\beta} \frac{\partial \alpha}{\partial \eta} \right) + \alpha \beta \kappa_G = 0 \quad \text{_____} \quad (2.3.2.3)$$

Where κ_G is the Gaussian curvature. This shows clearly that the Gaussian curvature depends only on the metric tensor and variations of the metric tensor. Notice that although the metric tensor is different for each different coordinate system, the Gaussian curvature is a coordinate system independent physical quantity and is an intrinsic property of the surface. The connection between Gaussian curvature and surface deformation is now clear that from Equation (2.3.1.4), surface deformation is in fact a measure of variation of metric tensor defined by the mapping (the displacement or the velocity field) which is then directly related to the Gaussian curvature.

Another way to examine this effect, in the context of the theory of Continuum Mechanics, is to examine the compatibility conditions for a curved surface. Simply put, the deformation or strain field for a mapping confined within a curved surface can not be assigned arbitrarily without subject to the local geometric constraint to assure the compatibility of the mapping (the displacement or the velocity field). In other words, the strain (strain rate) field has to satisfy the compatibility conditions to guarantee that the displacement (velocity) field that they are derived from are physically realistic. Geometrically, the easiest way to visualize this is imagining cutting the pre-strained surface into small squares, and then try to fit them back to form a continuous surface after each square is given a certain strain; in general the strained pieces cannot be fit back

together without further deformation, but if the strain in each part is related to the strain in its neighbors according to the compatibility conditions, which is governed by the local change of curvature, then they can be fit back together. A simple example to elucidate this is to consider the elastic deformation occurring in a thin shell, for a relatively small region that started flat and was subsequently deformed slightly. These compatibility equations can be reduced [Calladine, 1988] to

$$-\frac{\partial^2 e_{xx}}{\partial y^2} + \frac{\partial^2 e_{xy}}{\partial x \partial y} - \frac{\partial^2 e_{yy}}{\partial x^2} = \delta(\kappa_G) \quad \text{_____} (2.3.2.4)$$

where (x,y) is a local tangential two-dimensional Cartesian coordinate system; e_{xx} , e_{xy} , e_{yy} are corresponding components of the membrane strain tensor, and $\delta(\kappa_G)$ is the change of Gaussian curvature before and after the deformation. Obviously if the plane stays flat before and after the deformation is imposed, this equation further reduces to our familiar compatibility equation for plane-strain problem where $\delta(\kappa_G)$ is always zero. It is clear from this equation why Gauss theorem demands the conservation of Gaussian curvature as a necessary (not sufficient) condition to be free from in-plane deformation. Gaussian curvature is a powerful tool to examine whether there would be intrinsic deformation associated with a certain mapping. For example, Bevis [1986] applies Gauss theorem in examining several subduction zones and argues that since the Gaussian curvature is generally not conserved for the slab before and after subduction, it is unavoidable for the slab to suffer certain amount of membrane deformation. He also points out that the popular Frank's (1968) "ping-pong ball" model can be viewed as a particular example of conserving Gaussian curvature and thus avoiding internal deformation. An important point worth mentioning here is that, it is the conservation of Gaussian curvature rather than the "conservation of slab area" [e.g. Minamino and Fujii, 1981] that is controlling the possible contortion of the subducted slab. Unfortunately, we have not been able to devise a scheme to use Gauss theorem to quantify the relation between an arbitrary surface with spatially varying Gaussian curvature and the resulting deformation field associated with flow along the surface. The Gaussian curvature concept in itself is not enough to provide a feasible mean for the purpose of actually quantifying the deformation field associated with a non-ideal mapping (i.e. the Gaussian curvature is not conserved). This study is an attempt to devise such a machinery so that

we can examine the least amount of deformation rate associated with subduction where obvious change of geometric configuration occurs.

2.3.3 The projection operator

For any well-defined flow field \mathbf{V} embedded in the three-dimensional Euclidean space, the velocity gradient tensor is simply

$$\mathbf{L} = \nabla \mathbf{V}^T \quad (2.3.3.1)$$

Now suppose at the same time we have a well-defined surface Z also embedded in the same 3-D space and that in a global Cartesian coordinate system with base vectors $\hat{\mathbf{e}}_x, \hat{\mathbf{e}}_y, \hat{\mathbf{e}}_z$ the surface can be written as $Z=z(x,y)$. For any point located on the surface Z , we can always define a local Cartesian coordinate system using base vectors $\hat{\mathbf{e}}_s, \hat{\mathbf{e}}_t, \hat{\mathbf{e}}_n$ with $\hat{\mathbf{e}}_s, \hat{\mathbf{e}}_t$ representing two unit vectors orthogonal to each other and both tangent to the surface; $\hat{\mathbf{e}}_n = \hat{\mathbf{e}}_s \times \hat{\mathbf{e}}_t$ is then the unit normal vector. We can now decompose \mathbf{L} evaluated on the surface as

$$\mathbf{L} = \sum_{i,j=s,t,n} \partial_i v_j \hat{\mathbf{e}}_i \hat{\mathbf{e}}_j, \quad \hat{\mathbf{e}}_i \hat{\mathbf{e}}_j \text{ is the dyad } \hat{\mathbf{e}}_i \otimes \hat{\mathbf{e}}_j \quad (2.3.3.2)$$

From the classical Helmholtz' theorem, we can get the strain-rate tensor \mathbf{D} by

$$\mathbf{D} = \frac{1}{2}(\mathbf{L} + \mathbf{L}^T) \quad (2.3.3.3)$$

the six independent components of \mathbf{D} are then clearly:

the stretching or compression

$$\begin{array}{l} \partial_s v_s \quad \quad \quad s \\ \partial_t v_t \quad \text{in the } t \quad \text{direction;} \\ \partial_n v_n \quad \quad \quad n \end{array}$$

and the shearing

$$\begin{array}{l} (\partial_t v_s + \partial_s v_t)/2 \quad \quad \quad \text{within the surface;} \\ (\partial_s v_n + \partial_n v_s)/2, (\partial_t v_n + \partial_n v_t)/2 \quad \text{parallel to the surface.} \end{array}$$

As argued in appendix A, assuming that the viscosity is much lower outside the slab than within, most of the shearing parallel to the surface occurs in the region outside the slab. Thus, the last two terms of \mathbf{D} above (shearing parallel to the surface) are expected to be small when evaluated within the cold core of the slab (Note that the equivalent terms evaluated in the mantle adjacent to the slab represent the viscous drag that supports the slab and is a region of very large deformation rates). A mathematically convenient way to insure that the shear parallel to the surface vanishes is to consider any velocity field \mathbf{V} that does not cross the surface Z , construct the deformation rate tensor \mathbf{D} from \mathbf{V} (Equations (2.3.3.1) and (2.3.3.3)) and apply the surface projection operator to \mathbf{D} .

Define the surface projection operator to be

$$\mathbf{P} = \mathbf{I} - \widehat{\mathbf{e}}_n \widehat{\mathbf{e}}_n, \text{ where } \mathbf{I} \text{ is the 3-D identity operator; Obviously, } \mathbf{P} = \mathbf{P}^T \quad (2.3.3.4)$$

notice that \mathbf{P} is the same as Backus' "surface identity operator" \mathbf{I}_s [Backus, 1967].

Since

$$\widehat{\mathbf{e}}_t \cdot \widehat{\mathbf{e}}_n = \widehat{\mathbf{e}}_n \cdot \widehat{\mathbf{e}}_t = \widehat{\mathbf{e}}_s \cdot \widehat{\mathbf{e}}_n = \widehat{\mathbf{e}}_n \cdot \widehat{\mathbf{e}}_s = 0 \quad (2.3.3.5)$$

so that

$$\mathbf{P} \cdot \widehat{\mathbf{e}}_s \widehat{\mathbf{e}}_s \cdot \mathbf{P}^T = [(\mathbf{I} - \widehat{\mathbf{e}}_n \widehat{\mathbf{e}}_n) \cdot \widehat{\mathbf{e}}_s \widehat{\mathbf{e}}_s] \cdot \mathbf{P}^T = \widehat{\mathbf{e}}_s \widehat{\mathbf{e}}_s \cdot \mathbf{P}^T = \widehat{\mathbf{e}}_s \widehat{\mathbf{e}}_s \quad (2.3.3.6)$$

and similarly,

$$\mathbf{P} \cdot \widehat{\mathbf{e}}_t \widehat{\mathbf{e}}_t \cdot \mathbf{P}^T = \widehat{\mathbf{e}}_t \widehat{\mathbf{e}}_t, \quad \mathbf{P} \cdot \widehat{\mathbf{e}}_s \widehat{\mathbf{e}}_t \cdot \mathbf{P}^T = \widehat{\mathbf{e}}_s \widehat{\mathbf{e}}_t, \quad \mathbf{P} \cdot \widehat{\mathbf{e}}_t \widehat{\mathbf{e}}_s \cdot \mathbf{P}^T = \widehat{\mathbf{e}}_t \widehat{\mathbf{e}}_s,$$

$$\mathbf{P} \cdot \widehat{\mathbf{e}}_t \widehat{\mathbf{e}}_n \cdot \mathbf{P}^T = \mathbf{P} \cdot \widehat{\mathbf{e}}_n \widehat{\mathbf{e}}_t \cdot \mathbf{P}^T = \mathbf{P} \cdot \widehat{\mathbf{e}}_s \widehat{\mathbf{e}}_n \cdot \mathbf{P}^T = \mathbf{P} \cdot \widehat{\mathbf{e}}_n \widehat{\mathbf{e}}_s \cdot \mathbf{P}^T = \mathbf{P} \cdot \widehat{\mathbf{e}}_n \widehat{\mathbf{e}}_n \cdot \mathbf{P}^T = 0. \quad (2.3.3.7)$$

Thus if we then apply the surface operator on both sides of \mathbf{D} , we get

$$\begin{aligned} \mathbf{D}^{pp} &= \mathbf{P} \cdot \mathbf{D} \cdot \mathbf{P}^T = \mathbf{P} \cdot \frac{(\mathbf{L} + \mathbf{L}^T)}{2} \cdot \mathbf{P}^T \\ &= \widehat{\mathbf{e}}_t \widehat{\mathbf{e}}_t (\partial_t v_t) + \widehat{\mathbf{e}}_s \widehat{\mathbf{e}}_s (\partial_s v_s) + [\widehat{\mathbf{e}}_s \widehat{\mathbf{e}}_t (\partial_s v_t) + \widehat{\mathbf{e}}_t \widehat{\mathbf{e}}_s (\partial_t v_s)]/2 \quad (2.3.3.8) \end{aligned}$$

i.e. \mathbf{D}^{pp} is the surface deformation part of the complete strain-rate tensor \mathbf{D} , furthermore, applying assumption 3), to enforce incompressibility

$$\nabla \cdot \mathbf{V} = \partial_t v_t + \partial_s v_s + \partial_n v_n = 0 \Rightarrow \partial_n v_n = -(\partial_t v_t + \partial_s v_s) \quad (2.3.3.9)$$

we thus have

$$\begin{aligned} \widetilde{\mathbf{D}^{pp}} &= \mathbf{P} \cdot \mathbf{D} \cdot \mathbf{P}^T + \widehat{\mathbf{e}}_n \widehat{\mathbf{e}}_n (-\partial_t v_t - \partial_s v_s) \\ &= \widehat{\mathbf{e}}_t \widehat{\mathbf{e}}_t (\partial_t v_t) + \widehat{\mathbf{e}}_s \widehat{\mathbf{e}}_s (\partial_s v_s) + [\widehat{\mathbf{e}}_s \widehat{\mathbf{e}}_t (\partial_s v_t) + \widehat{\mathbf{e}}_t \widehat{\mathbf{e}}_s (\partial_t v_s)] / 2 + \widehat{\mathbf{e}}_n \widehat{\mathbf{e}}_n (-\partial_t v_t - \partial_s v_s) \end{aligned} \quad (2.3.3.10)$$

as the strain-rate tensor that we are interested in this study, which represents the stretching, compression, shearing within the surface of the slab and also accounts for the thickening or thinning in the slab normal direction.

Equation (2.3.3.10) gives us the strain-rate tensor as the basis for quantitatively measure the in-plane deformation. But how do we actually calculate it using a fixed global Cartesian coordinate system given that our knowledge on the flow field is limited to only the surface part ? i.e. if we have the surface flow field $\mathbf{V}^T = (u, v, w)$ that is only well-defined on the surface $Z = z(x, y)$, and always stays on the surface. To force the flow to stay on the surface everywhere, we must have

$$w = u(z_x) + v(z_y), \quad \text{where} \quad z_x = \frac{\partial z}{\partial x}, \quad z_y = \frac{\partial z}{\partial y} \quad (2.3.3.11)$$

but if we don't have full information on the complete flow field, we won't be able to evaluate $\nabla \mathbf{V}^T$ and thus \mathbf{D} . The answer here is that although \mathbf{L} demands full information of \mathbf{V}^T , $\mathbf{P} \cdot \mathbf{L} \cdot \mathbf{P}^T$ doesn't; in fact, it needs only informations of \mathbf{V}^T on the surface.

For any point (x,y,z) located on the surface $Z=z(x,y)$, vectors $\mathbf{a}^T = (1,0,z_x)$ and $\mathbf{b}^T = (0,1,z_y)$ are always tangential to the surface, so the local unit normal vector would be

$$\begin{aligned}\widehat{\mathbf{e}}_n &= \frac{\mathbf{a} \times \mathbf{b}}{|\mathbf{a} \times \mathbf{b}|} \\ &= A^{-1}(-z_x \widehat{\mathbf{e}}_x - z_y \widehat{\mathbf{e}}_y + \widehat{\mathbf{e}}_z), \quad \text{where } A = (1+z_x^2+z_y^2)^{1/2} \\ \widehat{\mathbf{e}}_n \widehat{\mathbf{e}}_n &= A^{-2} \begin{bmatrix} z_x^2 & z_x z_y & -z_x \\ z_x z_y & z_y^2 & -z_y \\ -z_x & -z_y & 1 \end{bmatrix} \\ \mathbf{P} = \mathbf{I} - \widehat{\mathbf{e}}_n \widehat{\mathbf{e}}_n &= A^{-2} \begin{bmatrix} 1+z_y^2 & -z_x z_y & z_x \\ -z_x z_y & 1+z_x^2 & z_y \\ z_x & z_y & z_x^2+z_y^2 \end{bmatrix} \quad \text{_____ (2.3.3.12)}\end{aligned}$$

Thus,

$$\begin{aligned}\mathbf{P} \cdot \mathbf{L} \cdot \mathbf{P}^T &= (A^{-2} \begin{bmatrix} (1+z_y^2)(\frac{\partial}{\partial x} + z_x \frac{\partial}{\partial z}) - z_x z_y (\frac{\partial}{\partial y} + z_y \frac{\partial}{\partial z}) \\ -z_x z_y (\frac{\partial}{\partial x} + z_x \frac{\partial}{\partial z}) + (1+z_x^2)(\frac{\partial}{\partial y} + z_y \frac{\partial}{\partial z}) \\ z_x (\frac{\partial}{\partial x} + z_x \frac{\partial}{\partial z}) + z_y (\frac{\partial}{\partial y} + z_y \frac{\partial}{\partial z}) \end{bmatrix} \mathbf{V}^T) \cdot \mathbf{P}^T \quad \text{_____ (2.3.3.13)}\end{aligned}$$

Now, when an arbitrary function f is said to be well-defined on the surface $Z=z(x,y)$, it means that the variation of f along any direction within the surface is also well-defined. The previously defined vectors \mathbf{a} , \mathbf{b} are two of such vectors, so that

$$\begin{aligned}\frac{\partial f}{\partial a} &= (\mathbf{a} \cdot \nabla) f = \frac{\partial f}{\partial x} + z_x \frac{\partial f}{\partial z} \\ \frac{\partial f}{\partial b} &= (\mathbf{b} \cdot \nabla) f = \frac{\partial f}{\partial y} + z_y \frac{\partial f}{\partial z}\end{aligned}\quad (2.3.3.14)$$

are completely defined by the surface information of f only. It is

$$\frac{\partial f}{\partial n} = (\widehat{\mathbf{e}}_n \cdot \nabla) f = A^{-2} \left(-z_x \frac{\partial f}{\partial x} - z_y \frac{\partial f}{\partial y} + \frac{\partial f}{\partial z} \right) \quad (2.3.3.15)$$

that is not constrained by the surface information, i.e. depends on the function value outside the surface. This implies that if we have two 3-D flow field $\mathbf{V}_{(1)}$ and $\mathbf{V}_{(2)}$ that are in general not the same but are identical on the surface \mathbf{Z} , then although in general \mathbf{L} and thus \mathbf{D} are different, but $\mathbf{P} \cdot \mathbf{L} \cdot \mathbf{P}^T$ evaluated on the surface \mathbf{Z} for both of these flow field will be exactly the same, and thus \mathbf{D}^{PP} are identical. In other words, \mathbf{D}^{PP} and $\widetilde{\mathbf{D}}^{PP}$ is independent of any information outside the surface \mathbf{Z} .

2.3.4 Mapping the 3-D problem to 2-D space

Previous discussion on the independence of \mathbf{D}^{PP} and $\widetilde{\mathbf{D}}^{PP}$ with respect to the information of flow field outside the surface may seem trivial and redundant since by definition they should rely merely on the knowledge of flow on the surface. But it highlights one important point in terms of actually computing \mathbf{D}^{PP} . That is, instead of calculating $\nabla \mathbf{V}^T$ directly, note that for any point located on the surface $z=z(x,y)$, the function u can be written as

$$u = u(x, y, z) = u(x, y, z(x, y)) = u^*(x, y)$$

Evaluating the differential:

$$\begin{aligned}du &= u_x dx + u_y dy + u_z dz = u_x dx + u_y dy + u_z (z_x dx + z_y dy) \\ &= (u_x + u_z z_x) dx + (u_y + u_z z_y) dy \\ &= u_x^* dx + u_y^* dy\end{aligned}$$

we see that

$$\begin{aligned} u_x^* &= u_x + u_z z_x \\ u_y^* &= u_y + u_z z_y \end{aligned} \quad (2.3.4.1)$$

using Equation (2.3.4.1) we can rewrite Equation (2.3.3.13) as

$$\mathbf{P} \cdot \mathbf{L} \cdot \mathbf{P}^T = \mathbf{P} \cdot \begin{bmatrix} u_x^* & v_x^* & w_x^* \\ u_y^* & v_y^* & w_y^* \\ 0 & 0 & 0 \end{bmatrix} \cdot \mathbf{P}^T \quad (2.3.4.2)$$

The advantage of the equation above is that having information of geometry parameters (z_x, z_y) of the surface, we need to know the velocity field defined at the surface as function of (x,y) only, i.e. we don't need to know any flow out of the surface to evaluate the surface gradient of the velocity field, also, the fact that now the parameters z, u^*, v^*, w^* are all functions of (x,y) only makes it possible to map this 3-D problem to a 2-D space to be solved, this will become very useful in the numerical formulation discussed later. Note that from now on we'll drop the $*$ for velocity field.

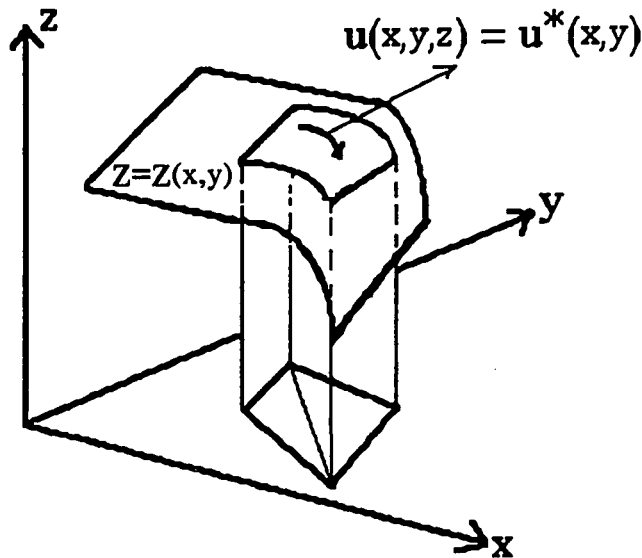


Figure 2.4 A surface flow $\mathbf{u}(x,y,z)$ defined on the non-Euclidean surface $z=z(x,y)$ embedded in the three-dimensional space can be rewrite as a function $\mathbf{u}^*(x,y)$ of x,y only.

2.4 Membrane deformation rates: Inverse Problem

2.4.1 Integrated total dissipation power

One natural way to define a global scalar measure of the membrane deformation rate mathematically, is to take the simple L^2 norm of the tensor $\tilde{\mathbf{D}}^{pp}$:

$$I = \iint [\tilde{D}^{pp}_{ij} \tilde{D}^{pp}_{ij}] dA$$

Once we have calculated \mathbf{D}^{pp} , then from Equations (2.3.3.8), (2.3.3.9) and (2.3.3.10)

$$I = \iint [D^{pp}_{ij} D^{pp}_{ij} + (D^{pp}_{ii})^2] dA \quad \text{_____} \quad (2.4.1.1)$$

Notice that for a Newtonian flow with constant and isotropic viscosity μ , the total dissipation power is

$$\frac{H}{2} \int \boldsymbol{\tau} : \dot{\boldsymbol{\epsilon}} dA = \frac{H \mu}{2} \int \dot{\boldsymbol{\epsilon}} : \dot{\boldsymbol{\epsilon}} dA \quad \text{_____} \quad (2.4.1.2)$$

where H is the slab thickness,

$\boldsymbol{\tau}$ is the stress tensor,

$\dot{\boldsymbol{\epsilon}}$ is the strain-rate tensor .

the L^2 norm measure defined in Equation (2.4.1.1) is thus proportional to the dissipation power of the particular flow field we use to define the subduction process. Finlayson [1972] shows that in the ideal closed system with proper boundary conditions, minimizing the dissipation power is the appropriate variational principle governing the flow motion for both the Newtonian flow and the Power-Law flow. Our formulation is not a closed system in that we have not included all the dynamics that control the flow. Nevertheless, we are going to minimize the functional (2.4.1.1) to define a flow field

with the least amount of membrane deformation rates that is compatible to the geometric constrains setup by the slab configuration. In other words, we are not claiming that the flow field of our calculation is the flow representing the actual subduction process. Rather, the calculated flow field is the optimal flow field with the minimum membrane deformation rate among all the admissible flow field that are compatible with the geometric constrains.

Similar expression of Equation (2.4.1.1) for Power-law rheology is thus

$$I = \iint [D^{pp}_{ij}D^{pp}_{ij} + (D^{pp}_{ii})^2]^{\frac{1+1/n}{2}} dA \quad (2.4.1.3)$$

Again, physically, this is the dissipation power for the flow field with a Power-law rheology. Notice that, when $n \rightarrow \infty$ this functional is simply the L^1 norm measure of the membrane strain-rate tensor. In summary, Equations (2.4.1.1), (2.4.1.3) then mathematically complete our definition of "the configuration with the least amount of deformation", i.e. in order to find the optimal configuration, the scalar quantity I is what needs to be minimized.

A brief summary of the problem can now be mathematically posed as the following. We want to determine the flow field $[u(x,y),v(x,y),w(x,y)]$ and the slab geometry $z(x,y)$ associated with the subduction process which minimizes the integrated total dissipation power I , and satisfies the boundary constrains that

- (1). The flow field before entering the trench boundary is completely prescribed by the known relative plate convergence motion.
- (2). The geometry of the oceanic lithosphere before subduction overlays the surface of the earth and is thus part of a spherical cap.
- (3). The flow stays within the slab surface during subduction process, i.e. there is no flow across the surface.
- (4). The slab surface go through where position constrains are available, e.g. hypocenters of slab earthquakes.

$$\tilde{G}_{ij} = P_{is} G_{st} P_{jt} \quad , \quad D^{pp}_{ij} = \frac{1}{2} (\tilde{G}_{ij} + \tilde{G}_{ji}) \quad \text{_____} \quad (2.4.1.4)$$

where

$$G = \begin{bmatrix} u_x & v_x & w_x \\ u_y & v_y & w_y \\ 0 & 0 & 0 \end{bmatrix}$$

$$P = A^{-2} \begin{bmatrix} 1+z_y^2 & -z_x z_y & z_x \\ -z_x z_y & 1+z_x^2 & z_y \\ z_x & z_y & z_x^2+z_y^2 \end{bmatrix} \quad , \quad A = \sqrt{1+z_x^2+z_y^2}$$

2.4.2 Inverting for flow field only

In this section we hold the geometry, and therefore the projection operators, fixed and invert for the flow velocity field, we adjust the flow field in order to find the least amount of deformation rates associated with the process of moving and contorting from one geometric configuration (the spherical cap oceanic lithosphere) into a different configuration (the subducted slab).

2.4.2.a Linear inversion for Newtonian Rheology

For a flow with Newtonian rheology, the inversion for flow field is then linear. Suppose $[\phi]$ is a vector of parameters that specify the functions $u(x,y)$, $v(x,y)$ to be determined, then

$$\frac{\partial I}{\partial [\phi]} = 2 \iint [D^{pp}_{ij} \frac{\partial D^{pp}_{ij}}{\partial [\phi]} + D^{pp}_{ii} \frac{\partial D^{pp}_{jj}}{\partial [\phi]}] dA = 0$$

$$\frac{\partial D^{pp}_{ij}}{\partial [\phi]} = \frac{1}{2} (P_{is} \frac{\partial G_{st} P_{jt}}{\partial [\phi]} + P_{is} \frac{\partial G_{ts} P_{jt}}{\partial [\phi]}) \quad \text{_____} \quad (2.4.2.a.1)$$

2.4.2.b Non-linear inversion for Power-Law Rheology

For power-law rheology, the inversion is similar except that it's no longer linear,

$$\frac{\partial I}{\partial [\phi]} = (1 + \frac{1}{n}) \iint I_0 [D^{pp}_{ij} \frac{\partial D^{pp}_{ij}}{\partial [\phi]} + D^{pp}_{ii} \frac{\partial D^{pp}_{ij}}{\partial [\phi]}] dA = 0 \quad , \quad I_0 = [D^{pp}_{ij} D^{pp}_{ij} + (D^{pp}_{ii})^2]^{\frac{1-n}{2n}}$$

(2.4.2.b.1)

This inversion can be attacked by iterating from an initial Newtonian solution. And then by utilizing a "direct iteration method" [Zienkiewicz, 1977]; for each new iteration, use the previous solution to evaluate the weighting I_0 . Physically, the effects of the power-law rheology would be to concentrate the deformation, i.e. increase the contrast of the high vs. low deformation pattern.

2.4.3 Inverting simultaneously for the flow field and the slab geometry

2.4.3.a The non-linear inverse problem

The basic strategy in undertaking this complete inversion is briefly discussed in this section, more details on the non-linear optimization is discussed in Appendix.B. As usual, non-linear optimization starts with an initial model and then iterate it's way down to adjust increments on the adjustable variables in order to get to the sought minimum. In the n th step, we can expand the "dissipation power" functional I to be minimized near the model calculated in the previous $(n-1)$ th step by hyperbolic expansion [Bevington, 1969], i.e.

$$I^n \approx I^{n-1} - \beta_j (\Delta\phi)_j + \alpha_{jk} (\Delta\phi)_j (\Delta\phi)_k$$

$$\beta_j = - \left(\frac{\partial I}{\partial \phi_j} \right)_{n-1} \quad , \quad \alpha_{jk} = \frac{1}{2} \left(\frac{\partial^2 I}{\partial \phi_j \partial \phi_k} \right)_{n-1}$$

$$(\Delta\phi)_j = \phi_j^n - \phi_j^{n-1}$$

(2.4.3.a.1)

To make I^n minimum

$$\frac{\partial I^n}{\partial (\Delta\phi)_j} = -\beta_j + \alpha_{jk}(\Delta\phi)_k = 0 \quad (2.4.3.a.2)$$

solve the linear system of equations

$$\alpha(\Delta\phi) = \beta \quad (2.4.3.a.3)$$

for $\Delta\phi$.

Creeping vs. Jumping iteration & Damping vs. Smoothing regularization.

Generally, Equation (2.4.3.a.3) is an ill-posed problem, certain regularization has to be imposed to stabilize the inversion. Scales et. al. [1990] discussed different regularizations and their effects on the convergence rate for Least-Square problems. Discussion for more general optimization problems is briefly shown here.

First of all, there are two alternatives to approach Equation (2.4.3.a.3), the Creeping algorithm:

$$(c)\phi^n = \phi^{n-1} + \alpha^\dagger \beta \quad (2.4.3.a.4)$$

and the Jumping algorithm :

$$(J)\phi^n = \alpha^\dagger (\alpha\phi^{n-1} + \beta) \quad (2.4.3.a.5)$$

where α^\dagger is the generalized inverse of α . Comparing Equations (2.4.3.a.4) and (2.4.3.a.5),

$$(J)\phi^n - (c)\phi^n = [\alpha^\dagger \alpha - I]\phi^{n-1} \quad (2.4.3.a.6)$$

the difference of these two solutions depends on the way how the generalized inverse of α is applied. In Equation (2.4.3.a.4), α^\dagger operates on β directly, implying that $\Delta\phi$ is the

minimum-norm solution. The term "creeping" simply indicate that in each iteration during the optimization process, the perturbation from the initial model are minimized. On the other hand, in Equation (2.4.3.a.5) the way α^\dagger operates forces the solution vector ϕ itself to be minimize, and is thus refereed as "jumping" algorithm. In other words, the difference in Equation (2.4.3.a.6) are solely components of the initial model in the null space of α^\dagger . If the initial model contains components within the null space of α^\dagger , these components will be sorted out by the jumping algorithm but not by the creeping algorithm.

The most common ways to regularize Equation (2.4.3.a.3) are usually achieved by imposing an additional optimization constrain or penalty of the form:

$$\chi = I + \lambda[(R\phi)^T(R\phi)] \quad (2.4.3.a.7a)$$

or

$$\chi = I + \lambda[(R(\Delta\phi))^T(R(\Delta\phi))] \quad (2.4.3.a.7b)$$

when $R=I$, Equation (2.4.3.a.7b) becomes

$$\chi = I + \lambda\|\Delta\phi\|^2 \quad (2.4.3.a.8)$$

Rewrite Equations (2.4.3.a.1), (2.4.3.a.2)

$$\chi = I^{n-1} - \beta_j(\Delta\phi)_j + \alpha_{jk}(\Delta\phi)_j(\Delta\phi)_k + \lambda\|\Delta\phi\|^2$$

$$\frac{\partial\chi}{\partial(\Delta\phi)_j} = -\beta_j + \alpha_{jk}(\Delta\phi)_k + 2\lambda\delta_{jk}(\Delta\phi)_k \quad (2.4.3.a.9)$$

i.e.

$$[\alpha + \lambda I](\Delta\phi) = \beta \quad (2.4.3.a.10a)$$

similarly, if we apply the same derivation for Equation (2.4.3.a.7a), we get

$$[\alpha + \lambda \mathbf{I}](\Delta\phi) = \beta - \lambda \phi \quad (2.4.3.a.10b)$$

From discussions in the previous section, clearly, if we choose regularization Equation (2.4.3.a.10a), we will be using a "creeping" scheme where the perturbations in each step are minimized. This is a simple but robust way to stabilize the solution of Equation (2.4.3.a.3) although the convergence is usually slow. From the physical point of view, if we are able to make good initial guess then the creeping scheme can in a sense display the evolution of the structure during each iteration.

Alternatively, in the other popular "smoothing" regularization, $\mathbf{R} = \nabla^2$ is used instead of $\mathbf{R} = \mathbf{I}$, we then have

$$[\alpha + \lambda (\nabla^2)^T (\nabla^2)](\Delta\phi) = \beta \quad (2.4.3.a.11a)$$

and

$$[\alpha + \lambda (\nabla^2)^T (\nabla^2)](\Delta\phi) = \beta - \lambda \phi \quad (2.4.3.a.11b)$$

2.4.3.b Parameterization and Finite Element Interpolation

To formulate a discrete parameterization of the flow field by a finite number of variables, we first cover the region of interest by a set of inter-connected non-overlapping triangles. Each vertex that is shared by the neighboring triangular element is a "node", and we assign a global label to it, say we thus have N_e elements and N_p nodes. This mesh generating procedure for a curved boundary can be easily automated as discussed in Appendix C. In a chosen Cartesian coordinate system, associate 5 degrees of freedom to each node: the x- and y-components of the velocity vector (u and v), the height (or the depth) (z), and the slopes (z_x and z_y) of the surface. As discussed in section (2.3.4), all the variables can be transformed to be functions of x, y only, and the actual mesh we will be dealing with is the projection of the original mesh onto the X-Y plane as shown in Figure 2.4, this greatly simplifies the computation.

Using the nodal variables and the triangular mesh thus constructed, we can then form patchwise continuous representations of the flow field. To get robust estimates of various spatial derivatives of the flow field using these patchwise continuous representation in order to get approximations of the membrane strain rate tensor, certain continuity (or compatibility) condition have to be considered.

Linear C^0 element

The easiest way to devise a patchwise representation of a certain function based on a triangular grid is to simply assume that the function value varies linearly within a single element. For an element with nodal variables $[f_1, f_2, f_3]$, we assume that within the element

$$f(x,y)=ax+by+c \quad \text{-----} \quad (2.4.3.b.1)$$

Since we have f_1, f_2, f_3 at the vertices to determine the three unknown coefficients a, b, c , f is completely determined within the element. Furthermore, since two neighboring element share one common edge and two nodes as shown in Figure 2.5, the values of f interpolated on the common edge are uniquely specified by the two common nodal variables. This then guarantees that the function f is continuous across any element boundary. This continuity is true for f but not for derivatives of f , and is thus called C^0 continuity.

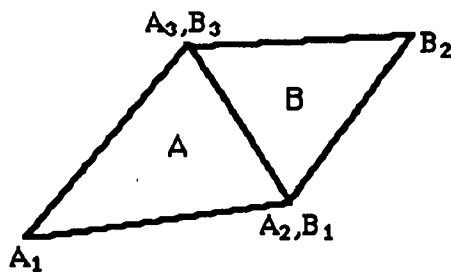


Figure 2.5 Continuity across the shared boundary of two neighboring triangular elements has to be secured.

In the Finite Element Method (FEM) community, the interpolation scheme is usually expressed in terms of the "Local Area coordinate" and "Shape functions", which simplify the algebra involved. The "Local Area coordinate" is defined as shown in Figure

2.6, where any point $P(x,y)$ within the element can also be addressed by a new set of coordinate (L_1, L_2, L_3) , where

$$L_3 = \frac{\text{Area of } pq_1q_2}{\text{Area of } q_3q_1q_2}$$

and L_1, L_2 are defined in the similar fashion.

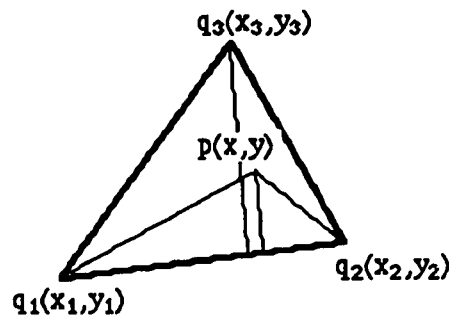


Figure 2.6 Definition of local area coordinate system.

It can be shown that in general, the transformation between these two coordinate systems is

$$x = L_i x_i, \quad y = L_i y_i, \quad i = 1, 2, 3$$

$$L_i = a_i x + b_i y + c_i, \quad a_i = (y_j - y_k)/2, \quad b_i = (x_k - x_j)/2, \quad c_i = (x_j y_k - x_k y_j)/2,$$

$$i, j, k \text{ is in cyclic permutation and ranges from 1 to 3.} \quad \text{_____ (2.4.3.b.2)}$$

Having defined the Local Area coordinate system, we can then express the representation of the function in terms of the "Shape functions";

$$f = N_i^1 f_i, \quad \partial f / \partial x = (\partial N_i^1 / \partial x) f_i, \quad \partial f / \partial y = (\partial N_i^1 / \partial y) f_i \quad \text{_____ (2.4.3.b.3)}$$

N_i^1 is the shape function which is function of L_i , f_i are nodal variables. In the simple linear element;

$$N_i^1 = L_i, \quad (\partial N_i^1 / \partial x)_i = \partial L_i / \partial x = a_i, \quad (\partial N_i^1 / \partial y)_i = \partial L_i / \partial y = b_i \quad \text{_____ (2.4.3.b.4)}$$

Quadratic C^0 element

As shown in Figure 2.7, this element has 6 nodes, i.e. 3 vertices and 3 mid-side points to allow quadratic variations of f in the element,

$$f = N^2_i f_i \quad , \quad \partial f / \partial x = (\partial N^2 / \partial x)_i f_i \quad , \quad \partial f / \partial y = (\partial N^2 / \partial y)_i f_i \quad , \quad i \text{ ranges from 1 to 6.}$$

$$N^2_{2k-1} = L_k(2L_{k-1}-1),$$

$$N^2_{2k} = 4L_k L_{k+1} \quad , \quad k \text{ ranges from 1 to 3, if } k+1 > 3 \text{ then } k+1 = 1. \quad \text{---(2.4.3.b.5)}$$

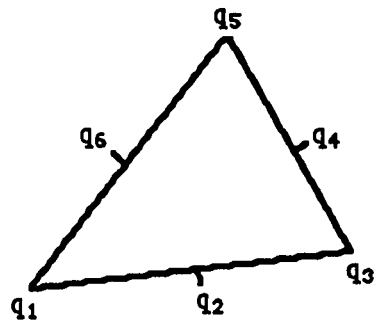


Figure 2.7 Nodes location of the quadratic C^0 element.

Clough-Tocher cubic C^1 element

For reasons to be discussed later, we will need a C^1 element for the interpolation of z , i.e. the continuity of z , z_x , z_y across the element boundaries have to be all secured. It has been pointed out [Akima, 1970] that a complete 21 degrees of freedom quintic polynomial is needed to achieve this if we follow the usual procedure to construct the shape functions. Alternatively, by introducing a "seaming technique" [Clough and Tocher, 1965] Clough and Tocher were able to develop a 12 d.o.f cubic C^1 element which can then be further reduced to a 9 d.o.f element by sacrificing some flexibility [Lancaster and Salkauskas, 1988]. General configuration of the element is shown in Figure 2.8, the shape functions of this element can be found in Lancaster and Salkauskas [1988].

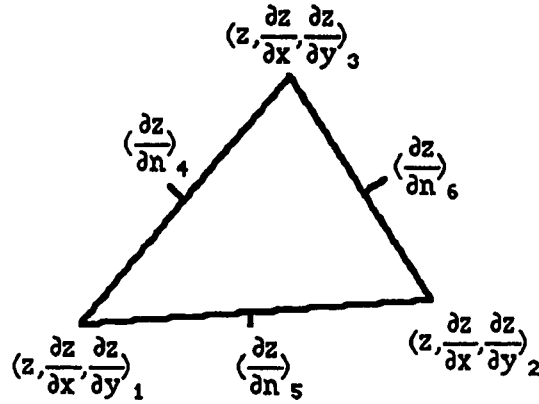


Figure 2.8 Nodal variables of the C^1 Clough-Tocher element.

2.4.3.c Setting up the inversion

To simplify the computation, we tend to utilize lower order interpolation wherever it is possible. For the parameters u, v we thus choose the linear element. To make the flow field stay on the surface, the constraint $w = uz_x + vz_y$ must be satisfied. Under this condition, in spite of the fact that w is not an explicit variable used in the parameterization (as it can always be computed from other parameters), the continuity of the implicit computation of w must still be insured, otherwise, we would have tears in the flow field which is not only physically unrealistic but also would greatly underestimate the membrane deformation. This then leaves no other alternative than to use at least C^1 interpolation for z to guarantee the continuity of z_x, z_y and thus w . This is the basic rationale for using the Clough-Tocher element for z . Again, although w can be written implicitly in terms of u, v, z_x, z_y , the lowest order interpolation for w would be quadratic to account for variation of w originating from both variations of (u, v) and (z_x, z_y) .

Another advantage of utilizing C^1 interpolation for z is that if we choose to go with the "Smoothing" regularization as discussed in section (II.3.2.a), it is very convenient to write down the R operator by

$$R_{ij} = (\nabla^2 N^3_i)(\nabla^2 N^3_j), \quad i, j \text{ ranges from 1 to 9}$$

N^3_i are the nine shape functions of Clough-Tocher element _____(2.4.3.c.1)

In summary, for the mesh constructed on the X-Y plane in a region mapped by projecting the surface region on the X-Y plane, we parameterize each node with 5 d.o.f (u, v, z, z_x , z_y) and the patchwise representations for a single element are

$$\begin{aligned} u &= N^1_i u_i, \quad u_x = \frac{\partial N^1_i}{\partial x} u_i, \quad u_y = \frac{\partial N^1_i}{\partial y} u_i \\ v &= N^1_i v_i, \quad v_x = \frac{\partial N^1_i}{\partial x} v_i, \quad v_y = \frac{\partial N^1_i}{\partial y} v_i \end{aligned} \quad \text{_____ (2.4.3.c.2a)}$$

$$\begin{aligned} w &= N^2_i w_i, \quad w_x = \frac{\partial N^2_i}{\partial x} w_i, \quad w_y = \frac{\partial N^2_i}{\partial y} w_i \\ w_{2k-1} &= u_k (z_x)_k + v_k (z_y)_k, \quad \text{no summation} \\ w_{2k} &= \left(\frac{u_k + u_{k+1}}{2} \right) (z_x)_k^m + \left(\frac{v_k + v_{k+1}}{2} \right) (z_y)_k^m \\ (z_x)_k^m, (z_y)_k^m &\text{ are } z_x, z_y \text{ evaluated at the } k\text{th mid-side.} \end{aligned} \quad \text{_____ (2.4.3.c.2b)}$$

$$\begin{aligned} z &= N^3_i z_i, \quad z_x = \frac{\partial N^3_i}{\partial x} z_i, \quad z_y = \frac{\partial N^3_i}{\partial y} z_i \\ z_1, z_4, z_7 & \quad \quad \quad z & \quad \quad \quad 1 \\ z_2, z_5, z_8 & \text{ are } z_x \text{ variables at vertex} & \quad \quad \quad 2 \\ z_3, z_6, z_9 & \quad \quad \quad z_y & \quad \quad \quad 3 \end{aligned} \quad \text{_____ (2.4.3.c.2c)}$$

We now have the complete representations that is at least C^0 in the velocity field and C^1 in the geometry, it is then straight forward to formulate the numerical scheme to undertake the inversion.

In a single element, with initial guesses on the five d.o.f for each vertex, we have 15 element d.o.f

$$\phi_{15 \times 1}^T = [(u, v, z, z_x, z_y)_i], \quad i=1,2,3 \quad \text{_____ (2.4.3.c.3)}$$

we can then calculate P, G, L, D according to Equations (2.4.1.4) and (2.4.3.c.2) and thus the integration

$$I^e = \iint [D_{ij}D_{ij} + (D_{ii})^2]^{\frac{1+1/n}{2}} dA$$

$$= \iint [D_{ij}D_{ij} + (D_{ii})^2]^{\frac{1+1/n}{2}} A dx dy$$

(as defined before, $A = \sqrt{1+z_x^2+z_y^2}$ is the area element at each point) _____ (2.4.3.c.4)

can be easily calculated by numerical integration scheme (e.g. Gauss' weighted sum algorithm [e.g. Zienkiewicz, 1977]).

To proceed with the inversion, we need to compute for each element the 15 by 15 α^e matrix and the 15 by 1 β^e vector as defined in Equations (2.4.3.a.2) and (2.4.3.a.3), the details of these derivation is presented in Appendix D.

2.4.4 The *Simple* experiment

The *Simple* experiment is designed to show both the forward computation of the membrane deformation and how the optimization works. Starting with a model geometry that is a spherical cap with radius 600 km, the minimum membrane deformation rate solution for this geometry is to have a rotational flow field on this surface. In fact, this is the only way to have a solution free from internal membrane deformation. We then slightly perturb this geometry by adding a round hill of height 30 km on top of the original spherical cap. An arbitrary rotational flow field is then imposed on this surface by entering the experimental region from the left edge. The first calculation is then to calculate the membrane deformation rates for this non-ideal configuration (Figure 2.9).

For the sake of comparing membrane deformation rates of different configurations, We defined the quantity

$$I' = \sqrt[n]{\frac{1+1/n}{n} \frac{I}{A}} \quad \text{_____} \quad (2.4.4.1)$$

where n is the power of the power-law rheology,

A is the total area of the surface,

I is the integrated total dissipation power defined in Equation (2.4.1.3)

This then represents root mean square effective strain-rate (RMS) for Newtonian rheology; and mean effective strain-rate (MES) for Power-Law rheology with $n=\infty$.

In Figure 2.9, the rotational flow field outside the anomalous region is free from any internal deformation while the flow crossing over the hill is first compressed in the flow direction facing the hill and laterally extended, and then the exact opposite mechanism can be observed for flow over the back side of the hill.

We performed the first optimization experiment by fixing this non-ideal model geometry, setting the boundary conditions on the left entering edge to have fixed incoming flow field and then invert the flow field within the experimental region that minimizes the total dissipation power (Figure 2.10). This experiment on inverting for the flow field only shows how the flow field responds by adjusting itself to reduce the membrane deformation rate caused by the hill. The result of this optimization as compared to the forward computation reduces the RMS by a factor of 2.5. A similar optimization experiment adopting Power-Law rheology ($n=10000$) is then undertaken (Figure 2.11) to compare with the previous Newtonian rheology experiment (Figure 2.10). Comparison between Figure 2.10 and Figure 2.11 clearly demonstrates the effects of the Power-Law rheology that it forces the deformation to be more concentrated.

A full inversion is then executed by allowing the geometry within the region to be adjusted simultaneously with the flow field. Ideally, the optimization iterations would converge to the strain-rate free solution with the geometry adjusted to the perfect spherical cap and the flow field be tuned to become pure rotational. The boundary conditions in this experiment are such that the geometry of the surface on the left edge is fixed and the flow field on the two corner points defining the left edge are fixed. The results shown in Figure 2.12 is a series of iterations. After 25th iteration where the overall mean effective strain-rate is reduced by a factor of 2000, essentially vanishing; the added hill has been

wiped away to force the surface back to the ideal spherical shape and the flow field is approaching a perfect rotational flow field, i.e. the solution converges to the ideal solution as expected. In summary, these experiments show the forward computation of the membrane deformation rate. It also confirms the capability of our inversion scheme to seek for the optimal geometry and flow field .

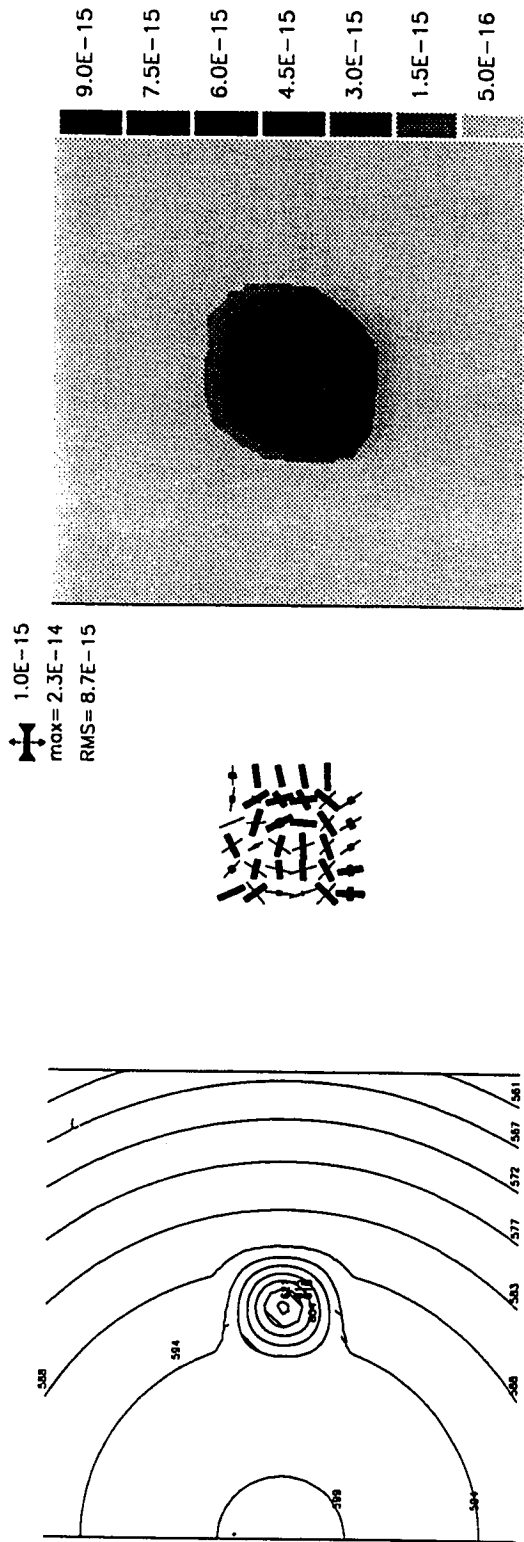


Figure 2.9 (a) Initial Model (b) Model surface is contoured with respect to a cartesian coordinate system. Forward computation is done for a spherical cap. Slab surface is contoured within the given geometry coming in from the left edge. (b) Orientations of principal axes of rotational flow field confined within the given geometry for compressional axes and thin line segments for tensional axes). On the upper right, the first row shows the scale key of saturation, the middle row shows the maximum magnitude associated with either axis plotted, and the third row is the root-mean-square (RMS) effective strain rate or the mean effective strain rate (MES) defined in Equation 2.4.4.1.

(c) Distribution pattern of effective strain rates defined by $\sqrt{\frac{1}{2} \dot{\epsilon} : \dot{\epsilon}}$, where $\dot{\epsilon}$ is the strain-rate tensor. The unit of strain-rate in all plots is sec^{-1} .

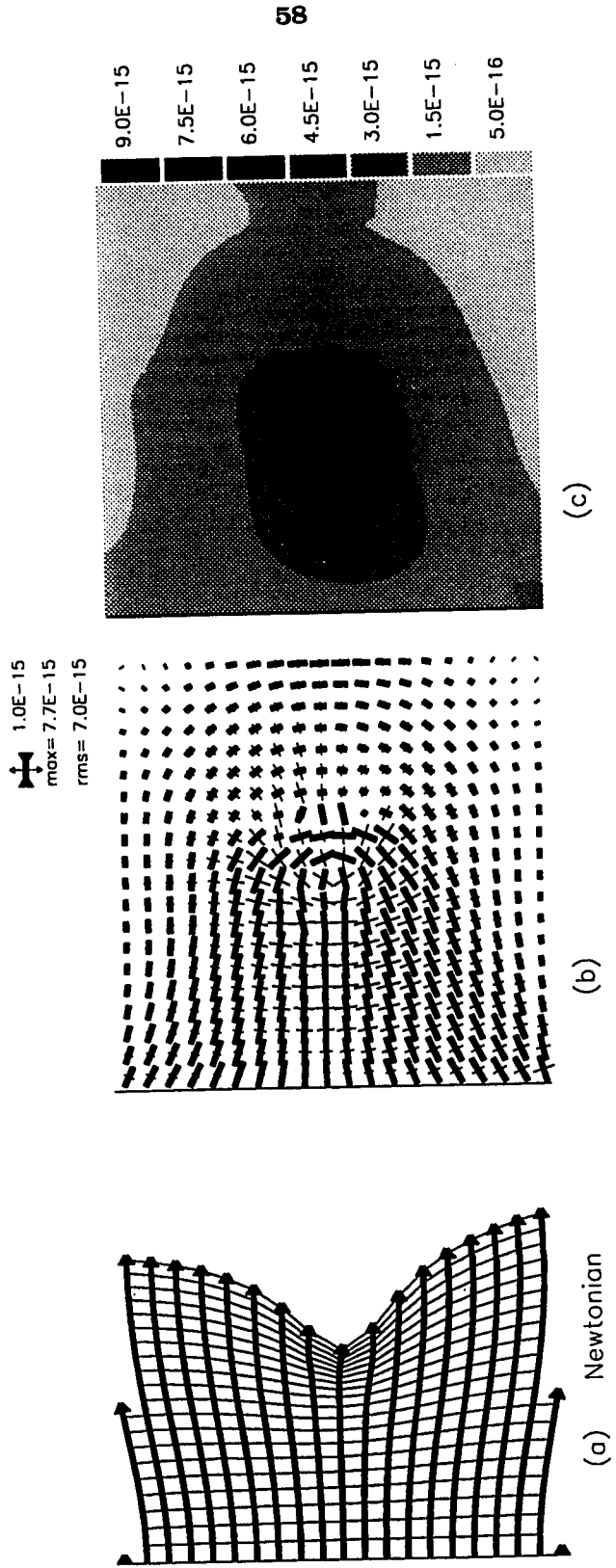


Figure 2.10 Optimal flow field, distribution of effective strain-rates and orientations of principal axes of membrane strain-rates (see the caption of Figure 2.9) obtained by fixing the model geometry of the *Simple* experiment (Figure 2.9(a)) and invert for the flow field only, Newtonian rheology.

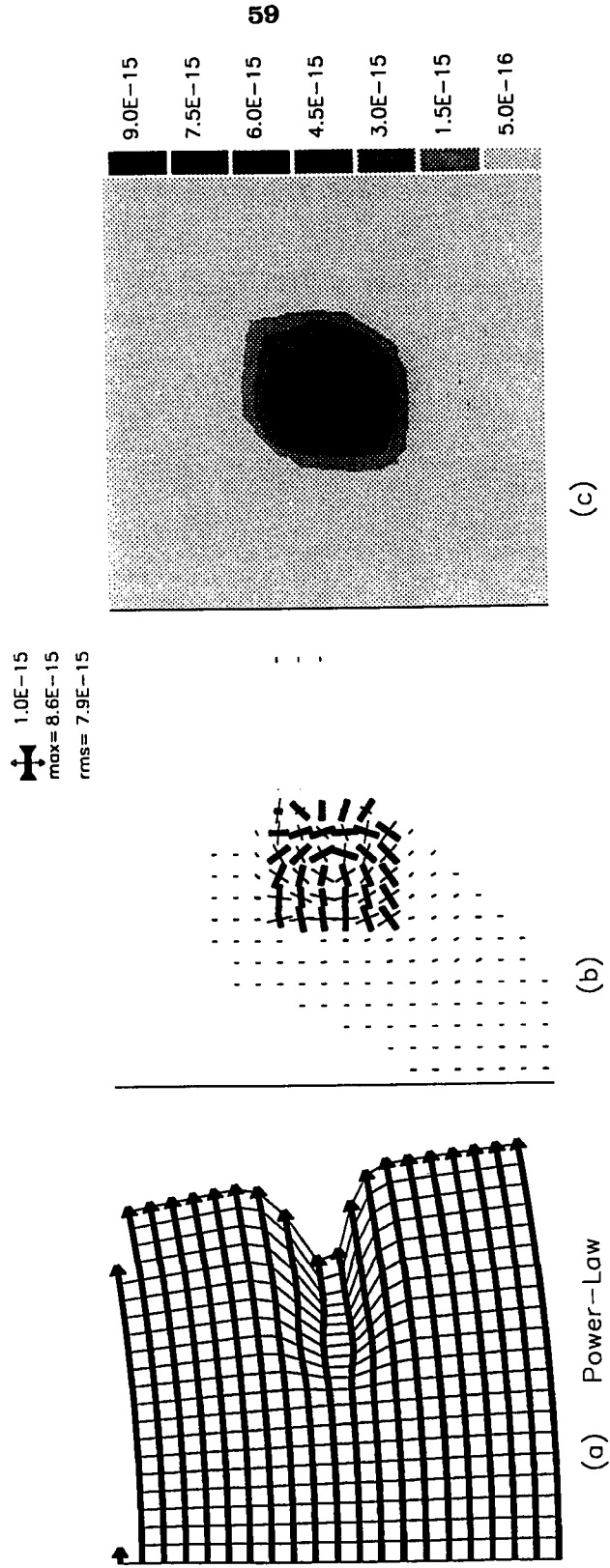


Figure 2.11 Optimal flow field, distribution of effective strain-rates and orientations of principal axes of membrane strain-rates (see the caption of Figure 2.9) obtained by fixing the model geometry of the *Simple* experiment (Figure 2.9(a)) and invert for the flow field only, Power-Law rheology ($n=100000$).

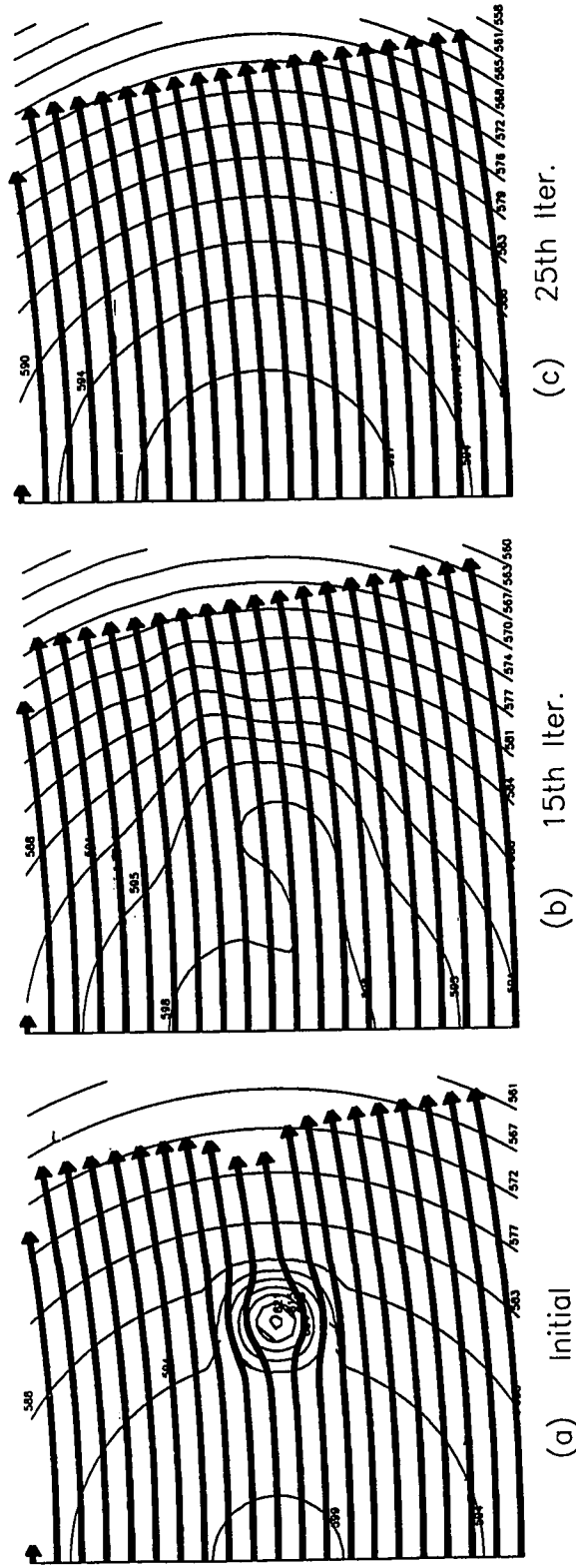


Figure 2.12 The flow field and the surface geometry for different iterations during the *Simple* experiment, complete inversion involving both the flow field and the model geometry: the initial model, 15th iteration and 25th iteration.

Chapter 3 Cascadia Subduction Zone

3.1 Tectonic framework and observations

Although lacking in typical signatures associated with subduction zones (deep oceanic trench, highly anomalous gravity profile etc.), the relative convergence between the Juan de Fuca Plate and the North American Plate along Vancouver Island and Washington-Oregon coast is well documented [e.g. Nishimura et. al., 1984; Riddihough, 1984]. Reproduced from Taber and Smith [1985], Figure 3.1a shows a brief sketch of the tectonic setup of this subduction zone and the estimated convergence rate along different parts of the trench. The trace of the trench, as shown in Figure 3.1a, changes its azimuth from nearly NS south of 47°N to approximately $\text{N}30^{\circ}\text{W}$ north of 48°N , and thus shows a concave oceanward bend adjacent to Olympic Peninsula. Landward of this sharp backward-curved (as compared with other trenches) bend, there are several anomalous geophysical and geological features:

(1). *Concentration of seismic activity.* The well-located microseismicity recorded by the Washington Regional Seismograph Network (WRSN) during the past two decades is concentrated in the vicinity of the Puget Sound Basin (Figure 3.2a). Extracting earthquakes within the down-going slab from both this catalogue and Pacific Geoscience Center catalogue, and also including events greater than magnitude 6 during the last century (Table 1) that are believed to occur within the subducted slab, we plot the total seismic moment release rate by first subdividing the area in Figure 3.3 into 20 km by 20 km map-view cells. We then convert bodywave magnitude to seismic moment release by using empirical formula:

$$\log M_0 = 2.4 \times m_b + 10.1 \quad \text{_____} \quad (3.1)$$

and sum all the seismic moment associated with slab earthquakes that falls within each cell. The distribution of seismic moment release of subcrustal events displays an even more pronounced concentration beneath the Puget Sound Basin, extending from Olympia, Washington to Victoria, British Columbia . As shown in Figure 3.3 the contrast is at least four orders of magnitude.

Table 1. Earthquakes with magnitude ~6 or larger that are inferred to be within the subducted slab in this century.

Date	Lat. (⁰ N)	Long. (⁰ E)	Dep.(Km)	Mag.	seismic moment release (dyne-cm)
01/11/09	48.7	-122.8	75	6.0	
11/13/39	47.4	-122.6	60	6.2	
02/15/46	47.3	-122.9	60	6.2	
04/13/49	47.1	-122.7	54	7.0	1.5×10^{26} [Baker & Langston, 1987]
04/29/65	47.4	-122.3	59	6.5	1.4×10^{26} [Langston & Blum, 1977]

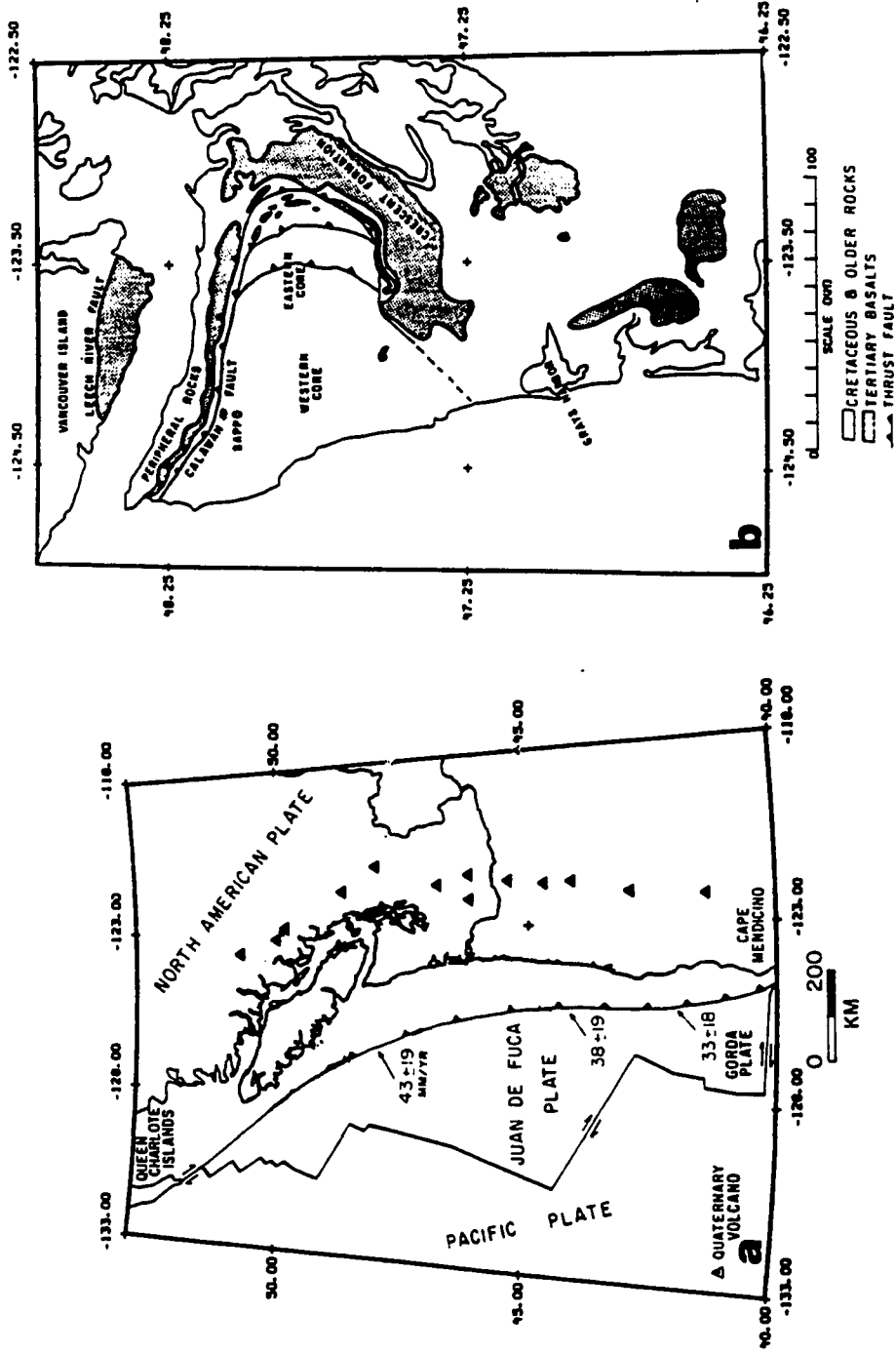


Figure 3.1 Reproduced from Taber and Smith (1985), (a) is a brief sketch of the tectonic framework of the Cascadia Subduction Zone, the convergence rate are adapted from Nishimura et al. (1984). (b) shows simplified Washington coast geology (after Cady, 1975).

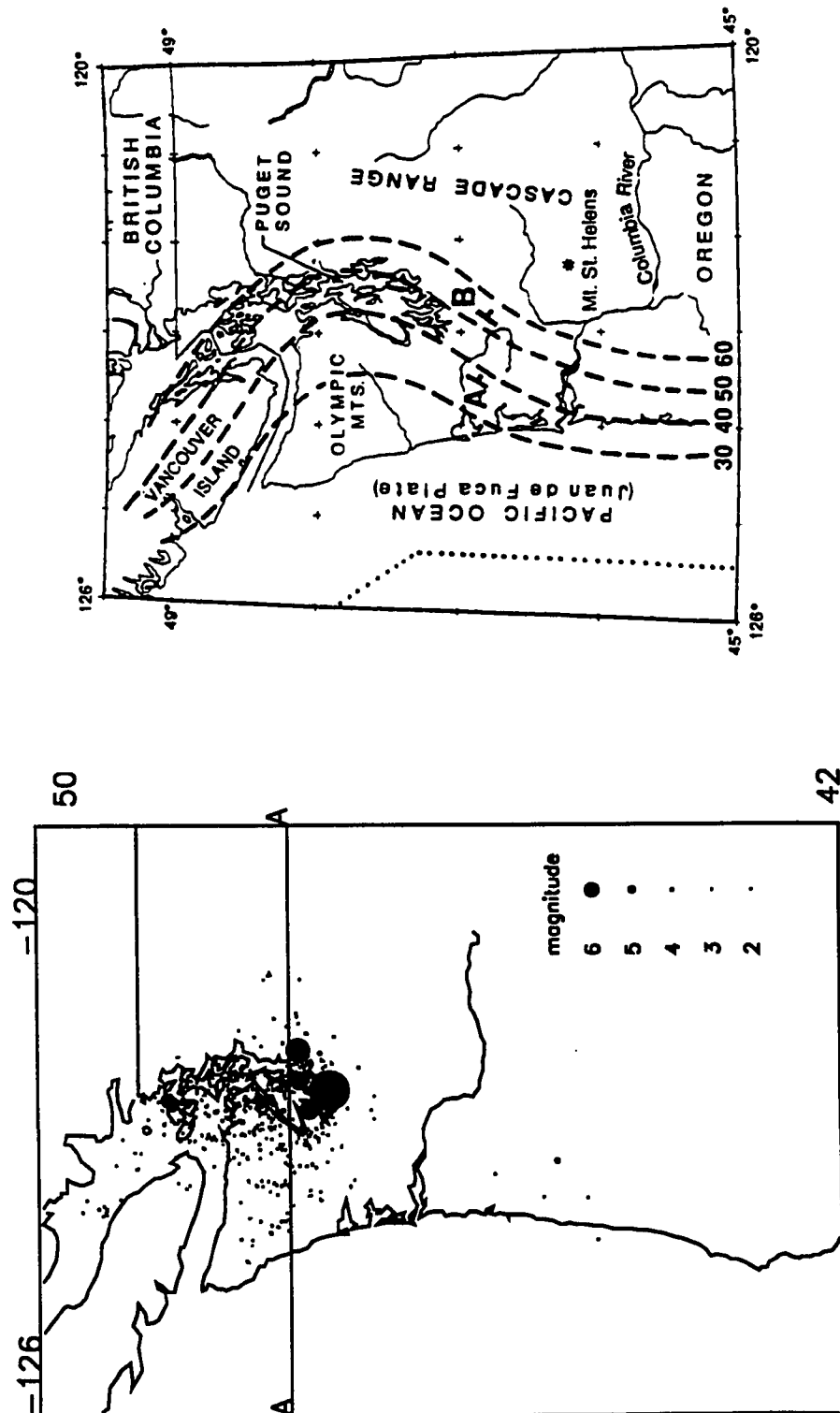


Figure 3.2 (a) Slab seismicity of the Cascadia Slab recorded by WRSN in the last two decades plus historical events with magnitude 6 or greater that are inferred to be within the subducted slab. (b) The Arch structure proposed by Crosson and Owens (1987).

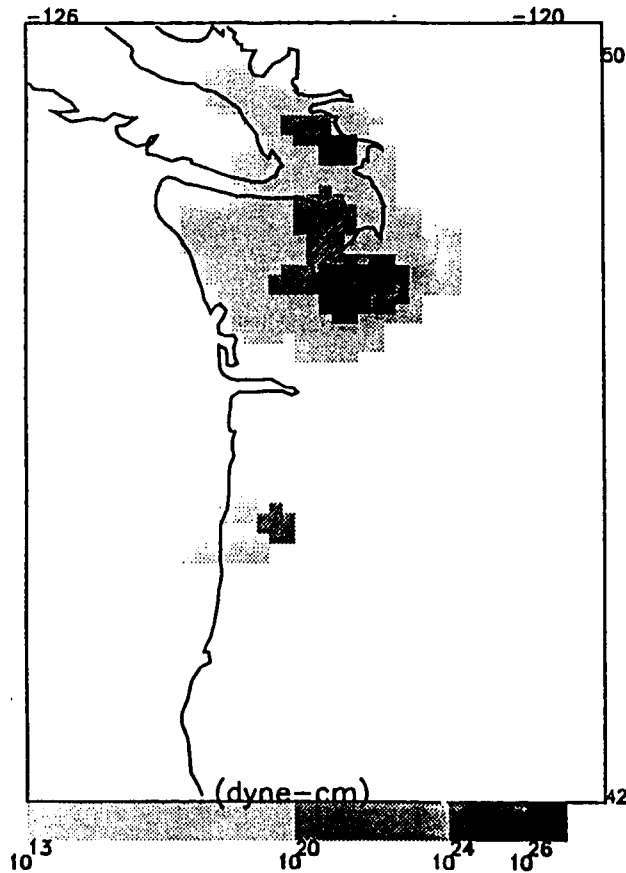


Figure 3.3 Total seismic moment release within the subducting plate of this century in the Cascadia Subduction Zone.

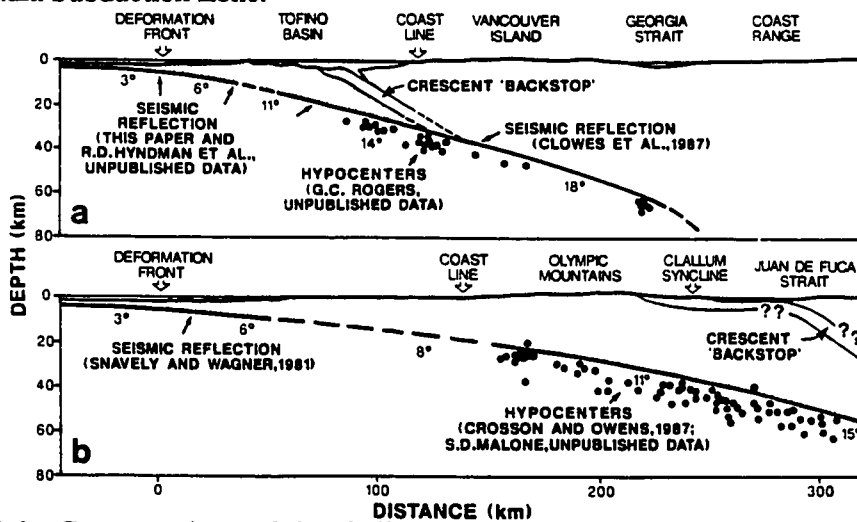


Figure 3.4 Cross sections of the shallow structure of the Cascadia slab underneath Vancouver Island and the Olympic Mountains [after Davis and Hyndman, 1989]

(2). *Slab geometry.* The low rate of subcrustal seismicity makes detailed mapping of the Wadati-Benioff Zone (WBZ) of this subduction zone rather difficult in general. However, a well defined cross section of the shallow slab seismicity beneath the Olympic Peninsula-Puget Sound area which is coincident with the axis of the trench bend, defines a generally planar WBZ with a dip around 10° [e.g. Crosson and Owens, 1987; see also Figure 3.4, Figure 3.5]. Rogers et al. [1990] on the other hand, shows that a steeper $\sim 18^{\circ}$ dip fits the seismicity underneath Vancouver Island which is consistent with the slab shape by combining both slab seismicity and evidence from seismic reflection studies shown in Figure 3.4 which is reproduced from Davis and Hyndman [1989]. The slab dip to the south underneath Oregon is poorly resolved, Weaver and Michaelson [1985] suggest that the Cascadia Slab is divided into two segments, and has steeper dips beneath the southern segment than beneath the northern segment. Four small earthquakes that are inferred to be slab events near Portland, North Oregon also suggest a possible steeper dip to the south. Figure 3.2b is reproduced from Crosson and Owens [1987] which shows a proposed *Arch* structure representing the possible buckling of the subducted Juan de Fuca plate [see also Weaver and Baker, 1988] with the arch axis coincident to the axis of the trench bend. This Arch structure is consistent with Teleseismic P-to-S receiver function analysis [Crosson and Owens, 1987; Owens et al., 1988; Lapp et al., 1990] and recent tomographic studies [Vandecar, 1991]. Also, tomographic images by Rasmussen and Humphrey [1988], and Vandecar [1991] indicate that after passing beneath the Puget-Sound region the slab goes to a steeper $\sim 55^{\circ}$ dip. Figure 3.5 shows the cross-sectional view (A-A' in Figure 3.2a) of the slab seismicity around the Puget-Sound region and our attempt to construct plausible slab shapes consistent with the shallow slab seismicity and the information from tomographic studies in greater depth, using the "minimum change of curvature" algorithm described in chapter 2. In Figure 3.5(a), the slab bends and unbends within 60 km from the deformation front to achieve a 10° dip, this shape is consistent with the shallow seismicity but not with the few deepest events and the tomographic results. Figure 3.5(b), on the other hand, shows a wider bending and unbending zone that the slab reaches 55° dip after it is already 200 km deep, the shape does not quite follow the trend delineated by the shallow seismicity. Finally, Figure 3.5(c) shows a slab shape that has two bending-unbending zones, the shallow one is identical to the one in Figure 3.5(a); the secondary bend occurs

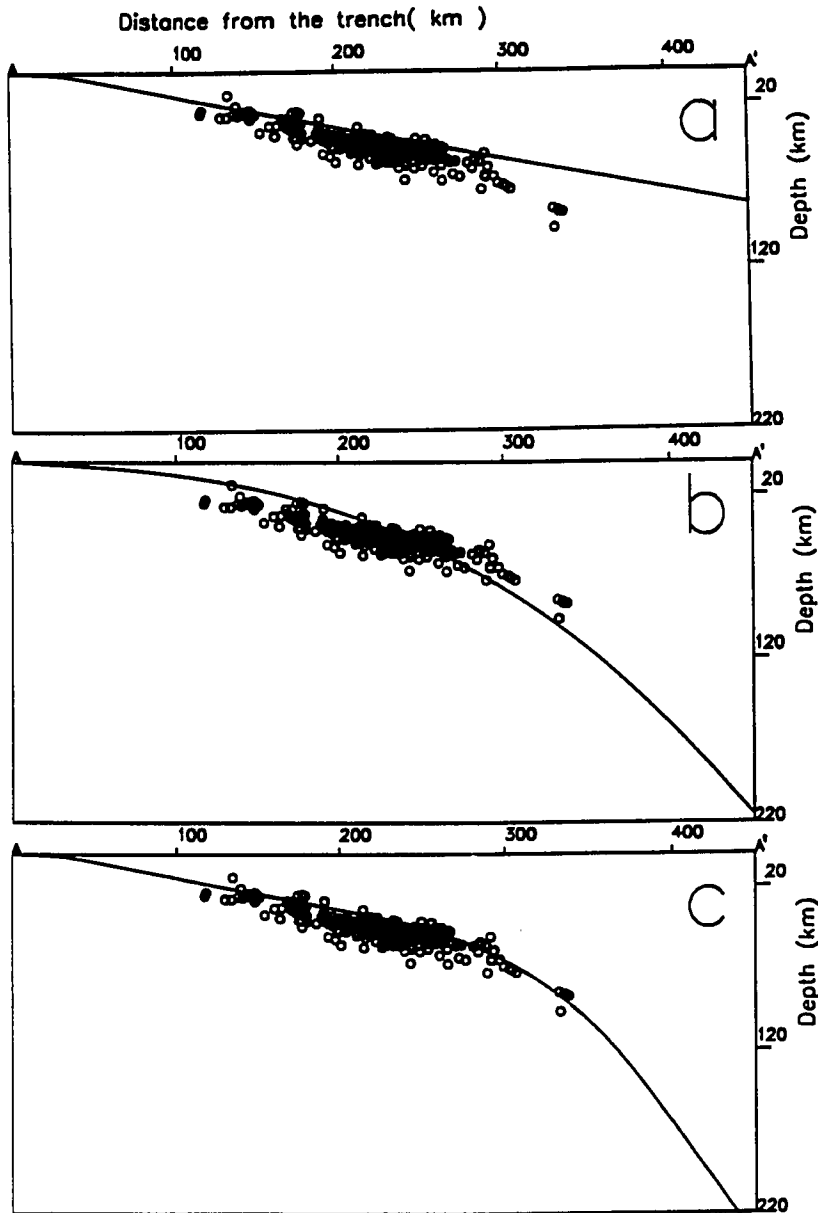


Figure 3.5 Slab seismicity projected on A-A' cross section marked on Figure 3.2a, "minimum change of curvature" algorithm described in chapter 2 are used to fit this cross-section. (a) Slab bends sharply in the first 50 km after passing through the trench to attain a 10° dip. (b) Slab bends smoothly to a dip of 55° when it reaches 250 km depth. (c) Slab shape composed by two bends, the shallower structure above 50 km depth is similar to (a) while a secondary smoother bend occurs between depth range 40-100 km where most of the slab earthquakes are concentrated.

in the depth range 40-100 km where most of the slab earthquakes are concentrated, this shape seems to be the favorable one that is consistent with most of the constraints.

In general, the proposed arch structure is compatible with other geophysical observations, e.g. seismic reflection and refraction studies: Snively and Wanger [1981], Green et al. [1986], Keach et al. [1986], Taber and Lewis [1986], Yorath et al. [1987]. However, the tightness of the arch and the slab structure at greater depth further north and south are not constrained by these observations.

(3). *Geological observations.* Coincident with the arch axis in Olympic Peninsula is the Eocene to Miocene highly deformed sedimentary and meta-sedimentary accretionary complex which is bounded to the north and east by the horseshoe shaped Eocene Crescent basalts [Taber and Cady, 1978; see Figure 3.1b]. The wide and deep accretionary wedge is confined to less than 100 km along arc. This unusual distribution has been attributed to the shallower slab dip beneath the Olympic Peninsula [Davis and Hyndman, 1989; Brandon and Calderwood, 1990]. By applying the "Critical Taper theory" of Davis et al. [1983], Davis and Hyndman [1989] argued that the slab dip angle is greater than 11° beneath the continental shelf around the Vancouver Island region, a dip too steep to allow upward growth of an accretionary prism; but to the south, beneath the Olympic Peninsula of Washington coast, the slab dips more gently on top of the proposed arch structure, allowing the accretionary prism to grow upward well above sea level to form the Olympic Mountains (Figure 3.4).

We postulate that the arching structure along with other important observations such as the concentration of slab related seismic activity (both in terms of the seismicity and the total seismic moment density) beneath Puget Sound that is coincident with the axes of the arch; and the anomalous high Olympic Mountain accretionary prism located on top of the arch and narrowly restricted around the landward corner of the bend of the trench are all linked directly or indirectly to the trench geometry. A primary goal of this study is thus set to investigate and quantify the possible relationship between these observations and the trench geometry in this subduction zone.

3.2 Examining the effect of the backward-curved trench

3.2.a Inverting for the optimal flow field: The *Constant-Dip* experiment

The fundamental goals in undertaking modeling experiments for this subduction zone are two fold. First, based on the coincidence of the axis of the concave-oceanward bend of the trench and the top of the proposed arch structure, we will examine the effect of the trench shape on the slab geometry. In other words, can the trench shape actually force the forming of the arch? A second question is: how much is membrane deformation reduced by forming the arch structure? Finally, how does the deformation regime correlate with the seismic activity? To keep the geometry simple, the deformation front is digitized and fit with a hyperbolic curve. A finite element mesh is generated for the curved boundary as described in Appendix A. We then construct a working model slab geometry with a constant 20° dip along the entire trench. The controlling cross section is built by the "minimum change of curvature" algorithm discussed in chapter 2, and has piecewise continuous change of curvature. Fixing the geometry of this working model, we invert for the flow field that will yield the least amount of membrane deformation rates. The boundary conditions are that on the surface of the Earth prior to entering the trench, the flow field is constrained to be the relative plate motions with the Euler pole set at $(29.11^\circ\text{N}, -112.72^\circ\text{E})$ and a angular velocity of 1.05° per million years [Nishimura et al, 1984]. The model geometry and the result from flow field inversion for this *Constant-Dip* model is shown in Figure 3.6. The bend of the trench shape clearly imposes a smoothly varying along-arc compression and reaches values as large as $2 \times 10^{-16} \text{ sec}^{-1}$ and integrates to strains of several percent.

3.2.b The full Inversion: The *Shallow-Dip* experiment

To test our hypothesis that the arch structure is a direct result of the unusual trench configuration, we formulated the inversion described in chapter 2 so that both the flow field and the slab geometry can be adjusted simultaneously in order to achieve the optimal configuration with the least amount of in-plane deformation. In other words, instead of fixing the slab geometry, we only set boundary conditions on the northern and

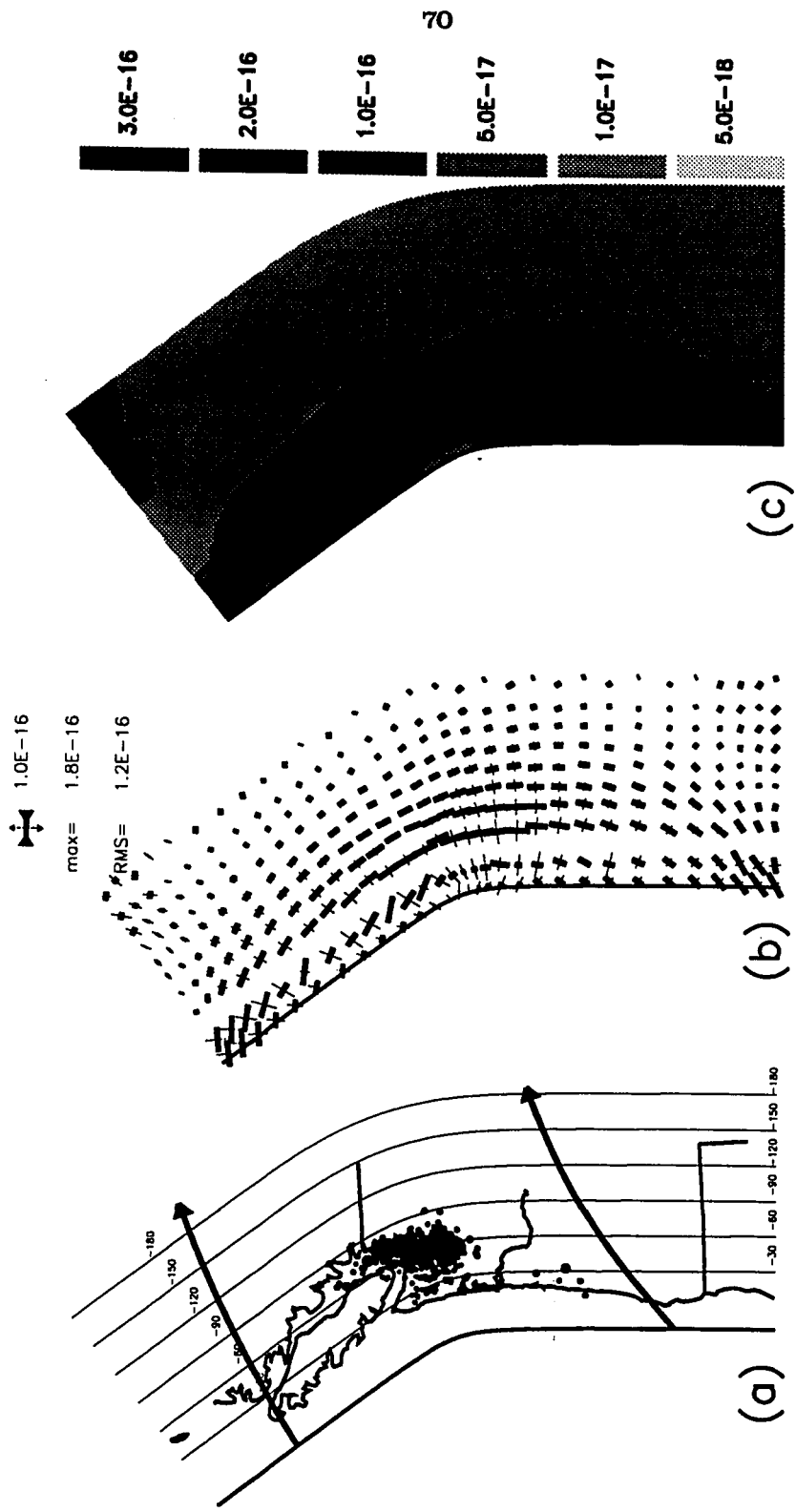


Figure 3.6 Flow field inversion of the *Constant-dip* experiment. (a) Depth contours showing the structure of the constant dip model of the Cascadia Subduction Zone. Also shown are the slab seismicity and inverted flow trajectory representing admissible subduction process that has the least amount of membrane deformation rate for this particular slab configuration. (b) Projected orientations of principal axes of membrane strain rates. (c) the distribution of effective strain rates. (see the figure caption of Figure 2.9 for explanations on (b) & (c))

southern edges of the study region to have a 20° dip below a depth of 50 km. Having defined the boundary conditions on the geometry, we set up the constant-dip slab geometry as in the previous flow field inversion experiment as the initial model. Boundary conditions on the flow field are identical to those used in the previous flow field inversion. We then let the solution iterate to convergence. The result for this *Shallow-Dip I* experiment (Figure 3.7) is a very tight arch that is consistent with the seismicity and the results from the receiver function analysis [Crosson and Owens, 1987; Owens et al., 1988; Lapp et al., 1990]. Figure 3.7(b), 3.7(c) shows the resulting pattern of the distribution of the in-plane deformation which clearly indicates a very effective reduction of the total in-plane deformation. The arch structure reduces the RMS effective strain-rate (see section 2.3.3 for definition) by a factor of five over the *Constant-Dip* experiment (compare Figure 3.6 and Figure 3.7). The concentration of strong along arc compression near the axis of the bend remains a distinct feature.

In the *Shallow-Dip II* experiment, a Power-law rheology ($n=100000$) instead of the Newtonian rheology for the *Shallow-Dip I* experiment is utilized. Results for this experiment is shown in Figure 3.8. As a comparison, this experiment yields more concentration of high effective strain-rate with higher contrast to the background (Figures 3.8(b) and 3.8(c)) as compared to the *Shallow-Dip I* experiment (Figures 3.7(b) and 3.7(c)).

Since the geometry is practically identical to the one shown in Figure 3.7(a), it is the iso-dip contour that is shown in Figure 3.8(a). The 10° and 12° slab dip contours which bound the 11° critical dip according to the "Critical Taper Theory" of Davis et al. [1983] show a clear triangular wedge that extends inland in the Olympic Peninsula region, mimicking the distribution of the Crescent basalt backstop and the locus of the thick accretionary wedge material. Figure 3.9(a) shows the perspective view of the resulting optimal slab geometry with the slab seismicity; 3.9(b) is the same contour plot of the slab structure as in Figures 3.7(a), and is reproduced here to be compared with the regional trend of the volcanic line (Figure 3.8(c)) [Dickenson, 1970].

The result of these non-linear optimizations (both of experiments *Shallow-Dip I*

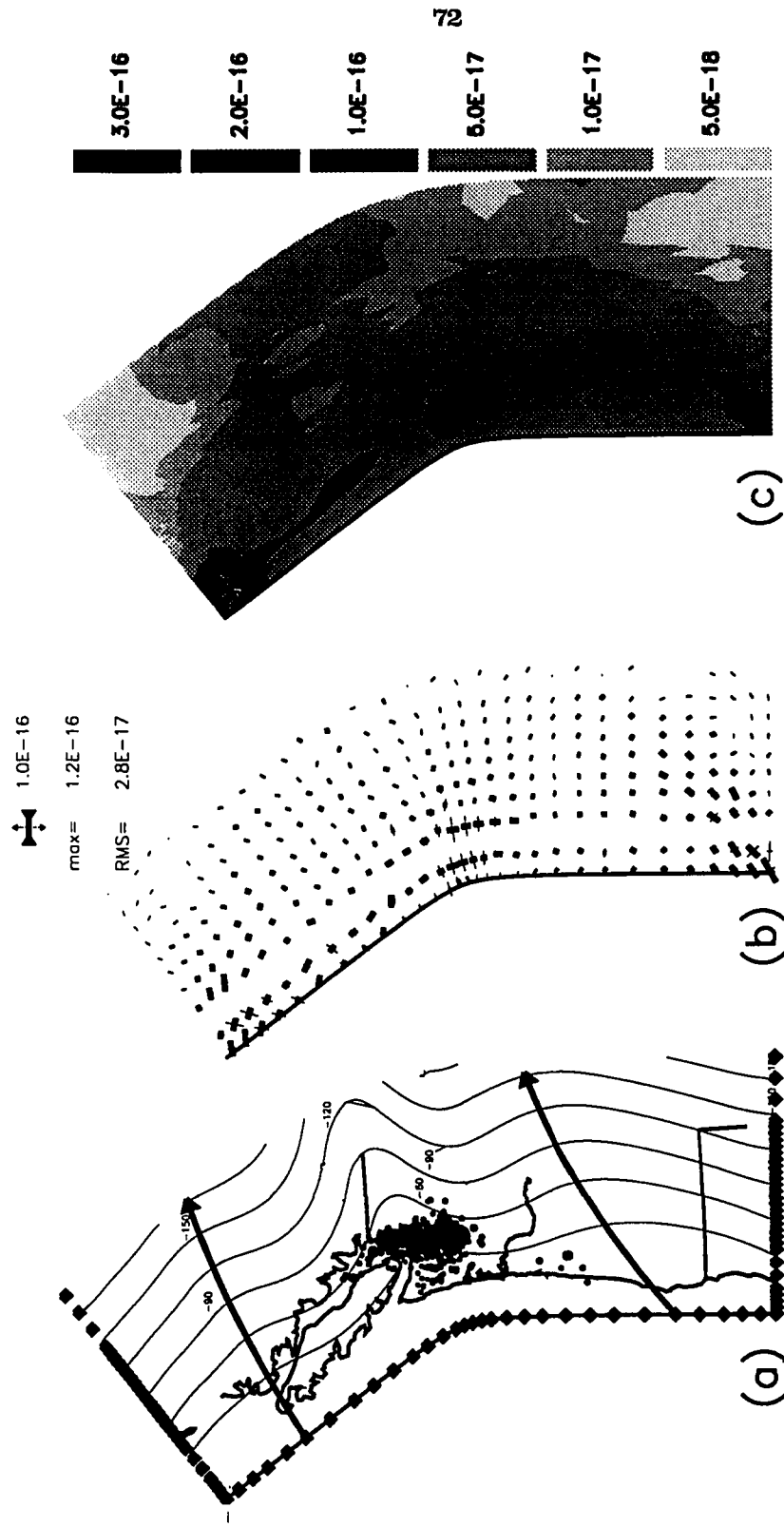


Figure 3.7 The *Shallow-Dip 1* experiment full inversion involving both the flow field and the slab geometry for shallower structure and deformation regime of Cascadia Subduction Zone, experiment on examining the effects of the concave-oceanward shape of the trench in this subduction zone, Newtonian rheology. Notice that boundary conditions on the slab geometry are marked by filled squares on the edges in (a). (Also refer to the caption of Figure 2.9 for explanations of the plots in (b) and (c))

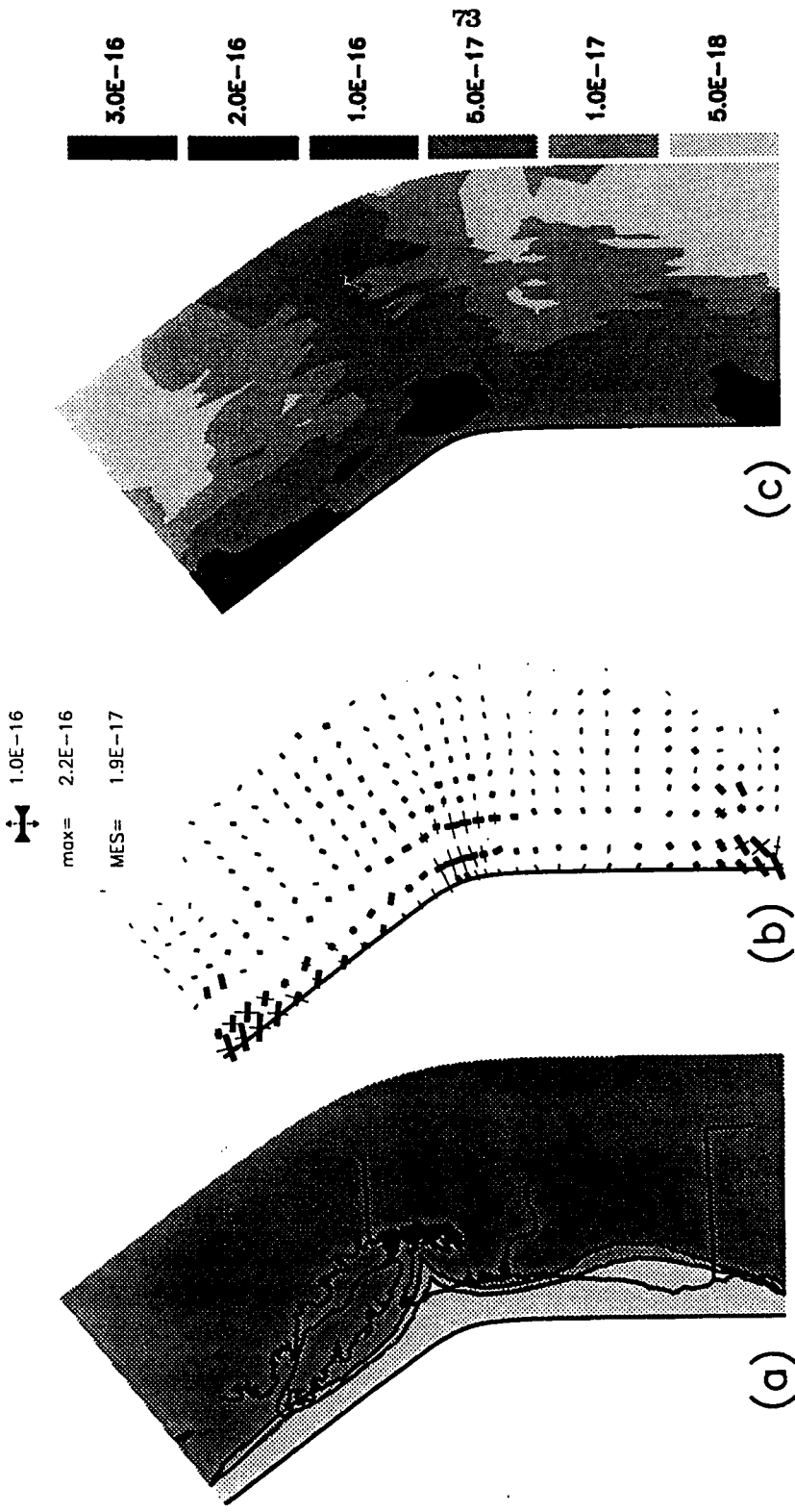


Figure 3.8 The *Shallow-Dip II* experiment, Power-Law rheology ($n=10^6$) instead of Newtonian rheology. (a) shows the 10^0 and 120° iso-dip contour of the slab dip, the triangular wedge in the Olympic Peninsula region produced by the arch structure provides room for the thick accretionary prism to develop, which is consistent with the "Critical Taper Model" by Davis et al. (1983). (Refer to the caption of Figure 2.9 for explanations of the plots in (b) and (c))

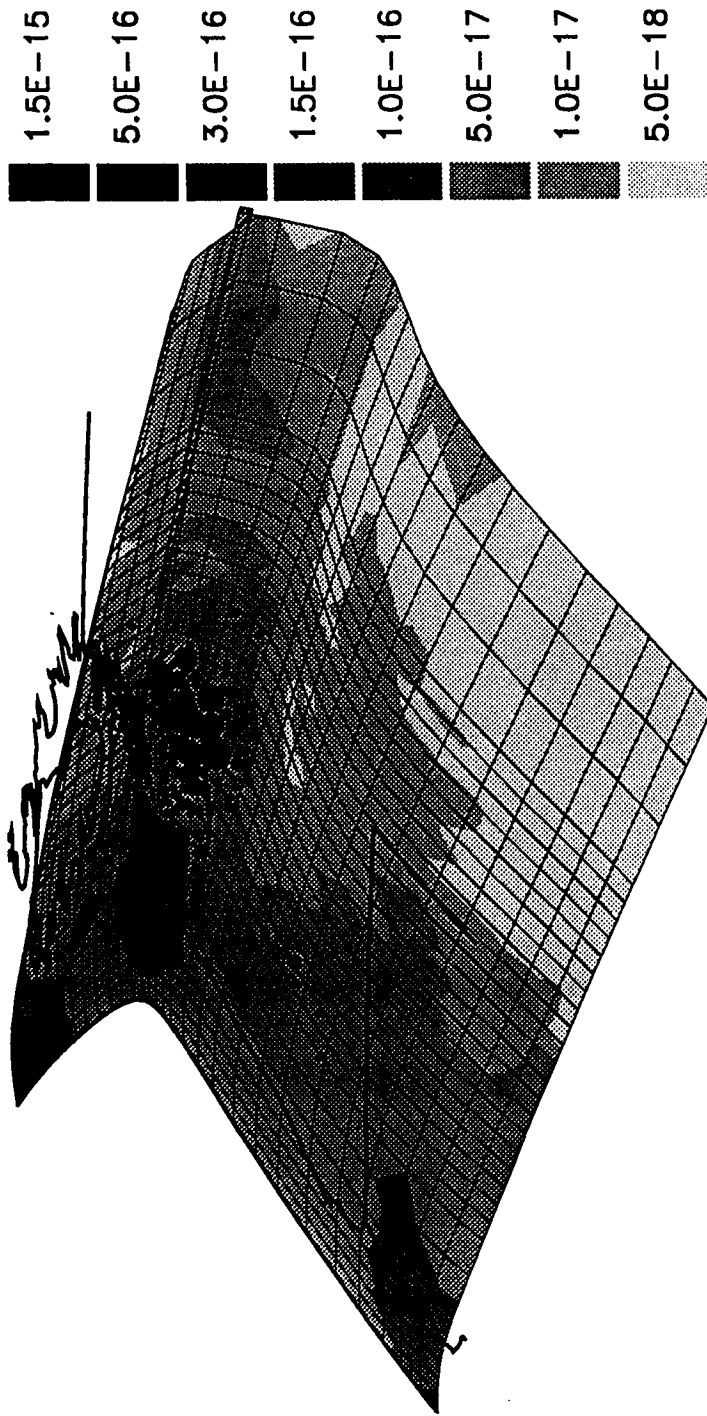


Figure 3.9 (a) Perspective view of the shallow structure of the Cascadia slab outlined by the mesh surface. Same seismicity as in Figure 3.2(a), except projected differently. The gray-scale pattern is the same distribution of effective strain rates as in Figure 3.8(c). Compare (b) the structure projected to the surface, and (c) the regional volcanic trend [from Dickenson, 1970].

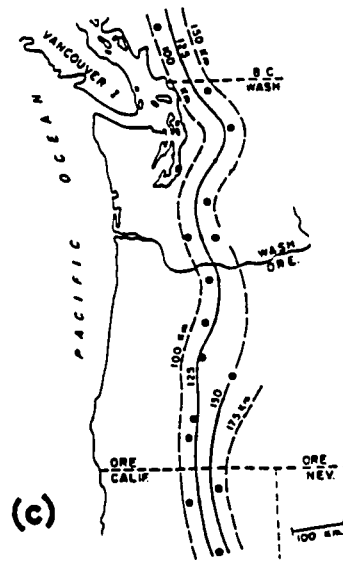
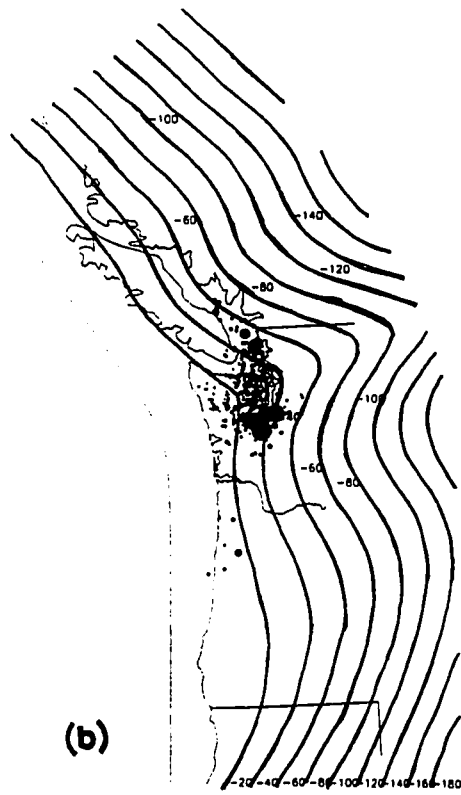


Figure 3.9 (Continued)

and *Shallow-Dip II*) provide a plausible model for the underlying shallow structure of Cascadia Slab that is consistent with the observations mentioned earlier in this chapter.

The total seismic moment release can be viewed as a reflection of the undergoing deformation. Bevis [1988] derived a simple formula to relate the seismic moment release and the average strain rate for intra-slab earthquakes,

$$\dot{\epsilon} = \frac{\Sigma M}{2\mu WLHt}$$

where $\dot{\epsilon}$ is the average effective strain rate, μ is the rigidity of the slab,

M is the total seismic moment release in a time period t ,

W, L, H are along-strike width, down-dip length, slab thickness.

Assuming $\mu = 7 \times 10^{11}$ dyn / cm², $W = 200$ km, $L = 200$ km, $H = 10$ km, $t = 90$ years for the Cascadia slab, we get a strain-rate of 2×10^{-16} sec⁻¹. Note that over 99% of the summed moment release comes from the 5 events in Table 1. The predicted peak membrane strain-rate is about 1.5×10^{-16} sec⁻¹, which is the same order of magnitude as calculated from seismic moment releases. We also estimated the mean bending strain rate to be also around $\dot{\epsilon}_{\text{bending}} = 2 \times 10^{-16}$ sec⁻¹ based on simple profile shown in Figure 3.5c and the simple formula described in Section 2.3.3 i.e., $\frac{V(d\kappa/ds)H}{4}$, where $d\kappa/ds$ is the change of curvature along the path, H is the seismogenic thickness of the slab and v is the convergence rate. The membrane strain rate and the bending strain rate are thus the same order of magnitude comparable to scalar strain rate estimated from seismic activity.

The modelling results, however, do not provide adequate explanations for two observations:

- (1). The predicted deformation-rate contrast comparing the peak value with the background is only within one order of magnitude while the seismic moment contrast is at least 3 orders of magnitude. The Power-law rheology improves this but still does not have the right order of magnitude.
- (2). This model did not take account of the evidence from tomographic studies which suggests that the slab goes to a steeper 55° dip at greater depth.

3.3 Effect of bending an arch: The *Arch-Bending* experiment

Our first hypothesis, examined in the previous section, is that the abnormal bend of the trench forces the occurrence of the arch in order to accommodate the room problem [Rogers, 1984] it creates. However, the slab has to go to a steeper dip at greater depth as indicated by tomographic studies [Rasmussen and Humphrey, 1988; Vandecar, 1991]. As a result, we are faced with a situation of bending an arch. This will be very difficult compared to bending a flat sheet. We designed the second experiment with relatively simple geometry to test our second working hypothesis that the concentration of slab seismicity in the Puget-Sound area is caused by concentration of in-plane deformation when the arch is bent to go to steeper dip.

For this *Arch-Bending* experiment, a simple arch is built in a rectangular region with normalized length 200 km by 200 km as shown in Figure 3.10(b), on the left edge the surface is relatively flat to the north and to the south. In the middle, a Gaussian-shaped arch with the peak height 40 km is superposed on the flat surface; this non-planar surface is then bent along a north-south axis in the middle. A flow field with constant speed within the surface and directed normal to the left entering edge is then imposed on this surface. Fixing the model geometry and the flow boundary conditions on the left edge, a flow field inversion is done by letting only the flow field adjust itself to achieve the minimum-membrane-deformation-rate configuration (Figure 3.10(a), (b)). Notice the widely-spread high membrane deformation before the bending occurs. If, on the other hand, we allow the geometry to be adjusted except on the north and south edges while holding the flow field fixed (Figure 3.10(c)-(f)). The result of the inversion shows a gradual reduction of total membrane deformation while concentrating the high deformation in the area near the arch axis and just before the bend starts to take place. After 30 iterations, the arch in down-dip direction is essentially removed. Results for the full inversion are shown in Figure 3.10(g)-(j) by letting both the flow field and the geometry be adjusted simultaneously. While the boundary conditions on the flow field are the same (the velocity vectors on the left edge are fixed) the boundary conditions on the geometry are slightly different: for (g),(h), the two cross sections defining the northern and southern edge are completely fixed as before; while in (i),(j) only the depth at the two points in the upper right and lower right corners are fixed. Not surprisingly,

(i),(j) yield the lowest membrane deformation rate. The results of both (g),(h) and (i),(j) show an interesting effect that while both the geometry and the flow field are allowed to be adjusted, it does not require the arch to be flattened out after the bend to get to a lower deformation configuration as compared to the result shown in (e),(f) where it does require the arch to be wiped out since in that experiment, only the geometry is allowed to be adjusted. The overall pattern of the optimal deformation rate distribution are generally the same. In the down dip side, there is practically no significant deformation; within the bending zone, the deformation is low near the axis of the arch; before the bending area, the deformation is concentrated around the arch especially right before encountering the bend. We suspect that the concentration of seismicity underneath Puget-Sound area is the result of an analogous deformation pattern.

3.4 Incorporating the information of a steeper secondary bend: The *Steep-Dip* experiment

Combining the essence of experiments described in 3.2 and 3.3, we use the arch structure from the experiment shown by Figure 3.2 as the initial model for a new inversion where the geometric boundary conditions on the northern and southern edges are forced to dive to a steeper 55° dip. The results of this *Steep-Dip* experiment that includes the complete inversion of tuning both the flow field and the slab geometry in order to reduce the membrane deformation rate are shown in Figure 3.11. The slab geometry goes to a simpler configuration (Figure 3.11(a)) with an even tighter arch structure at greater depth. The deformation near the arch axis is much higher and more concentrated (Figure 3.11 (b) and (c)) than in the *Shallow-Dip I* experiment (Figure 3.7).

To test the uniqueness of our solution, we repeat the experiment with identical boundary conditions, but a different starting model. Cross-sections for the new starting model do not vary along strike. The result of this inversion converges to a solution that is essentially identical to what is shown in Figure 3.11 implying that the predicted arch is a robust result forced by the shape of the trench instead of being caused by the seed arch in the initial model. Note that the 55° dip in this *Steep-Dip* experiment forces strain rates about 3 times greater than the shallower-dip (20°) models.

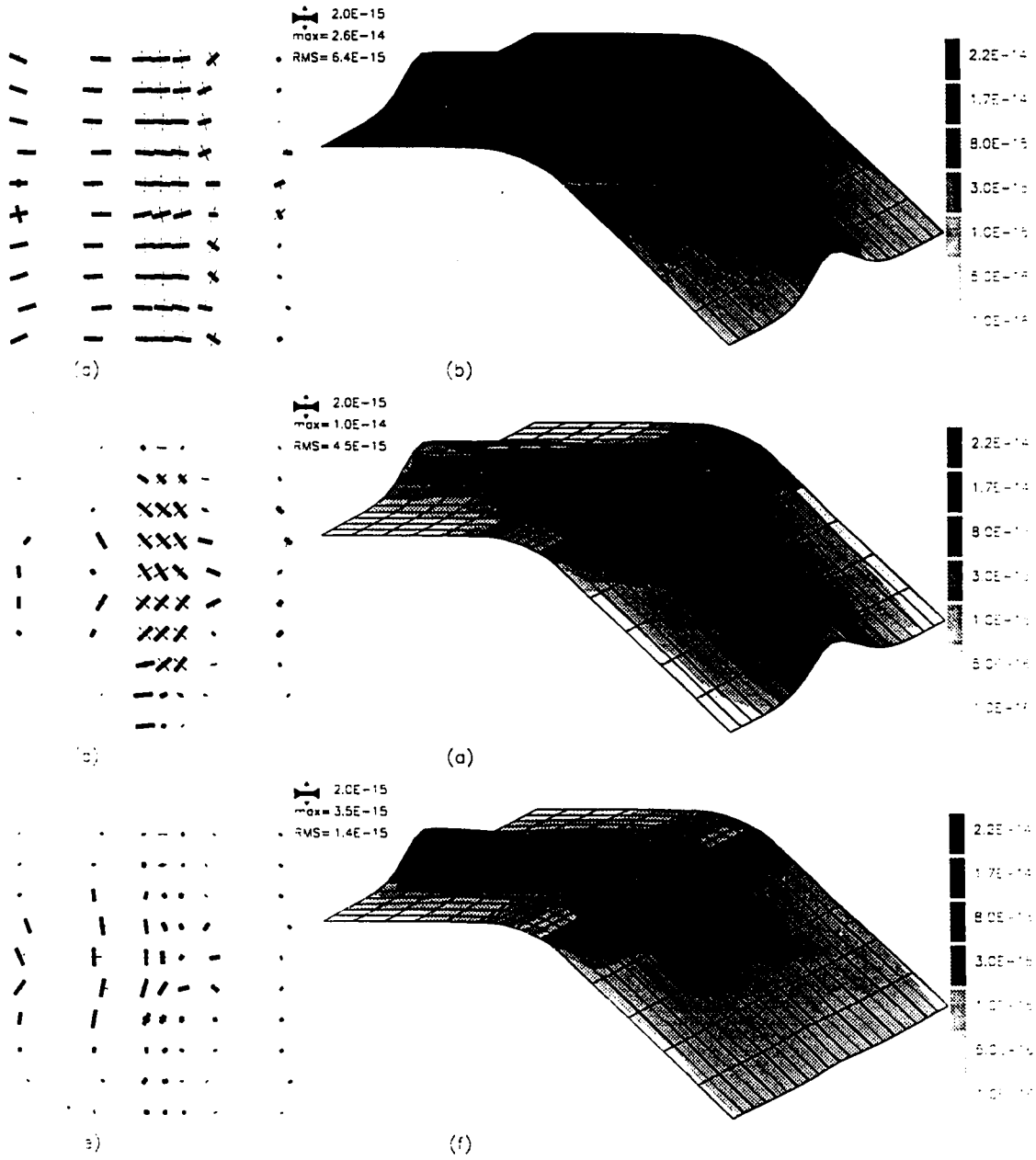


Figure 3.10 (see next page)

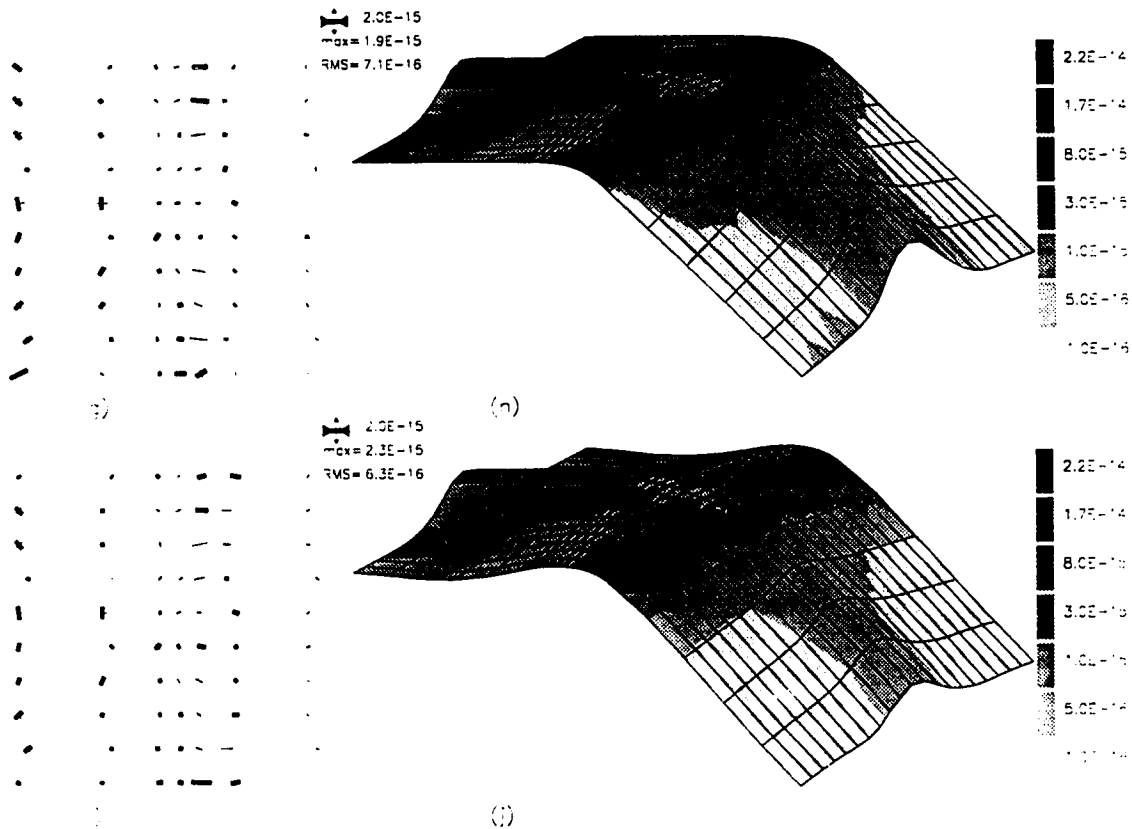


Figure 3.10 The *Arch-bending* experiment on the effects of bending an already arched, non-flat surface. (a), (b) are orientations of principle axes of the membrane strain rates and the distribution of the effective strain rate (see the caption of Figure 2.9) for the optimization by inverting for flow field only. (c)-(f) are results of inverting for optimal geometry only (holding the flow field fixed) using (a),(b) as the initial model. (c), (d) are the same plots after 15 iterations for the complete nonlinear optimization involving both the flow field and the model geometry; (e), (f) are after 30 iterations. (g)-(j) are plots for similar optimization as in (c)-(f) except that both the flow field and the geometry are allowed to be tuned, also, the boundary conditions on the geometry are more relaxed. Instead of fixing the entire northern and southern edges, (g),(h) allow the three points sitting in the bending zone to be free to adjust while (i),(j) only fix the two corner points in the upper- and lower right.

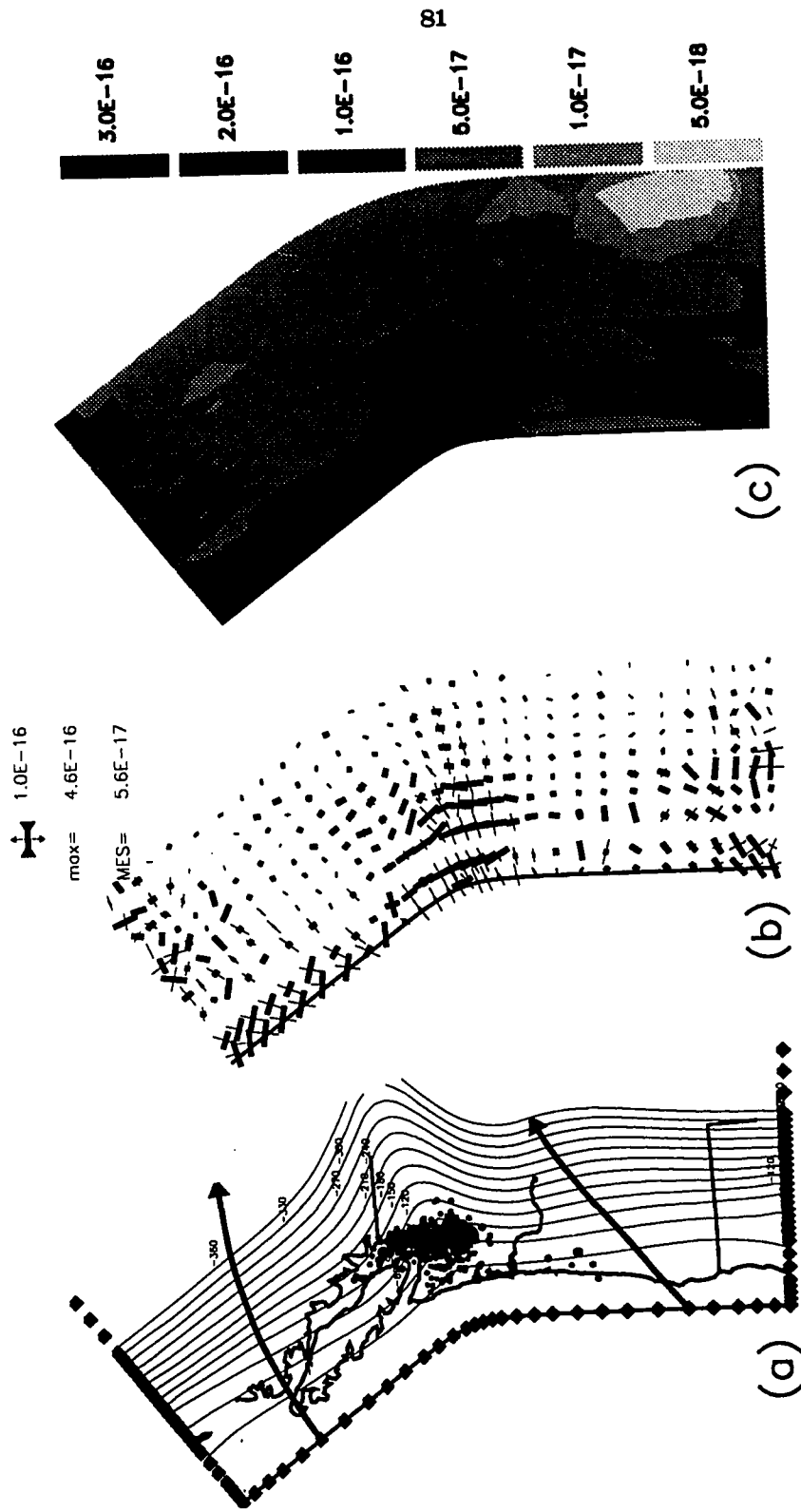


Figure 3.11 The *Steep-Dip* experiment, full inversion incorporating the steeper 55° dip in greater depths, showing the effects of combining the concave-oceanward shape of the trench and a steep secondary bend. (a) Depth contours showing the resulting slab structure, (b) Orientations of principal axes of the membrane strain rates, (c) the distribution of effective strain rates (Refer to the caption of Figure 2.9 for explanations of the plots in (b) and (c)).

3.5 Conclusions and discussions

The experiments described in section 3.2, 3.3 and 3.4 leads us to the following conclusions:

- (a). The arch structure of the subducted Cascadia Slab underlying Olympic Mountains and the Puget-Sound basin is a natural response of the subducted slab trying to accommodate the room problem as the spherical oceanic lithosphere subducts at a trench with a backward-curved shape.
- (b). Strain rate estimated from the seismic moment release calculated for the slab earthquakes of the last century are about the same order of magnitude as the calculated membrane and bending strain rates.
- (c). As the arch forms, the shallower slab dip on top of the arch provides a better opportunity to form a thicker accretionary prism. Consistent with the Critical Taper theory, the iso-dip contours of our predicted arch provides a reasonable explanation for the origin of the Olympic mountains and the the reason why it is laterally confined narrowly near the axis of the concave-oceanward bend of the trench in the along-arc direction. The shape of the circumferential backstop (the Crescent formation) seems to be consistent with the tightness of the predicted arch. Although the predicted arch seems to have an even shallower dip as compared with the dip revealed from slab seismicity, the tightness of the arch structure is consistent with the P-to-S receiver function analysis. Also, undulations in the trend of the volcanic line are consistent with the predicted slab structure.
- (d). By subducting to a steeper dip at greater depth (>100 km), the already formed arch has to be bent, this might cause the concentration of the seismicity underneath the Puget-Sound area. The predicted concentration as shown in Figure 3.11c, however, is not as dramatic as revealed from seismic moment release shown in Figure 3.3. There are two possible explanations for this, one is that the one hundred year sampling window used to construct Figure 3.3 is too short, in other words, there might have been big historical events outside the Puget-Sound area.

The other plausible explanation is that the seismic activity becomes significant only when the local deformation rate is higher than certain threshold level. Also, the increased crustal seismicity near Puget Sound that is over the predicted arch may also be related to the arch structure. One speculation is that whereas the 20° dip north and south of the arch may be in local dynamic equilibrium, the arch geometry may not be in local dynamic equilibrium, producing large shear stresses in the crust above the arch.

- (e). The experiments incorporating the steeper 55° dip as boundary conditions predicts an even more pronounced arch. However, tomographic results [Vandecar, 1991] do not indicate a noticeable shallower slab dip at depths exceeding 100 km underneath the Puget-Sound region compared to areas further north and south. This points out one serious defect in our formulation. We did not include important dynamic controls such as gravitational pulling. In other words, our formulation let the slab surface change its configuration in order to seek the geometry that reduces membrane deformation. In the case of this subduction zone, forming an arch is an efficient way to achieve this reduction. However, forming the arch is against the effect of gravity. Adding the effect of the gravitational pulling might balance part of the tendency of forming an arch, and in return would increase the deformation within the slab underneath the Puget Sound area.
- (f). From his tomographic study of Cascadia Slab, Vandecar [1991] suggest that the slab is torn at a depth near 100 km beneath Oregon. If this is the case, the need to form a pronounced arch at greater depth in order to reduce the membrane deformation as predicted in our steep-dip experiment will be relaxed. Our calculation is performed with respect to the current configuration of the trench, and based on the assumption that the slab is continuous across the entire subduction zone. The question of whether the tear is present or not is not directly resolvable by our calculation.

Chapter 4 Preliminary experiments on Alaska-Aleutian and NW-Pacific

4.1 Alaska-Aleutian Subduction Zone

4.1.1 Slab seismicity, slab geometry and focal mechanisms

Figure 4.1 is reproduced from Kienl et al. [1983] which shows the seismicity and the tectonic framework of Alaska-Aleutian Subduction Zone. The relative plate motion between Pacific and North American plate [Minster and Jordan, 1978] is nearly normal to the trench in the eastern Aleutians but almost parallel to the plate boundary in both southeastern Alaska and the western Aleutians. We plot the map view distribution of the seismic moment release (Figure 4.2(a)) computed for earthquakes below 70 km from ISC bulletins (1964-1984), and from large historical slab earthquakes in this century from Astiz et. al. [1988]. We also plot the same seismic moment release projected to a cylindrical surface roughly parallel to the along-arc direction (Figure 4.2(b)). The most immediate impression indicated by these plots is that there are two zones where seismic activity seems to concentrate. One is around the Gulf of Alaska where the trench has a concave-oceanward shape and the other is in the central Aleutians where the trench seems to have the tightest curvature. The Aleutian slab geometry is relatively well constrained by Wadati-Benioff seismicity. The decrease of maximum depth of seismicity from 250 km in the central Aleutians to 50 km toward the west is explained by Creager and Boyd [1991] to be caused by along-arc variation of the slab's thermal structure. Seismicity rate is reduced in the southeastern Alaska region. However, by combining locally recorded events and evidence from seismic reflection profiling, Page et al. [1989] mapped the shallower structure of the Wrangell zone. This zone extends to a depth of at least 100 km beneath Wrangell volcanos and at least 150 km in lateral extension (Figure 1.5d). The local strike direction at the eastern edge of the Aleutian Wadati-Benioff zone is 90° from the strike of the Wrangell zone, and the region between the two zones is totally aseismic down to the detection level of the local array [Figure 1.5d, and Page et al., 1989]. They favor a continuous buckled slab structure, at least in the shallower depth, rather than putting a tear to separate these two zones. Note that the aseismic zone

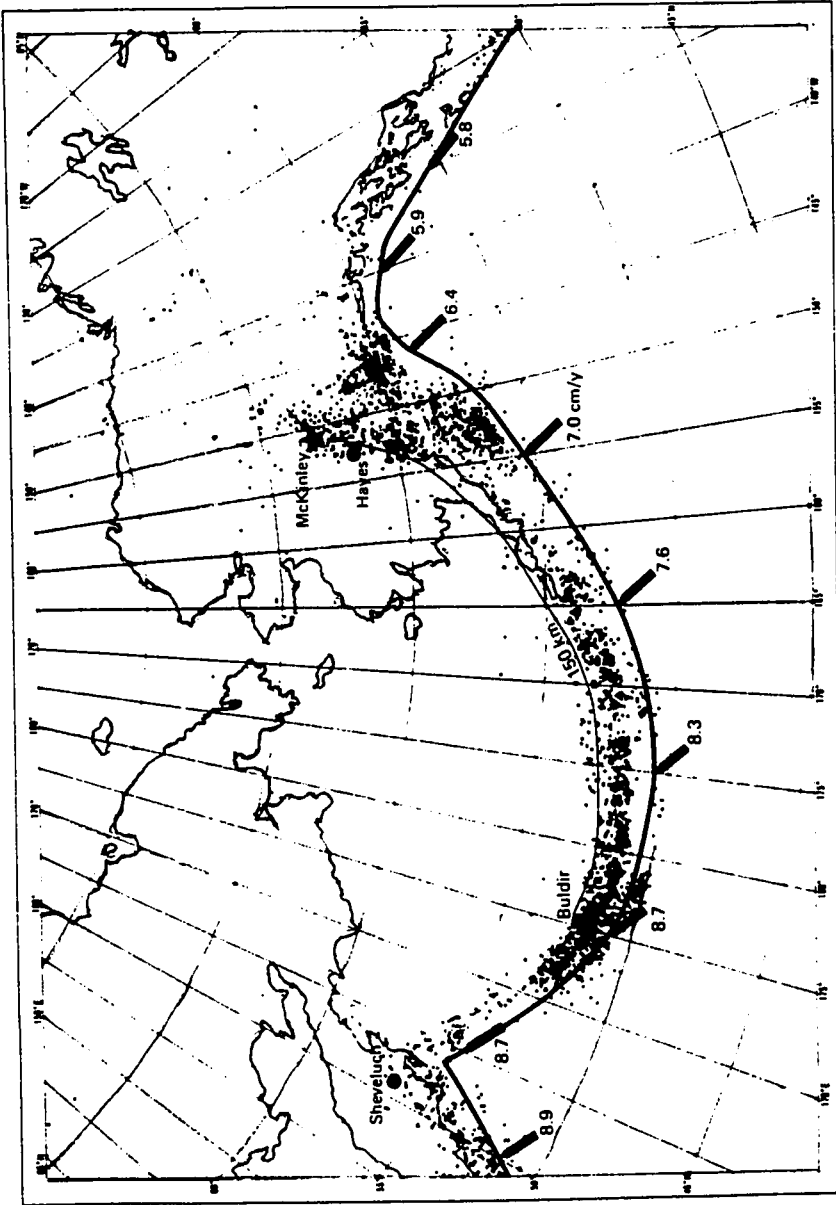


Figure 4.1 Seismicity and the tectonic framework of the Alaska-Aleutian Subduction Zone. (reproduced from Kienl et al., 1983).

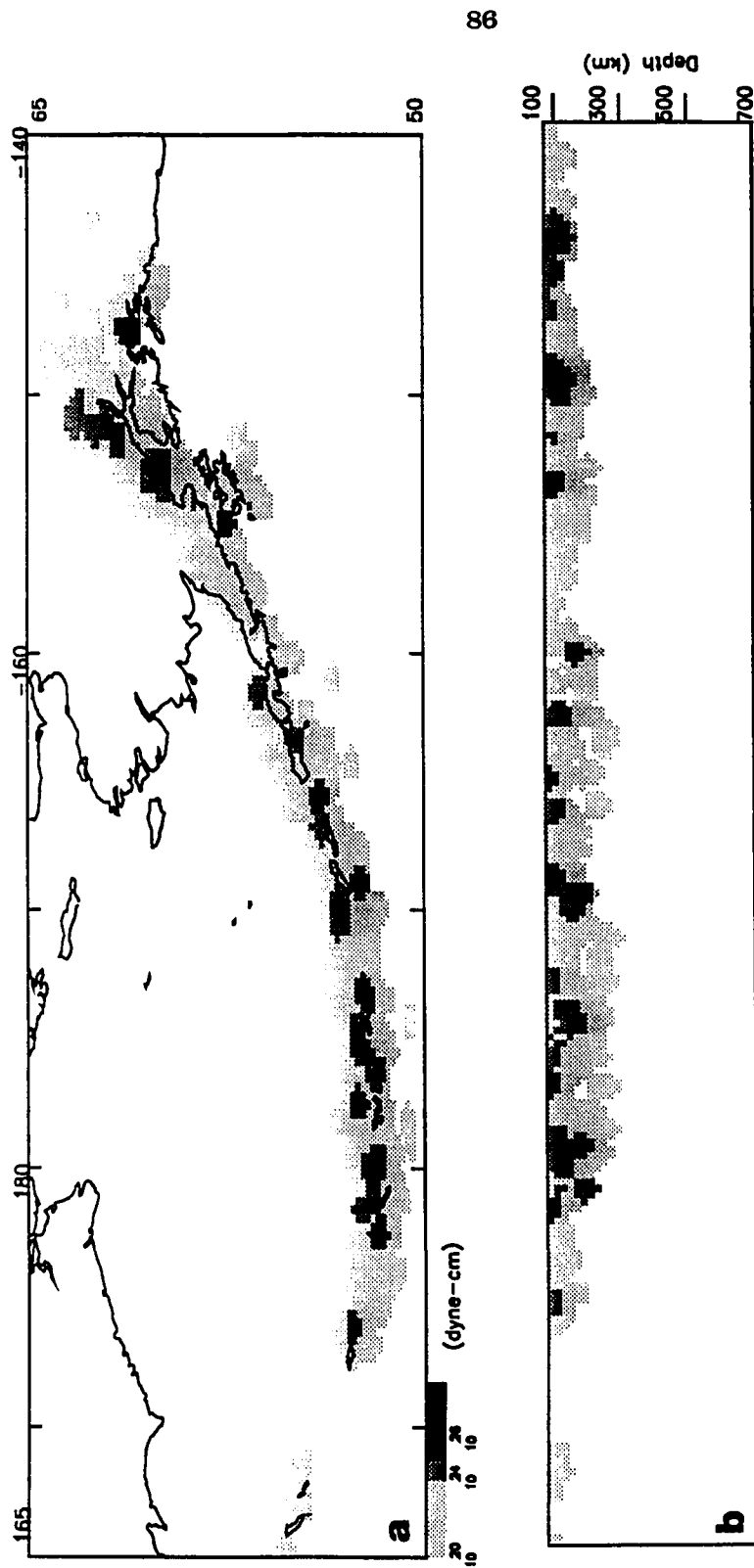


Figure 4.2 Seismic moment release of Alaska-Aleutian Subduction Zone., the region is divided into 40 km by 40 km cells, all the earthquakes deeper than 70 km from ISC (1964-1984) and from the catalog of large earthquakes of this century [Astiz et al., 1988] that fall in the same cell are converted to seismic moment (see Equation 3.1) and summed. Notice that the gray-scale key at the bottom indicates that we have grouped the moment release into three different levels (above 10^{20} , 10^{24} , 10^{25}) for easy detection of patterns, the peak value is on the order of 10^{28} dyne-cm. (a). Map view. (b) Projected to a cylindrical surface roughly parallel to the along-arc direction.

is landward of a sharp concave oceanward bend in the trench. Pulpan and Frohlich [1985] point out that the Aleutian slab's strike changes by 15° beneath the lower Cook Inlet that is coincident with a northward bend of the volcanic line (see Figure 1.5d). They also point out an increase of seismic activity near this bend area.

The along-arc tensional character of intermediate-focus events in the central Aleutians was recognized more than two decades ago [Stauder, 1968; Isacks and Molnar, 1971] and later confirmed by Creager and Boyd [1991] (see Figures 1.7 and 4.4). In the Eastern Aleutian-Alaska region, Pulpan and Frohlich [1985] argue for two possible segment boundaries near the Cook Inlet area and that the focal mechanisms at intermediate depth beneath Cook Inlet are controlled by horizontal north-south compression. Kissling and Lahr [1991] also show that focal mechanisms at Southern Alaska around the same region are dominated by down-dip extension and along-arc compression. The pattern of along-arc extension in the central Aleutians and along-arc compression in the eastern Aleutians is confirmed by the CMT solutions (figure 4.5b).

4.1.2 Previous models

Yamaoka et al. [1986], using their analog fitting experiment described in chapter 1, claim that they were able to get reasonably good fit which does not require any tears in this slab geometry, although the 45° slab dip angle for their slab geometry is probably not steep enough in the central Aleutians as pointed out by Creager and Boyd [1991]. Burbach and Frohlich's [1986] modeling results in Aleutian Zone are summarized in Figure 4.3 where they indicate five Possible Segment Boundaries (PSBs) and show that the whole Aleutian Zone is under lateral extension averaging to 10% accumulated strain after 10 million years of subduction with a peak value of 50% accumulated strain in the western Aleutians. They do not predict along-arc compression under Alaska because they do not extend their calculation to where the trench curvature changes to concave oceanward. Creager and Boyd [1991] concentrate their efforts in the Aleutian zone between longitudes 165°E and 160°W . They construct the slab geometry constrained by

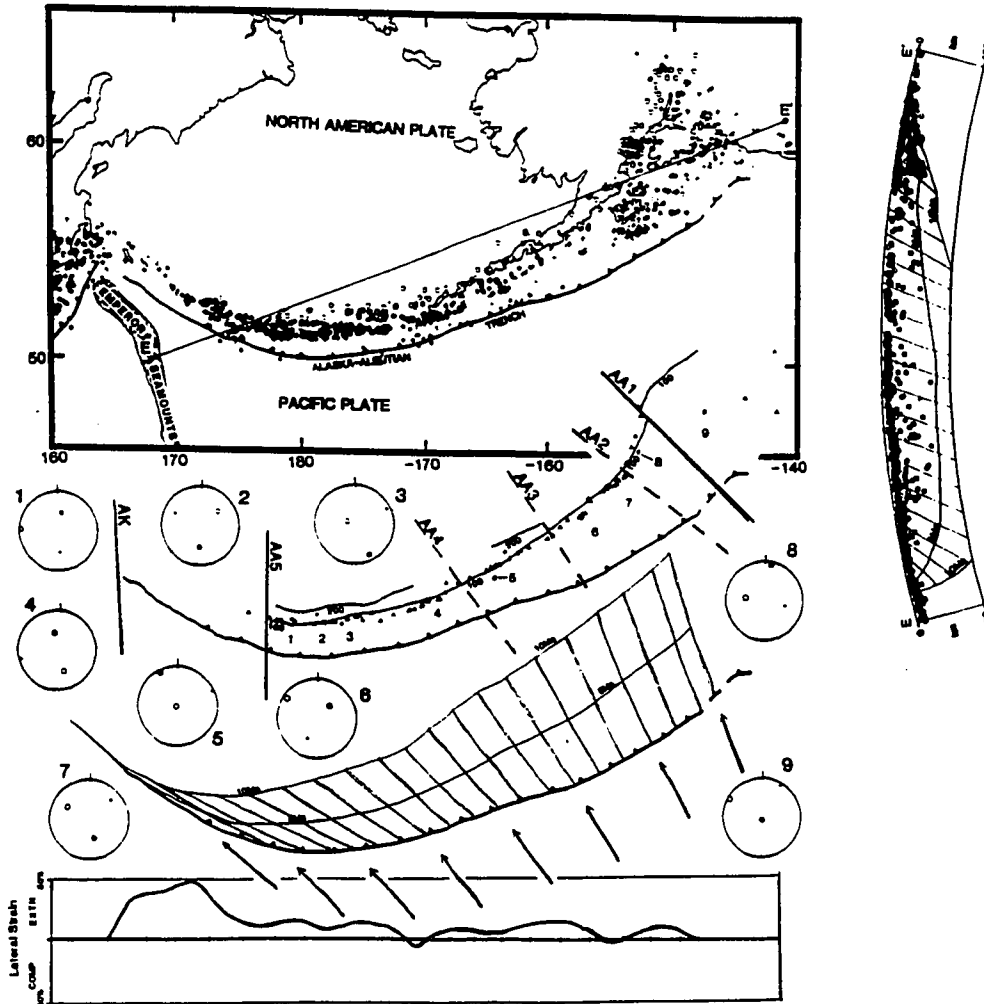


Figure 4.3 Burbach and Frohlich's [1986] modelling results of Alaska-Aleutian Subduction Zone. AA1-AA5 show the locations of the five possible segment boundaries (PSBs). On the same drawing, numbered positions from 1 to 9 are the CMT mechanism locations. The numbered CMT mechanisms are lower-hemisphere projections with solid circles for P-axes, open circles for T-axes and crosses for N-axes. Below that, the grids show the 5 my and 10 my isochrons of subduction while the set of lines in the direction of arrows are the tracked particle paths. The Lateral strain plot shows the accumulated lateral strain after 10 my of subduction. The slab is shown in general in along-arc extension, with a peak of 50% accumulated strain after 10 my of subduction in the Western Aleutian.

local network data where the slab is seismically active, and P-wave residual-sphere analysis of eleven earthquakes and one nuclear explosion where the slab is aseismic. The slab dip angle below 100 km depth varies from 45° in the eastern Aleutians to 60° in the central Aleutians and then to $\sim 50^{\circ}$ in the western Aleutian. Fixing this slab geometry, they invert for the optimal flow field that minimizes the in-plane deformation. Shown in Figure 4.3, their result predicts along-arc extension dominating the in-plane strain rate field with a peak value of $10^{-15} \text{ sec}^{-1}$ in the central Aleutians, and an accumulation of 10% strain as the slab material reaches the seismicity cutoff. The along-arc variations in the magnitude and orientation of their calculated strain-rates are in general consistent with the spatial distribution of seismic moment release and source mechanisms of intermediate-depth earthquakes (Figure 4.4). Also, their optimal flow field suggests that the slab underneath the far western Aleutians was transported there laterally with nearly zero component of down-dip subduction. They argue that this might be responsible for the lack of volcanic activity in that region.

4.1.3 Modeling efforts in this study

The basic goals in undertaking preliminary modeling experiments in this subduction zone are to test our working hypothesis that membrane deformation optimization provides reasonable explanations for the basic slab geometry and the pattern of seismic activity; especially the along-arc extension in the central Aleutian zone, along-arc compression in the eastern Aleutian zone and the arch structure implied by the variation of slab geometry around the corner surrounding the Gulf of Alaska.

4.1.3a The *Constant-dip* and *Continuous-slab* experiments

We begin by digitizing the Alaska-Aleutian trench and perform the first experiment on a *Constant-Dip* model. By utilizing the mesh construction technique described in Appendix C, we construct a mesh with 2142 triangles wrapping around the curve representing the trench. This *Constant-Dip* experiment uses a cross section that is built by letting the slab attain a 45° dip using the "minimum change of curvature" interpolation described in chapter 2. We then invert for the flow field only. Results of this experiment are shown in Figure 4.5. Principal axes of membrane strain-rates show a

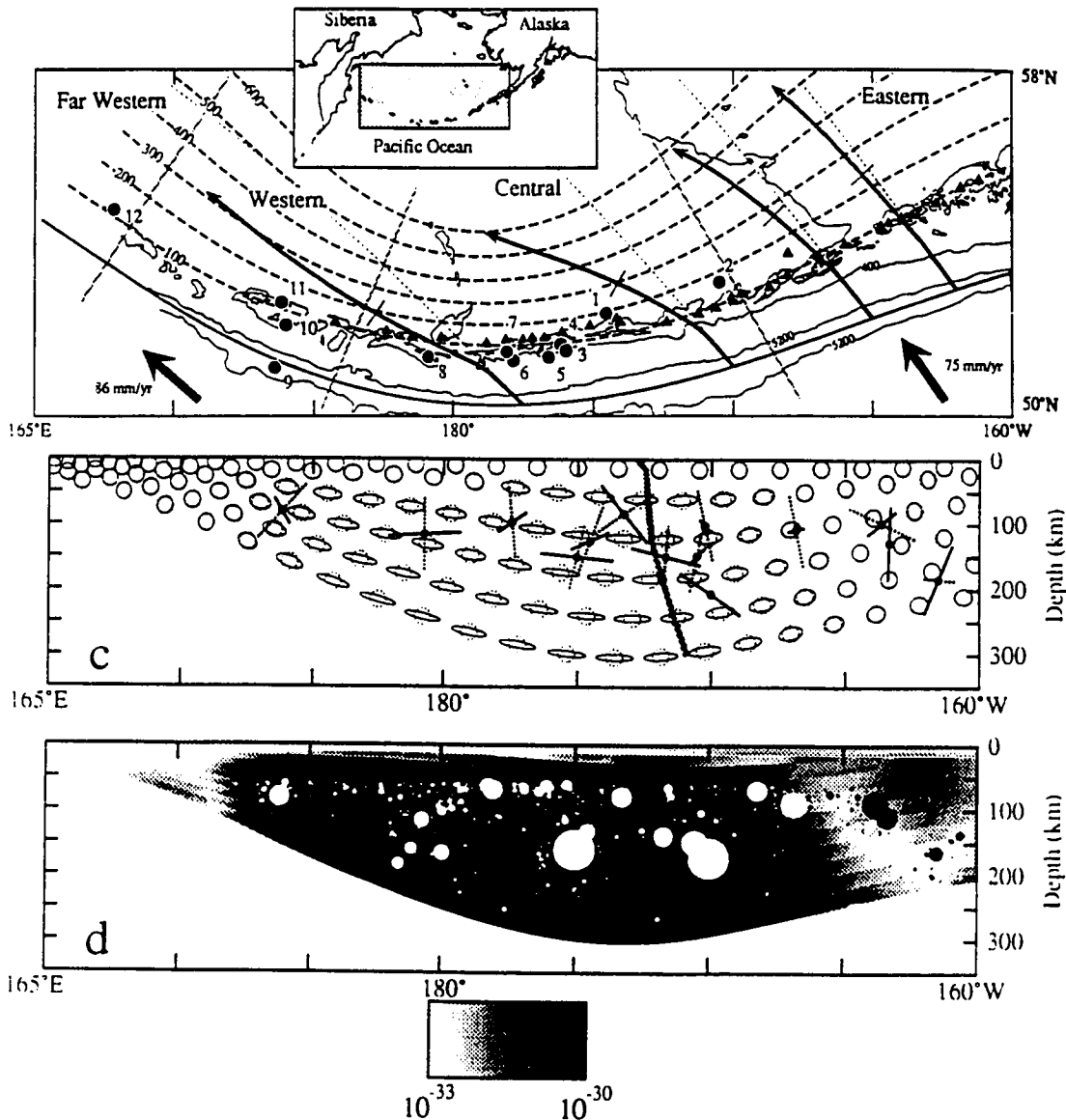


Figure 4.4 Creager and Boyd's [1991] modelling results of the Aleutian slab. (a) The slab geometry and the particle path representing the optimal flow field (inverted for the flow field that minimizes the in-plane deformation by holding the slab geometry fixed). (b) The comparison between the strain-rate ellipses, with long axes in extension and short axes in compression, and the focal mechanisms, with solid lines for extension axes and dotted lines for compression, projected on the Longitude versus depth cross section. (c) The distribution of the effective strain-rate ranging from 3×10^{-17} (light grey) to $10^{-15} \text{ sec}^{-1}$ (black), and circles whose radii are proportional to the earthquake magnitudes.

very simple systematic pattern with the central Aleutians being under along-arc extension. The Gulf of Alaska area is under along-arc compression around the axis of the oceanward-concave trench. The fourteen available CMT mechanisms from 1/1977 to 6/1986 below a depth of 70 km are also plotted for comparison. The projection in Figure 4.5(b) is done by converting into a three-dimensional Cartesian coordinate and then projected on the surface ($z=0$), so that they are directly comparable to the model calculation, while in Figure 1.7, everything is projected on the surface of the earth and plotted in the Longitude-Latitude domain. Unlike the conclusion drawn by Burbach and Frohlich [1986], the pattern of these CMT solutions seem to fall into two groups, with four mechanisms in the central Aleutians having more or less along-arc extension and nine mechanisms around the Cook Inlet area having NE-SW compressional axes. This pattern is then basically consistent with the predicted deformation regime.

In a second experiment (the *Continuous-slab* experiment), we use the resulting flow field and the slab geometry from the previous *Constant-Dip* experiment as the starting model. We then fix the model geometry at the trench and only one point at the bottom edge in central Aleutians (marked by filled squares in Figure 4.6(a)). That is to say that the only constraint on the slab leaving the trench is that it has to go to a deep depth at that point, other than that, the slab is free to adjust itself both through modifying the in-plane flow field and by tuning the slab geometry. The slab geometry (Figure 4.6(a)) has the steepest dip in the central Aleutians. Away from there, both of the two flanks are trying to get to shallower dip angle, especially the eastern flank where the arch, forced by the oceanward-concave trench configuration, has a shallow dip. The pattern of along-arc extension in the central Aleutians and along-arc compression further east under Alaska remains. The predicted strain rate under the Wrangell mountains is greatly reduced, consistent with observations (compare Figure 4.6 to Figure 4.5). Orientations of compressive axes on the western wing switch to a more northeast direction. Effective strain-rates show a peak deformation rate of $7 \times 10^{-16} \text{ sec}^{-1}$ and with high deformation rates concentrated in between from western Alaska to the central Aleutians. This is in general consistent with the pattern of seismic activity. However, if we examine the seismic moment release plot in Figure 4.2 in more detail, the seismic activity within that zone is concentrated toward the two ends rather than in the middle as suggested by our model. The resulting geometry is in general consistent with observations from Wadati-

Benioff seismicity. Given that the boundary condition is only one fixed point at depth, the consistency between the predicted geometry and observations suggest that the optimization of membrane deformation rate is one important controlling factor for slab geometry. However, we notice that when the solution is approaching a minimum of the integrated dissipation power, while the geometry still changes in significant amount, the reduction in the integrated dissipation power can be extremely slow. This suggest that the "dissipation power" functional space defined in the subspace of geometry parameters is usually "flat" near the minimum.

The most robust features of these calculations are that a steep dip in the central Aleutians can only be achieved by a continuous slab if there is significant along-arc stretching. Secondly, the concave oceanward bend in the trench forces both an arch structure and along-arc compression wrapping around the arch. Note that the along-arc extension in the central Aleutians, along-arc compression in the eastern Aleutians/Alaska and the arch structure are all observed. We have tried several inversions similar to the *Continuous slab* experiment, but varying rheology, trench geometry and boundary conditions. In all calculations where geometry is allowed to vary, an instability develops as tight bends in the depth contours near the central Aleutians (Figure 4.6a). We do not completely understand this, but it is a region of intense along-arc shear deformation (Figure 4.6c), and suggests that if the slab can tear, this is where it would tear. Is it possible that the slab does in fact have a tear in that region (notice that the location coincides with the possible segment boundary AA4 in Burbach and Frohlich's study (Figure 4.3))? We simulate tear by considering two independent calculations, one for the Aleutians, one for Alaska. Each has a free edge where the tear is postulated to occur.

4.1.3b Alaska Zone: The *Alaska* experiment

In the *Alaska* experiment, we build a starting model with a constant 45° dip along the Wrangell-Alaska transition zone between 132°W to 160°W . Using this constant-dip configuration as initial model and fixing slab geometry along the trench and one profile at



Figure 4.5 The *Constant-Dip* experiment in Alaska-Aleutian Subduction Zone. (a) Depth contours showing the structure of the constant dip model, (b) CMT solutions deeper than 70 km(1/1977 - 7/1986) in this region are plotted by projecting their P-axes (most compressive axes, thick bars) and T-axes (least compressive axes, thin line segments) on the surface. (c) Orientations of principal axes of membrane strain rates, and (d) the distribution of the effective strain rate. Both (c) and (d) thus show the deformation regime for the model geometry computed (see caption of Figure 2.9 for general explanations) for the optimal flow field, i.e. the flow field obtained by holding the geometry of the slab surface fixed and invert for the flow field with the least amount of membrane deformation rate.

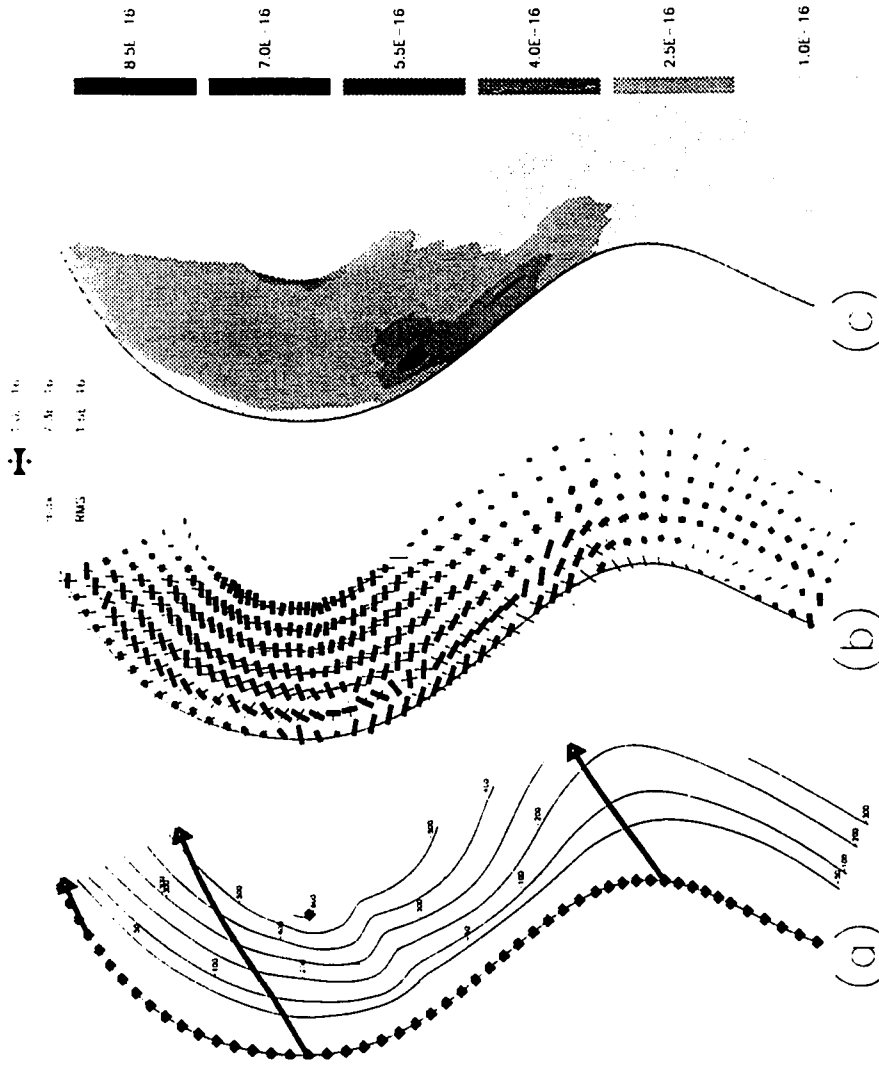


Figure 4.6 The *Continuous-slab* experiment in Alaska-Aleutian Subduction Zone. (a) Depth contours showing the geometry of the resulting structure, note that boundary conditions set on the slab geometry are marked by small filled squares, (b) orientations of principal axes of membrane strain rates, and (c) the distribution of the effective strain rate. Both (b) and (c) thus show the resulting deformation regime (see caption of Figure 2.9 for general explanations), i.e. the solution with the least amount of membrane deformation rate by performing full inversion on both the slab geometry and the flow field.

the eastern edge (marked by small filled squares in Figure 4.7a) we start the full iterative optimization. The reason to choose the one profile as a boundary condition is mainly because that profile is relatively well constrained by slab seismicity and that the slab geometry further west to Aleutian Zone is more or less uniform. The optimization result and comparisons with seismic observations are summarized in Figure 4.7. Comparing Figure 4.5 with Figure 4.7, a very efficient reduction in membrane deformation is achieved by forming a highly pronounced arch structure (notice that the grey-scales are different in Figures 4.5d and 4.7d). The deformation pattern revealed by CMT solutions (Figure 4.7b) is in general consistent with the orientation of predicted compressional axes (Figure 4.7c). Furthermore, Figure 4.7d shows that the deformation corresponding to Wrangell Zone is much lower to the eastern limb of the arch as compared to the western Aleutian Zone. The peak effective strain-rate is $2 \times 10^{-16} \text{ sec}^{-1}$ and concentrated around the Cook Inlet area where higher seismic activity is observed. Again, similar to the case in Cascadia Subduction Zone, the predicted arch structure is probably too severe because of the lack of involvement of gravitational pulling in our model calculations.

4.1.3c Aleutian Zone: The *Aleutian* experiment

A 60° constant-dip geometry is used as initial model for optimization experiment in the Aleutian Zone (165°E to 158°W). Figure 4.8a shows the intermediate-focus seismicity, the particle path and the optimal slab geometry. Figure 4.8b is the four CMT solutions below 70 km that show a deformation regime generally consistent with the calculated membrane deformation as shown in Figure 4.8c. Figure 4.8c reveals a clear pattern of along-arc extension in the central Aleutians and gradually switch to compression to shallower depth both to the east and to the west. The peak value of the membrane strain-rate in the central Aleutians is $2 \times 10^{-15} \text{ sec}^{-1}$ that is slightly higher than the result from Creager and Boyd's study. In general, the result of this experiment is qualitatively reproducing Creager and Boyd's result, however, instead of fixing the slab geometry a priori, our predicted slab geometry is not the same as theirs in the Eastern Aleutian, also the extremely high deformation to the eastern edge (Figure 4.8d) that appears in our modelling is not consistent with their study.

In conclusion, the four experiments presented here for Alaska-Aleutian subduction Zone indicate that:

- (1). Consistent with observations and previous modeling studies by Burbach & Frohlich, and Creager & Boyd, the subducting Aleutian Slab has a steeper dip in the central Aleutians than the western and eastern Aleutians. The slab dip is in general too steep for its trench configuration which leads to along-arc tensional membrane deformation rates. The backward curved trench around Gulf of Alaska, on the other hand, imposes along-arc compression. This along-arc compression can be reduced by forming an arch analogous to the situation in Cascadia Subduction Zone (Chapter 3). This pattern of along-arc extensions in the central Aleutians switching to along-arc compressions associated with the backward curved trench is a robust feature in all our experiment (some of them are not presented here). This pattern is also generally consistent with orientations of earthquakes focal mechanisms shown by the fourteen CMT solutions.
- (2). The resulting arch in Alaska-Wrangell slab reduces the along-arc compression, especially those in the eastern limb of the arch, that is, in the Wrangell Zone. While in the Cascadia subduction zone, the high deformation rates concentration coincides with the arch axis, the concentration of high deformation rates around Alaska-Wrangell Arch is skewed to the west, allowing very low deformation rates in Wrangell Zone. This result is true for all experiments we performed in this area (Figures 4.6 and 4.7), even when additional boundary conditions are put in by fixing the eastern edge (the bottom edge on Figures 4.6 and 4.7).
- (3). The *Continuous-Slab* experiment results in a shear contortion of the slab geometry. Associated with this contortion, all the experiments seem to concentrate their high deformation rates in the same area. This is not consistent with observation that the seismic activity concentrates more in the central Aleutians and around the arch. A tear within the subducted slab might account for this contradiction, however, it is not directly resolvable from our modelling.
- (4). The aseismic region between the Aleutian zone and Wrangell zone is an intriguing observation with no obvious explanation. Our calculation suggest that this region should be in along-arc compression, so if the slab were torn, it would be overlapping, not separating, in that region.

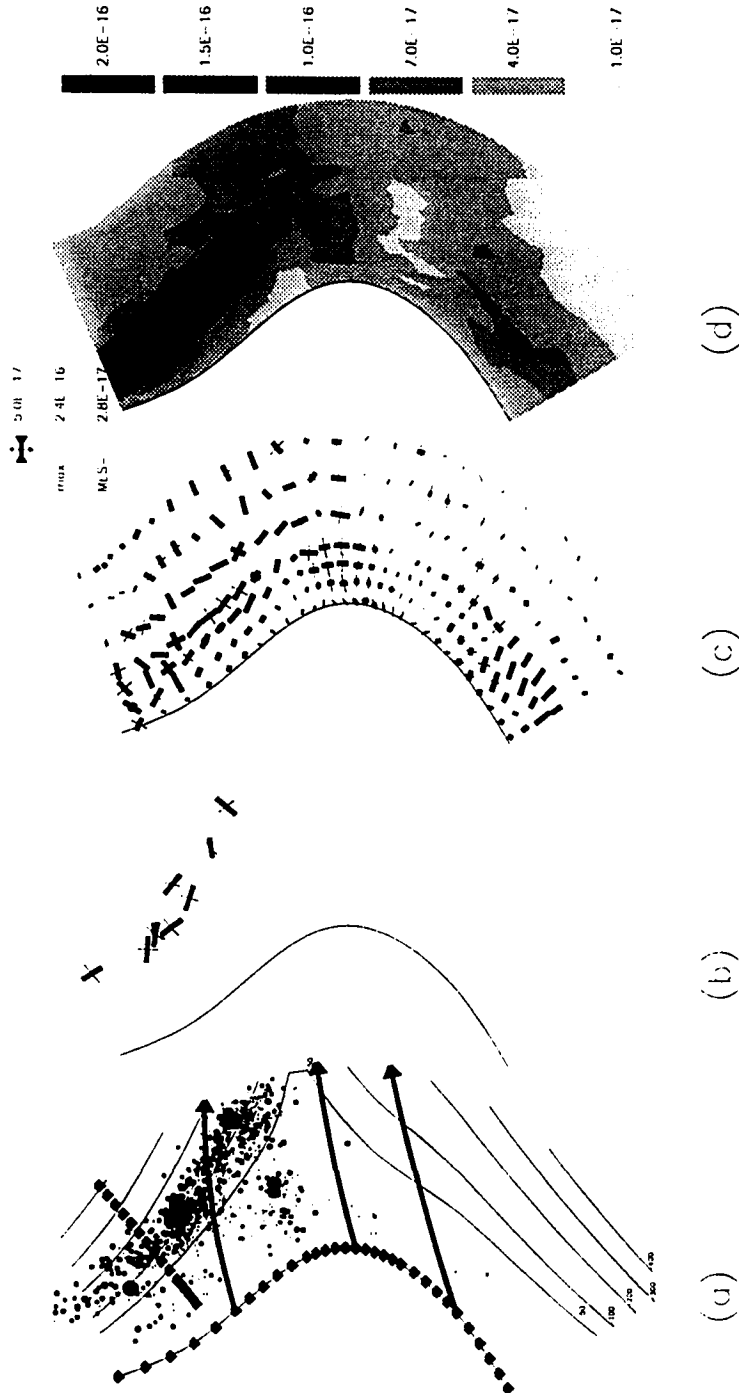


Figure 4.7 The *Alaska* experiment: (a) Depth contours showing the resulting slab structure with slab seismicity deeper than 70 km, note that boundary conditions set on the slab geometry are marked by small filled squares, (b) Available CMT solutions, same as in figure 4.5b, (c) orientations of principal axes of membrane strain rates, and (d) the distribution of the effective strain rate. See caption of Figure 2.9 for general explanations.

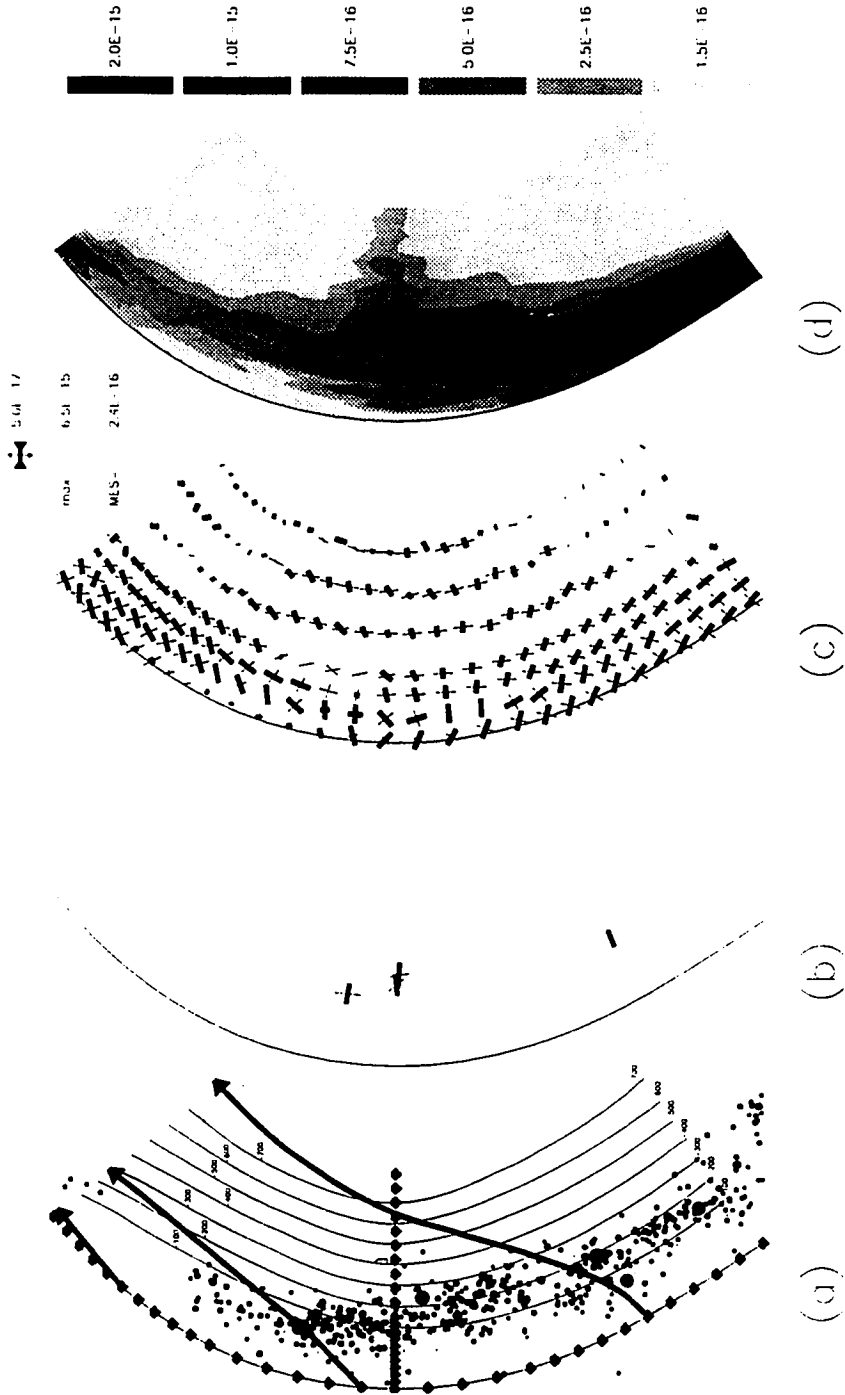


Figure 4.8 The *Aleutian* experiment: (a) Depth contours showing the resulting slab structure with slab seismicity deeper than 70 km, note that boundary conditions set on the slab geometry are marked by small filled squares, (b) Available CMT solutions, same as in figure 4.5b, (c) orientations of principal axes of membrane strain rates, and (d) the distribution of the effective strain rate. See caption of Figure 2.9 for general explanations.

4.2 The NW-Pacific Subduction zone

4.2.1 Slab seismicity and slab geometry

Lateral deformation in the along-arc direction in the NW-Pacific subduction zones have been the subject of interest of several studies in the past two decades. As already described in chapter 1, the along-arc variation of slab dip angle as shown in Figure 1.1 had been a well documented observation that motivated most of these studies. Isacks and Molnar [1971] is the first to propose two possible underlying slab structures around the Hokkaido corner (a tear or a continuous contortion). In a more recent study Chiu et al. [1991] uses three dimensional computer graphics to construct the slab geometry along the entire NW-Pacific subduction zones based on Wadati-Benioff seismicity. Reproduced from their study, Figure 4.9 shows the perspective view of the structures of (a),(c) Kuril-Japan-Izu-Bonin system and (b),(d) Bonin-Mariana system. These drawings indicate dramatic along-arc variations of slab geometry especially at places where the trench change its orientation to concave-oceanward e.g., Hokkaido corner and Izu corner. The *arch* structures in the slab at these places are clearly implied by the seismicity. Figure 4.10 is the seismic moment release plot similar to the one for the Alaska-Aleutian Subduction Zone (Figure 4.2). Starting from the Kuril Subduction Zone, the deepest seismicity reaches near 700 km depth in the center while the seismic activities shoals to both ends. Approaching the western limb of the Aleutian trench to the north, a clear pattern of lack of seismicity can be observed. The southwestern edge of this subduction is the Hokkaido Corner, a lack of deep seismicity below 300 km depth there has also been reported [e.g. Lundgren and Giardini, 1990]. Although marked by a shallow $\sim 30^\circ$ dip (see Figure 1.1), deep seismicity reaches 600 km in the Japan subduction zone. The Izu corner has a similar deep seismicity gap below 350 km as the one in the Hokkaido corner. Since it is an unstable triple junction between Eurasia, Pacific and Philippine Sea Plate; the trench configuration here would have to evolve with time. The Izu-Bonin and Mariana slabs have more complicated configurations. The deep seismicity increase from 400 km to 600 km toward south in the Izu-Bonin Zone when the slab dip varies from 40° to 80° . Approaching the Izu-Bonin/Mariana corner, the Wadati-Benioff zone becomes vertical and even appears to curl under slightly beneath northern Marianas.

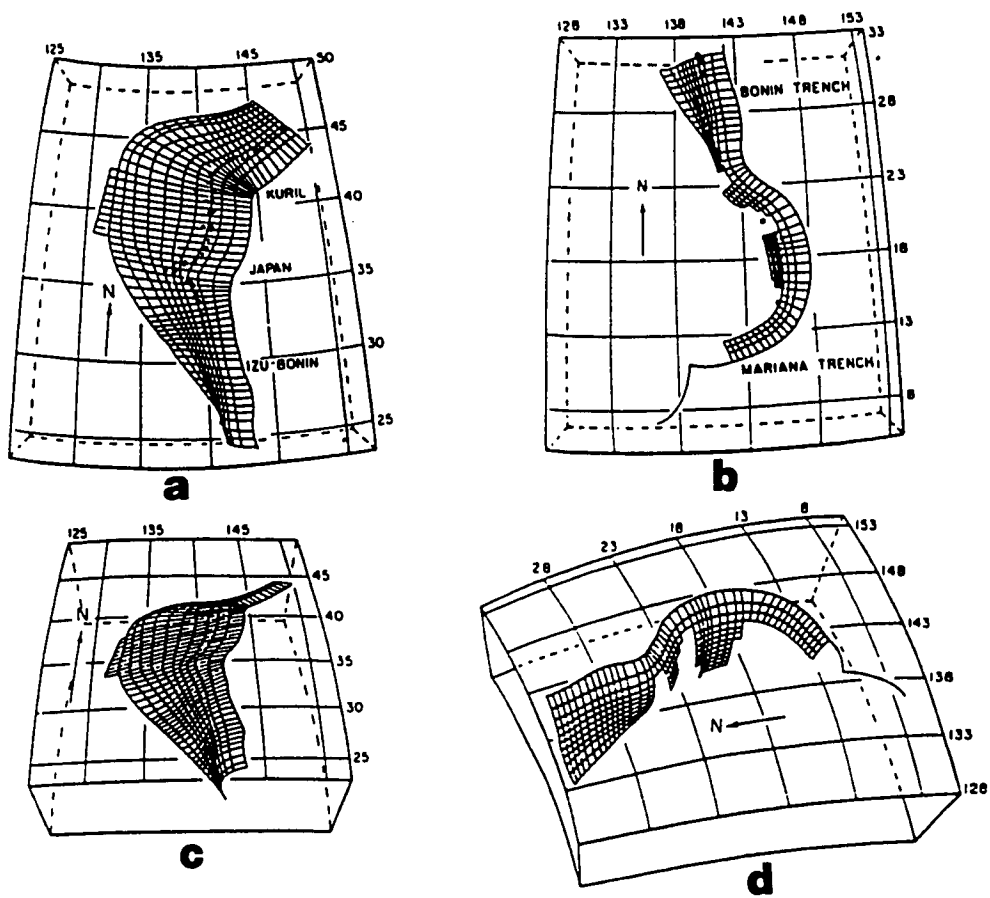


Figure 4.9 Three-dimensional perspective view of the geometry of the subducted slab of (a),(c) Kuril-Japan-Izu-Bonin system, and (b),(d) Bonin-Mariana system. [reproduced from Chiu et al., 1991].

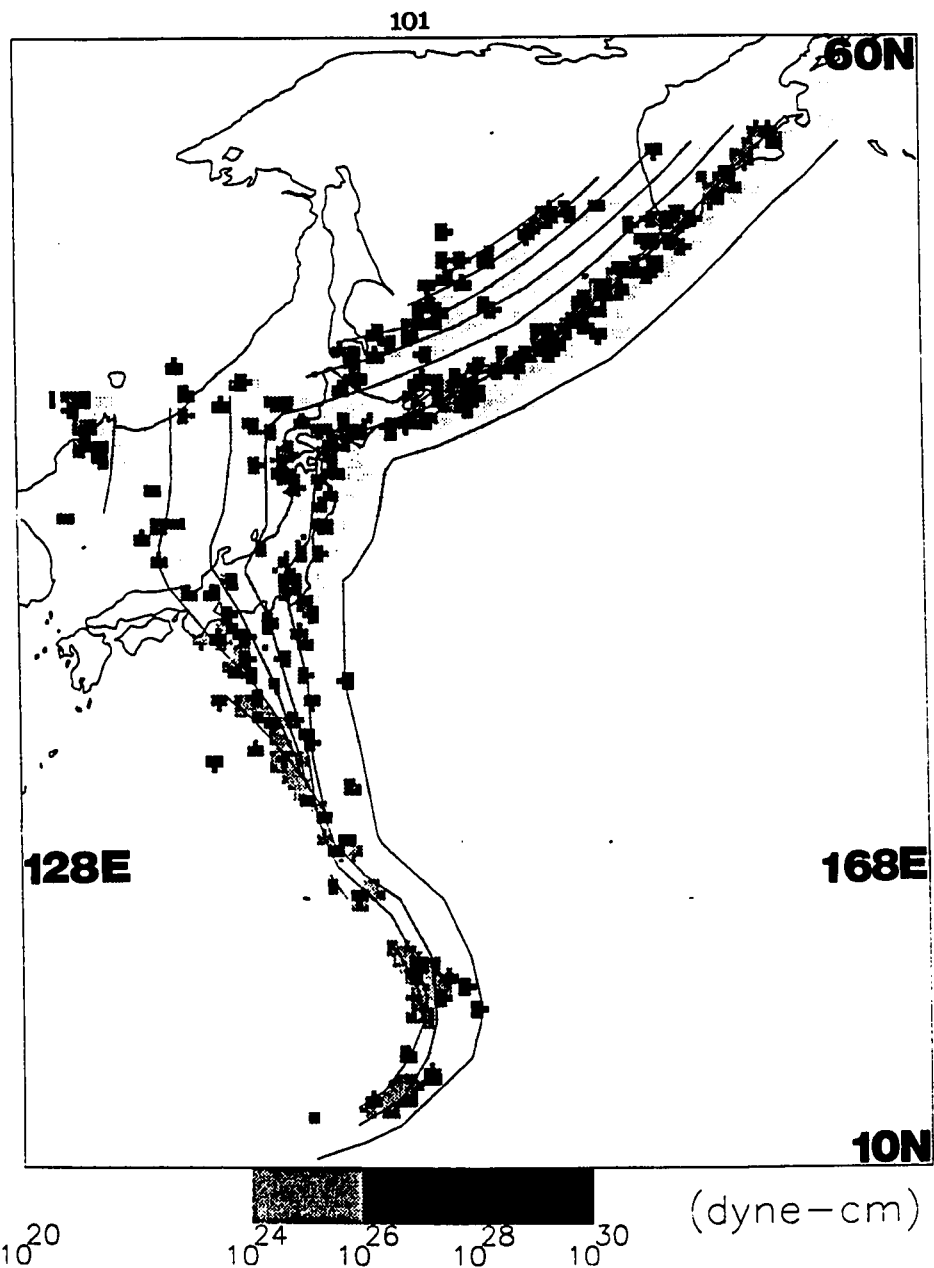


Figure 4.10 Seismic moment release of the NW-Pacific subduction zones, the region is divided into 40 km by 40 km cells, all the earthquakes deeper than 70 km from ISC (1964-1984) and from the catalog of large earthquakes of this century [Astiz et al., 1988] that fall in the same cell are converted to seismic moment (see Equation 3.1) and summed. (a) Map view. The depth contours (contour interval 100 km) are inferred from deep earthquakes. Solid lines is the trench. ((b) Projected to a cylindrical surface roughly parallel to the along-arc direction.

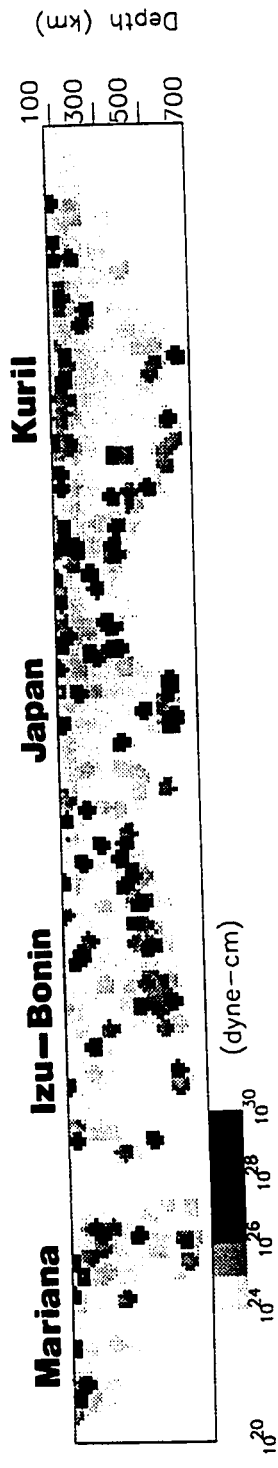


Figure 4.10 (Continued)

4.2.2 Deformation regime revealed from focal mechanisms

Beside the general slab geometry and the seismicity, the deformation regime revealed by focal mechanisms of intermediate and deep earthquakes, especially those from CMT solutions published by the Harvard group, is also a topic of great interest. A collection of the CMT solutions (1/1977 - 7/1986) below 70 km in this region are plotted in Figure 4.11 by projecting their P and T (most and least compressive) axes on a map view. No clear systematic variation can be detected in this plot. Zhou [1990], however, points out an intriguing pattern of along-arc variation of the occurrence depth of the P-T transition (down-dip extension to down-dip compression transition) that are deeper in both the Hokkaido corner (the junction between Kuril Trench and Japan Trench), and the Izu corner (the junction between Japan Trench and Izu-Bonin Trench) which are coincident with the two distinct concave-oceanward tight corner (Figure 4.12). Lundgren and Giardini [1990], examined both the distribution of seismicity and the focal mechanism around the Hokkaido corner, they showed evidence in support of both hinge faulting and continuous contortion around this concave-oceanward trench with a rather tight curvature and suggest that a plausible model is to allow the cold core of the slab to bear the hinge faulting mechanism while allowing the surrounding mantle flow to behave in a continuous, contorted fashion.

4.2.3 Previous modelling works

Previous modelling efforts include both Burbach and Frohlich [1986], and Yamoko et al. [1986]. Yamoko et al. indicate by their analog experiment that except near the Bonin-Mariana junction the slab is likely to be continuous from Kuril-Kamchaka to Japan and to Izu-Bonin Subduction Zone, and that a tear in the Bonin-Mariana junction would reduce much of the lateral extension and thus obtain a better fit to the slab geometry there. Figure 4.13 shows the results from Burbach and Frohlich's study which can be summarized as the following: In the Kuril-Kamchatka zone, model calculation yields an average 10% accumulated extension after 10 my of subduction along this arc. Approaching Hokkaido Corner, there are no evidence that shows overlapping in

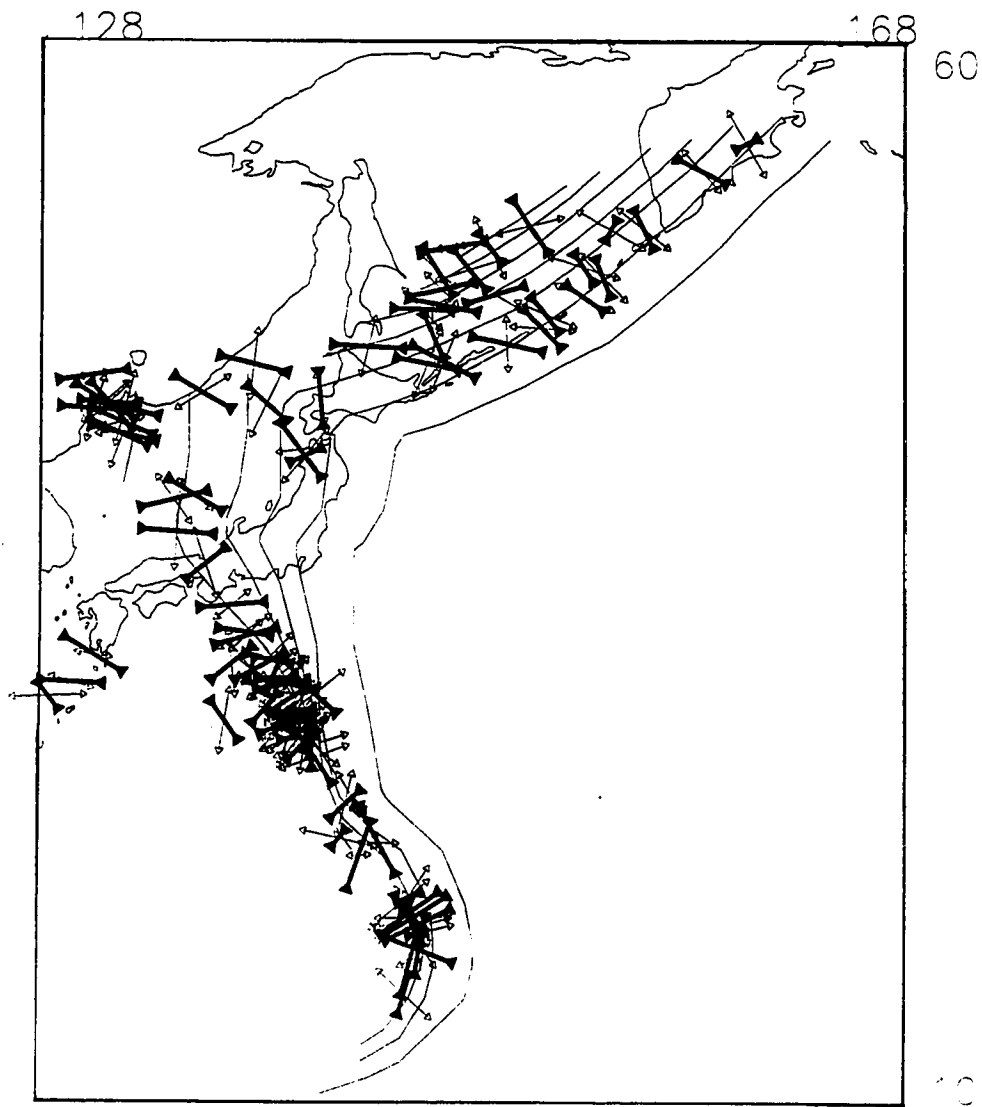


Figure 4.11 Map view of the orientation of the principal P and T axes (least and most compressive axes) of CMT solutions deeper than 70 km during 1/1977 - 7/1986.

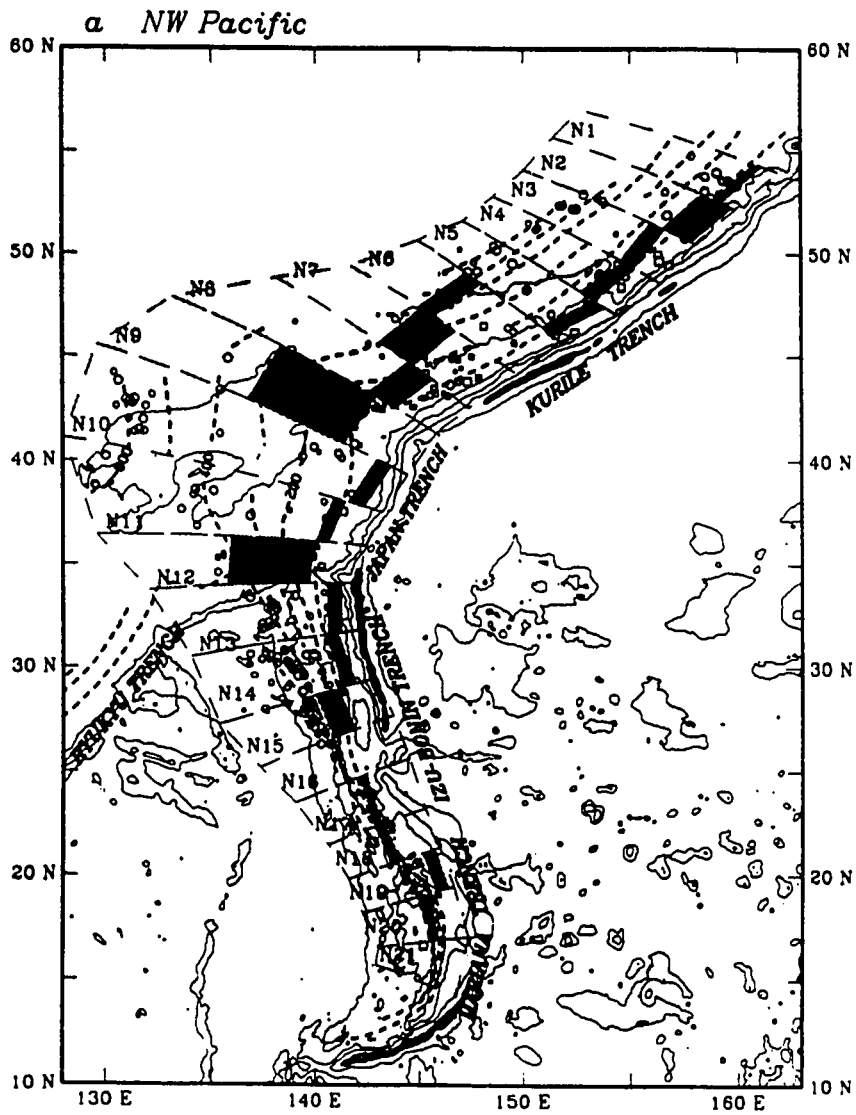


Figure 4.12 Along arc variation of the neutral down-dip stress zone (NDSZ) which marks the depth of transition from down-dip tension to compression within the slab in the NW-Pacific Subduction Zone, [after Zhou, 1990].

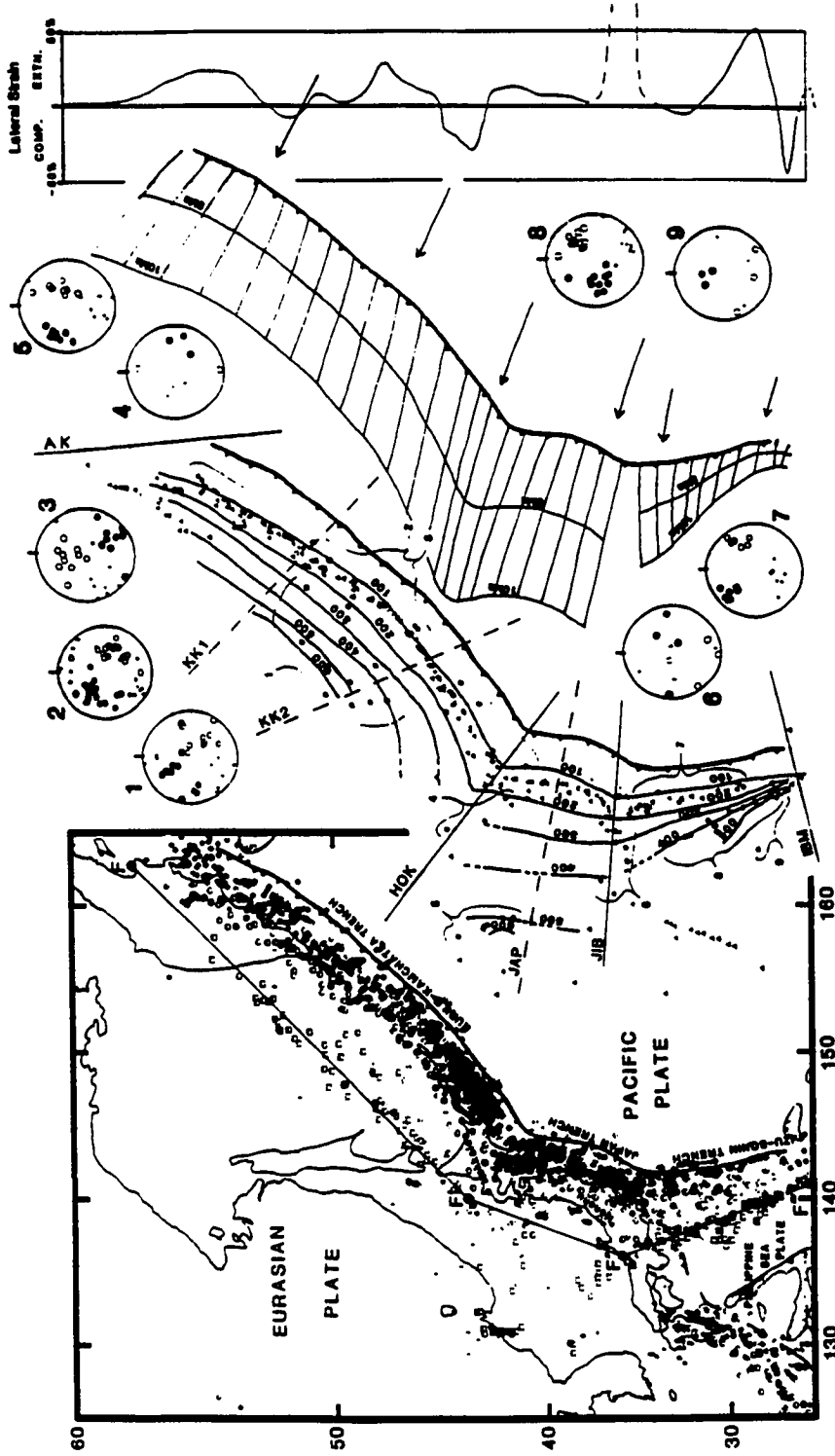


Figure 4.13 Modelling results from Burbach and Frolich's (1986) study showing the seismicity, lateral deformation and selected focal mechanisms in the NW-Pacific subduction zones. See also captions of Figure 4.3 for general explanation of plots.

teleseismic data, suggesting that a continuous buckled slab structure is in favor around this corner rather than a tear, 30% shortening in this region is modelled by their algorithm. The Honshu (Japan) arc, modelled by an average of 35° slab dip, they estimate 5-15% lateral extension along this arc. Mostly lateral extensional CMT mechanisms are explained in terms of either lateral extension or buckling of the subducted slab near Izu corner. Down-dip compression and lateral extension dominate the CMT mechanisms in the Izu-Bonin slab. In the Mariana region, 25-55% extensional strains is predicted by their modelling, probably caused by the tight curvature of the trench and the extraordinarily steep dip. This large tensional strains is consistent with most of the CMT mechanisms in this area which have mostly lateral tensional axes.

4.2.4 Modeling efforts in this study

The complete Kuril-Japan-Izu-Bonin-Marian system has a rather complicated trench shape, in order to focus on examining the effect of concave-oceanward bend of the trench, we concentrate our preliminary experiment around the Hokkaido corner and Izu corner using highly simplified linear segments representing the trench shape. Figure 4.14a shows this highly idealized trench shape and the predicted slab geometry after the iterative optimization process. The starting model for this optimization is again a constant-dip geometry, and the boundary condition as marked by the small filled squares are simply fixing the two cross-sections on the bounding edge. The predicted slab geometry in Figure 4.15a shows a pair of arches with an overall shape similar to the slab geometry constrained by slab seismicity (Figures 1.2 and 4.8c). Since the shape of the trench is not very realistic and the boundary condition on the southern edge corresponding to the Izu-Bonin slab has a slab dip too shallow, the result of this experiment can only be interpreted qualitatively. The CMT solutions shown in 4.14b and also in Figure 4.10 do not show systematic patterns that correlate well with the calculated strain-rate orientation shown in 4.14c. However, 4.14c does show an interesting concentration of down-dip extension to greater depth on top of the two arches which is consistent to the variation of P-T transition pointed out by Zhou [1990] (see Figure 4.12). In other words, his observation concerning deeper occurrence of down-dip

extension in the two corners can be attributed to the effect of the additional component of significant lateral compression on top of the usual gravitational pulling within the slab.

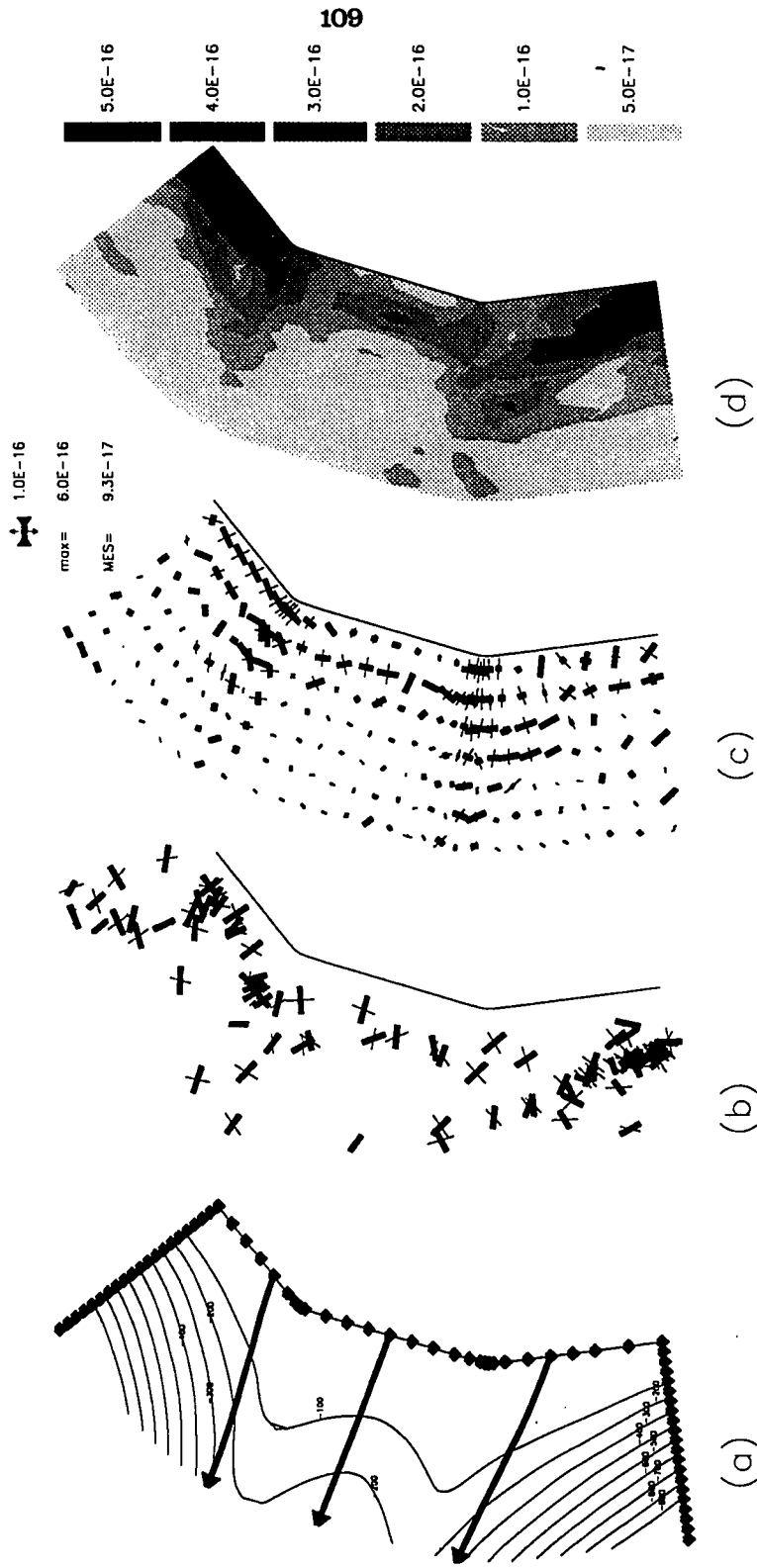


Figure 4.14 The *NW-Pacific* optimization experiment: Boundary conditions set on the slab geometry are such that the cross-sections on both of the two edges are fixed, their position are marked by filled squares. (a) Depth contours showing the resulting slab structure, (b) Available CMT solutions deeper than 70 km, (c) Orientations of principal axes of the membrane strain rates, and (d) The distribution of the effective strain rate. See the caption of Figure 2.9 for general explanations of the plot.

Chapter 5 Summary and Discussions

Lateral deformation of the subducted oceanic lithosphere has been a problem of geophysical concern mainly because of its possible role on the evolution of the structure of subduction zone systems. More importantly, it can be a seismic generating mechanism that might at least account for part of the along-arc variation of seismic activities. Interesting observations including the lateral variation of subducted slab geometry, the forming of cusps at arc-arc junction and the "space problem", well recognized in the past, had only been addressed qualitatively. This is mainly because of the fact that although conceptually and physically simple, the quantification of the membrane deformation for an arbitrary non-Euclidean surface is not a trivial task. The surface projection operation defined in Creager and Boyd [1991] and chapter 2 is a natural way to accomplish the forward computation if we know the flow field representing the subduction process in the three-dimensional space. It is conceptually and computationally simple since the whole calculation can be performed in a fixed Cartesian coordinate system even though the surface mapped by the flow field can be arbitrary. In modelling real subduction zones, however, we can only constrain the flow field on the surface before subduction. We also have only partial information on the slab geometry by using constrains from slab earthquake hypocenters and other direct and indirect seismic techniques including: residual-sphere analysis, P-to-S receiver function analysis and tomographic studies. An interpolation or inversion scheme has to be devised to determine the optimal slab geometry and the the flow field representing subduction process satisfying the constrains derived from observations for the purpose of estimating the membrane deformation in the slab. We use a minimum dissipation power principle to construct the inversion scheme in the sense that we hope to find and quantify the configuration with the least amount of membrane deformation rates among all admissible solutions that are consistent with observations. By using this algorithm, we first focus on the fundamental problem of examining the effect of trench shapes on the slab geometry and the possible implications on the spatial distribution of seismic activity.

Experiments on the Cascadia Subduction Zone suggest that the possible arch structure underneath the Puget Sound area is a natural consequence of the subducted slab

trying to reduce the along-arc compression caused by the concave-oceanward bend of the trench. This arch structure, as predicted by our inversion experiments described in chapter 3, not only is consistent with the local geophysical and geological observations, but also provides a natural explanation for the concentration of the local slab seismicity underneath Puget Sound Basin. Equipped with the "Critical Taper Theory" by Davis et al. [1983], this arch might also shed important insights on the forming of the thick accretionary prism that essentially makes up Olympic Mountains.

The effective strain-rate for both the bending and membrane deformation rates in this subduction zone are on the order of 10^{-16} per sec which is an order of magnitude lower than the other two subduction zones modelled. This might serve as an explanation that the seismic activity is generally much lower than other subduction zones.

Our preliminary experiments on both the Aleutian Zone and the NW-Pacific Zone again reveal the robust feature of arch structures associated with concave-oceanward bend of the trench. These predicted arch structures greatly reduce the potential lateral compression within the subducted slab and alter the deformation regime. The large scale structure of the slab predicted by minimizing the membrane deformation are usually consistent with the slab structure inferred from seismic observations, even when we use only minimal boundary constrains. Also, the predicted distribution of deformation generally correlates well with the spatial distribution of slab seismicity. These suggest that the lateral membrane deformation of the subducted slab is an important mechanism in controlling the slab geometry and seismic generating process.

We have not yet been able to establish detailed correlations of the orientation of calculated membrane strain-rates with the observed focal mechanisms. This is mainly because, although the spatial distribution of the orientation of calculated strain-rates generally yield systematic variation for simple subduction zone geometries, the focal mechanisms for the same zone are usually quite scattered and often lack obvious simple patterns. At places like Alaska-Aleutian Zone where the focal mechanisms do show clear trend (along-arc extension and along-arc compression) our model generally shows consistent results. One important reason for the lack of higher success in applying this scheme to examine the detailed pattern of focal mechanisms can be attributed to the fact

that our modelling does not involve possible dynamic controls of the subduction process, namely, the gravitational pulling, the compressibility associated with major transition zones and the viscous drag exerted on the slab and mantle winds. The complete pattern of deformation rates within subducted slabs is a combined result of the dynamics mentioned above and the interplay of membrane- and bending-deformation. Our study shows that the lateral membrane deformation arising mainly from kinematic and geometric boundary conditions is a basic mechanism of fundamental importance. Examples like the systematic variation of focal mechanisms in Alaska-Aleutian Zone indicate that the concept of membrane deformation can provide useful insights towards understanding the deformation regime of subducting slabs that is beyond the reach of the conventional two-dimensional model.

Lacking the involvement of important dynamic controls in our optimization algorithm also caution us in interpreting the obtained slab geometry. However, without addressing the detail structure of the obtained geometry, the forming of an arch structure with a shallower dip seems to be a robust feature related to the backward curvature (or concave-oceanward bend) of the trench in all experiments. Also, the spatial distribution of the seismic activity is usually coincident with concentration of high membrane deformation rates. Overall, the experiments show at least that the lateral deformation is a very important mechanism that deserve more attention. One way of applying this method is then to regard the geometry inversion as an interpolation scheme. Instead of trying to actually predict the overall slab geometry, more available geometric information should be incorporated as boundary conditions to setup at least the low wavenumber, large scale framework of the slab shape, and let the optimization algorithm to fine tune the geometry where it is poorly constrained. However, the success of predicting general trend of the slab geometry like the arch structure by using minor fixed boundary conditions strongly suggest that the membrane deformation is an important mechanism in shaping the slab geometry.

Based on the preliminary experiments on the three subduction zones presented in chapter 3 and chapter 4. We think the method described in this study is a promising tool in examining and quantifying the slab geometry and the associated lateral deformation.

We intend to extend our modeling experiments to perform systematic examination on all the major subduction zones.

Possible improvements on the present scheme might include the following:

- (1) Incorporate gravitational pulling. Conceptually, the difficulty involved with implementing the dynamics of the subduction process is mainly that the relative contribution of each component are largely unknown. To formulate a self-consistent, well balanced dynamic system representing the subduction process is thus extremely difficult. However, incorporating the gravitational pulling can be achieved by adding an additional term, describing the potential energy input rate, into the dissipation power functional that is minimized. By using different weighting on this newly added term in a trial and error fashion, we can at least examine a broader range of possible solutions and examine the possible effects of superposing the gravitational pulling. Another way to incorporate the controlling dynamics is to use simple parameterized approximation to dynamics which depends on a few parameters and slab geometry in two-dimensional cross section [e.g. Kemp and Bird, 1989].
- (2) Rheology and thermal structure. As the slab heats up, its reology changes. presumably the slab's effective viscosity decrease. A variable viscosity as a function of temperature is easily incorporated in our calculation.
- (3) Compressibility associated with phase transitions. Since major phase transitions occur within relatively narrow depth ranges and cause significant change of volume, the effect of these transitions on the slab geometry and internal deformation are probably significant . For example, Rogers [1983] used basalt-eclogite transition as one possible solution for the space problem in Cascadia Subduction Zone. However, how phase transitions translate in terms of strain or strain-rate is not yet clear. Recent work on how materials behave when going through a phase transition [R. Delinger, personal communication] will help in incorporating these effects in our modelling.
- (4) Incorporate bending deformation rate. Estimating bending deformation rates for subduction process needs higher order information on slab geometry, since it is directly proportional to the local change of curvature. To devise a discrete

parameterization of the geometry with piecewise continuous change of curvature (a nonlinear third order term) is technically difficult. The Clough-Tocher element used for interpolating slab geometry in this study is a C^1 element. One possible way to formulate bending deformation is then to use element average curvature and estimate the change of curvature by robust finite difference scheme to get piecewise estimate of the change of curvature.

Bibliography

- Akima, H., A new method of interpolation and smooth curve fitting based on local procedures., *J. Assoc. Comp. Mach.*, 17, 589-602, 1970.
- Aris, R., *Vectors, Tensors, and the basic equations of fluid mechanics*, Prentice-Hall Inc., Englewood Cliffs, N.J., 286 pp, 1962.
- Astiz, L., T. Lay, and H. Kanamori, Large intermediate-depth earthquakes and the subduction process, *Phys. Earth and Planet. Inter.*, 53, 80-166, 1988.
- Backus, G. E., Converting vector and tensor equations to scalar equations in spherical coordinates, *Geophys. J. Roy. astron. Soc.*, 13, 71-101, 1967.
- Baker, G.E., and C.A. Langston, Source parameters of the 1949 magnitude 7.1 South Puget Sound, Washington, earthquake as determined from long-period body waves and strong ground motions, *Bull. Seismol. Soc. Am.*, 77, 1530-1557, 1987.
- Bevis, M., The curvature of Wadati-Benioff zones and the torsional rigidity of subducting plates, *Nature*, 323, 52, 1986.
- Bevis, M., and B. L. Isacks, Hypocentral trend surface analysis: probe the geometry of Benioff Zones, *J. Geophys. Res.*, 89, 6153-6170, 1984
- Bevis, M., Seismic slip and down-dip strain rates in Wadati-Benioff zones, *Sciences*, 1317-1319, 1988
- Boyd, T.M., and K.C. Creager, The geometry of Aleutian subduction: Three-dimensional seismic imaging, *J. Geophys. Res.*, 96, 2267-2291, 1991
- Brandon, M.T., and A.R. Calderwood, High-pressure metamorphism and uplift in the Olympic subduction complex, *Geology*, 18, 1252-1255, 1990.
- Briggs, I.C., Machine contouring using minimum curvature, *Geophysics*, 39, 39-48, 1974.
- Burbach, G. V. and C. Frohlich, Intermediate and deep seismicity and lateral structure of subducted lithosphere in the circum-Pacific region, *Rev. Geophys. Space Phys.*, 24, 833-874, 1986.
- Cady, W.N., Tectonic setting of the tertiary volcanic rocks of the Olympic Peninsula, Washington, *J. Res. USGS* 3, 573-582, 1975.
- Cadwell, J.G., W.F. Haxby, Karig, D.E., and D.L. Turcotte, On the applicability of a universal elastic trench profile, *Earth Planet. Sci. Let.*, 31, 239-246, 1976.

- Calladine, C. R., *Theory of shell structures*, Cambridge University Press, Cambridge, 763 pp, 1988.
- Chapple, W.M., and D. W. Forsyth, Earthquakes and bending of plates at trenches, *J. Geophys. Res.*, 84, 6729-6749, 1979.
- Chiu, J.-M., B.L. Isacks, R.K. Cardwell, 3-D configuration of subducted lithosphere in the western Pacific, *Geophys. J. Int.*, 106, 99-111, 1991
- Clough, R.W., and J.L. Tocher, Finite element stiffness matrices for analysis of plates in bending. *Proc. Conf. Matrix Methods in Structural Mechanics*, Wright-Patterson A.F.B., Ohio, 1965.
- Creager, K.C., and T.M. Boyd, The geometry of Aleutian subduction: Three-dimensional kinematic flow modelling, *J. Geophys. Res.*, 96, 2293-2307, 1991.
- Crosson, R.S., Review of seismicity in the Puget Sound region from 1970 through 1978, *U.S. Geol. Surv., Open-File Rept.*, 83-19, 6-18, 1983.
- Crosson, R.S., and T.J. Owens, Slab geometry of the Cascadia subduction zone beneath Washington from earthquake hypocenters and teleseismic converted waves, *Geophys. Res. Letts.*, 14, 824-827, 1987.
- Davis, E. E., and R.D. Hyndman, Accretion and recent deformation of sediments along the northern Cascadia subduction zone, *Geol. Soci. Amer. Bull.*, 101, 1465-1480, 1989.
- Davis, D., J. Suppe and F. A. Dahlen, Mechanics of fold-and-thrust belts and accretionary wedges, *J. Geophys. Res.*, 88, 1153-1172, 1983.
- DeBremaecker, J.C., Is the oceanic lithosphere elastic or viscous ? *J. Geophys. Res.*, 82, 2001-2004, 1977.
- De Fazio, T.L., Island-arc and underthrust plate geometry, *Tectonophysics*, 23, 149, 1974.
- DeMets, C. G., R. G. Gordon, D.F. Argus, and S. Stein, Current plate Motions, *Geophys. J. International*, 101, 425-478, 1990.
- Dickinson, W.R., Relations of andesites, granites, and derivative sandstones to arch-trench tectonics, *Rev. Geophys.*, 8, 813-860, 1970.
- Dziewonski, A.M., and D.L. Anderson, Preliminary Reference Earth Model, *Physics of the Earth and Planetary Interiors*, 25, 297-356, 1981.

- Dziewonski, A.M., T.A. Chou, and J.H. Woodhouse, Determination of earthquake source parameters from waveform data for studies of global and regional seismicity, *J. Geophys. Res.*, 86, 2825-2852, 1981.
- Dziewonski, A.M., and J.H. Woodhouse, An experiment in the systematic study of global seismicity: centroid-moment tensor for 201 moderate and large earthquakes of 1981, *J. Geophys. Res.*, 88, 3247-3271, 1983.
- Finlayson, B. A., *The method of weighted residuals and variational principles with applications in fluid mechanics, heat and mass transfer*, Academic Press, 1972.
- Forsyth, D., Lithosphere: Mechanical properties, *The Encyclopedia of solid earth geophysics*, edited by D.E. James, Van Norstrand Reinhold company, New York, 1989.
- Forsyth, D. and S. Uyeda, On the relative importance of the driving forces of plate motion, *Geophys. J. R. Astron. Soc.*, 43, 165-200, 1975.
- Frank, Curvature of island arcs, *Nature*, 220, 363, 1968.
- Freeth, S.J., Can membrane tectonics be used to explain the break-up of plates ?, in: Davis, P.A. and S.K. Runcorn (ed) *Mechanics of continental drift and plate tectonics*, Academic Press, 1980.
- Giardini, D., Systematic analysis of deep seismicity: 200 centroid-moment tensor solutions for earthquakes between 1977 and 1980, *Geophys. J. R. Astron. Soc.*, 77, 883-914, 1984.
- Gill, P.E., and W. Murray, Newton-type methods for unconstrained and linearly constrained optimization, *Mathematical Programming*, 7, 311-350, 1974.
- Gill, P.E., W. Murray and M.H. Wright, *Practical Optimization*, Academic Press, London, 401 pp., 1981.
- Green, A.G., R.M. Clowes, C.J. Yorath, C. Spencer, E.R. Kanasewich, M.T. Brandon, and A.S. Brown, Seismic reflection imaging of the subducting Juan de Fuca plate, *Nature*, 319, 210-213, 1986.
- Gurnis, M. and B.H. Hager, Controls of the structure of subducted slabs, *Nature*, 335, 317-321, 1988.
- Hanks, T. C., The Kuril Trench-Hokkaido rise system: large shallow earthquakes and simple models of deformation. *Geophys. J. R. Astron. Soc.*, 23, 173-189, 1971.

- Hsui, A.T., Application of fluid mechanic principles to the study of geodynamic processes at the trench-arc-back arc system, *Pure Appl. Geophys.*, 128, 661-681, 1988.
- Isacks, B. L., and M. Barazangi, Geometry of Benioff Zones: Lateral segmentation and downwards bending of the subducted lithosphere, in *Island Arcs, Deep Sea Trenches and Back-Arc basins, Ewing Ser.*, vol. I, edited by M. Talwani and W. Pitman III, pp. 99-114, AGU, Washington, D. C., 1977.
- Isacks, B. L. and P. Molar, Distribution of stresses in the decending lithosphere from a global survey of focal mechanism solutions of mantle earthquakes, *Rev. Geophys. Space Phys.*, 9, 103-174, 1971.
- Isacks, B. L., J. Oliver, and L. R. Sykes, Seismology and the new global tectonics, *J. Geophys. Res.*, 73, 5855-5899, 1968.
- Kanamori, H. and D. L. Anderson, Theoretical basis of some empirical relations in seismology, *Bull. Seismol. Soc. Am.*, 65, 1073-1095, 1975.
- Kawakatsu, H., Double seismic zones: A first order feature of plate tectonics, ph.D. Dissertation, Stanford University, 201 pp., 1985.
- Keach, R.W., C.J. Potter, J.E. Oliver, and L.D. Brown, Cenozoic active margin and shallow Cascades structure: COCORP results from western Oregon (abstract), *Geological Society of America Abstracts with Programs*, 18, 652, 1986.
- Kemp, D.V., and P. Bird, A model for the mechanics of flexible subducted lithosphere, *Eos Trans. AGU*, 70, 1315, 1989.
- Kienle, J., S.E. Swanson, and H. Pulpan, Magmatism and subduction in the eastern Aleutian Arc., *Arc Volcanism: Physics and Tectonics*. edited by D. Shimozuru and I. Yokoyama; Terra Scientific Publishing Co., Tokyo, 191-224, 1983.
- Kissling E., and J.C. Lahr, Tomographic image of the Pacific Slab under southern Alaska, *Eclogae geol. Helv.*, 84, 297-315, 1991
- Lancaster, P., and K. Salkauskas, *Curve and Surface Fitting*, Academic press, London, 280 pp, 1988.
- Langston, C.A., and D.E. Blum, The April 29, 1965, Puget Sound earthquake and the crustal and upper mantle structure of western Washington. *Bull. Seismol. Soc. Am.*, 67, 693-711, 1977.

- Lapp, D.B., T.J. Owens, and R.S. Crosson, P-waveform analysis for local subduction geometry south of Puget Sound, Washington, *PAGEOPH*, 133, 349-365, 1990.
- Laravie, J.A., Geometry and lateral strain of subducted plates in island arcs, *Geology*, 3, 484-486, 1975.
- Lee, E.H., and G.E. Forsythe, Variational study of nonlinear spline curves, *SIAM Review*, 15, 1, 120-133, 1973.
- LePichon, X., J. Francheteau, and J. Bonnin, *Plate Tectonics*, Elsevier, New York, 229 pp., 1978.
- Liboutry L.A., *Very Slow Flows of Solids-Basics of Modeling in Geodynamics and Glaciology*, Martinus Nijhoff Publishers, Dordrecht, 510 pp., 1987.
- Ludwin, R.S., C.S. Weaver, and R.S. Crosson, Seismicity of Washington and Oregon, in: Slemmons, D.B., E.R. Engdahl, D. Blackwell and D. Schwartz, (ed.), *Decade of North American Geology associated volume CSMV-1, Neotectonics of North America*, 1990.
- Lundgren P.R. and D. Giardini, Lateral structure of the subducting Pacific Plate beneath the Hokkaido corner from intermediate and deep earthquakes, *PAGEOPH*, 134, 385-404, 1990.
- Marquardt, D.W., An algorithm for least squares estimation of nonlinear parameters, *SIAM J. Appl. Math.*, 11, 431-441, 1963.
- McAdoo, D.C., J. C. Caldwell, and D. L. Turcotte, On the elastic-perfectly plastic bending of the lithosphere under generalized loading with application to the Kuril Trench, *Geophys. J. R. astr. Soc.*, 54, 11-26, 1978.
- McKenzie, D. P., Speculations on the consequences and causes of plate motions, *Geophys. J. R. Astron. Soc.*, 18, 1-32, 1969.
- McNutt, M., Lithospheric flexure and thermal anomalies, *J. Geophys. Res.*, 89, 11180-11194, 1984.
- Melosh, H.J., Dynamic support of the outer rise, *Geophys. Res. Lett.*, 5, 321-324, 1978.
- Melosh, H. J., and A. Raefsky, The dynamic origin of subduction zone topography, *Geophys. J.*, 60,333-354, 1979.

- Minamino, T., and N. Fuji, The effect of the contorted "nose" of a subducting slab on the stress field in the continental lithosphere at an arc-arc junction, *Geophys. J. R. Astron. Soc.*, 67, 145-158, 1981.
- Mister, J. B., and T. H. Jordan, Present-day plate motions, *J. Geophys. Res.*, 83, 5331-5354, 1978.
- Murray, W., Second Derivative Methods, *Numerical Methods for Unconstrained Optimization*, Academic Press, London and New York, 1972.
- Nishimura, C., D. S. Wilson and R. Hey, pole of rotation analysis of present day Juan de Fuca plate motion, *J. Geophys. Res.*, 89, 10283-10290, 1984.
- Olszak, W., and A. Sawczuk, *Inelastic behaviour in shells*, P. Noordhoff Ltd. Groningen, The Netherlands., 1967.
- Owens, T.J., R.S. Crosson, and M.A. Hendrickson, Constrains on the subduction geometry beneath western Washington from broadband teleseismic waveform modelling, *Bull. Seismol. Soc. Am.*, 78, 1319-1334, 1988.
- Page, R.A., C.D. Stephens, and J.C. Lahr, Seismicity of the Wrangell and Aleutian Wadati-Benioff zones and the North-American plate along the trans-Alaska crustal transact, Chugach Mountains and Copper River Basin, Southern Alaska, *J. Geophys. Res.*, 94, 16059-16082, 1989.
- Pearson, C. E. (ed.), *Handbook of Applied Mathematics*, 2nd ed., Van nostrand Reinhold, New York, 1306 pp., 1990.
- Phipps, J.B., and C. Peterson, General submergence of Grays Harbor, Washington during the Holocene (abstract), *EOS*, 70,1332, 1989.
- Pulpan, H., and C. Frolich, Geometry of the subducted plate near Kodiak Island and lower Cook Inlet, Alaska, determined from relocated earthquake hypocenters, *Bull. Seismol. Soc. Am.*, 75, 791-810, 1985.
- Rasmussen, J., and E. Humphreys, Tomographic image of the Juan de Fuca plate beneath Washington and western Oregon using teleseismic P-wave travel times, *Geophys. Res. Letts.*, 15, 1417-1420, 1988.
- Rogers, G.C., Seismotectonics of British Columbia, Ph.D. thesis, Univ. British Columbia, Vancouver, 227 pp., 1983.
- Rogers, G.C., Geometry of the Juan de Fuca Plate beneath Vancouver Island from seismicity (abstract), *EOS*, 70, 1330, 1989.

- Riddihough, R., Recent movements of the Juan de Fuca plate system, *J. Geophys. Res.*, 89, 6980-6994, 1984.
- Riddihough, R. P., M. E. Beck, R.L. Chase, E.E. Davis, R.D. Hyndman, S.H. Johnson and C.C. Rogers, Geodynamics of the Juan de Fuca plate,
- Scales, L.E., *Introduction to Non-Linear Optimization*, Springer-Verlag New York Inc., 242 pp., 1985.
- Scales, J.A., P. Docherty, and A. Gersztenkorn, Regularisation of inverse problem: imaging the near-surface weathering layer, *Inverse Problems*, 6, 115-131, 1990.
- Schubert, G., D. A. Yuen, and D. L. Turcotte, Role of phase transitions in a dynamic mantle, *Geophys. J. R. Astr. Soc.* 42, 705-735, 1975.
- Smith, W.H.F., and P. Wessel, Gridding with continuous curvature splines in tension, *Geophysics*, 55, 293-305, 1990.
- Snavely, P. D., and H. C. Wranger, Geologic cross section across the continental margin off Cape Flattery, Washington: *U.S. Geological Survey Open-File Report 81-0978*, 1981.
- Stauder, W., Tensional character of earthquake foci beneath the Aleutian trench with relation to sea-floor spreading, *J. Geophys. Res.*, 73, 7693-7701, 1968.
- Strobach, K., Curvature of island arcs and plate tectonics, *J. Geophys.*, 39, 819-831, 1973.
- Synge, J.L., and A. Schild, *Tensor Calculus*, Dover Publication Inc., New York, 324 pp. 1969.
- Tabor, R.W., and W.M. Cady, Geologic map of the Olympic Peninsula, scale 1:125,000, Misc. Invest. Map I-994, U.S. Geol. Surv., Reston, Va., 1978.
- Tabor, J. J., and Lewis, B.T.R., Crustal structure of the Washington continental margin from refraction data, *Bull. Seismol. Soc. Am.*, 76, 1011-1024, 1986.
- Tabor, J.J., and S.W. Smith, Seismicity and focal mechanisms associated with the subduction of the Juan de Fuca plate beneath the Olympic Peninsula, Washington, *Bull. Seismol. Soc. Am.*, 75, 237-249, 1985.
- Timoshenko, S.P., and J.N. Goodier, *Theory of Elasticity*, third edition, McGraw-Hill Inc. 567 pp, 1970.
- Tovish, A., and G. Schutbert, Island arc curvature, velocity of convergence and angle of subduction, *Geophys. Res. Lett.*, 5, 329-332, 1978.

- Tsukahara, H., Physical conditions for double seismic planes of the deep seismic zone, *J. Phys. Earth.* 28, 1-15, 1980.
- Turcotte, D.L., Membrane tectonics, *Geophys. J. R. Astr. Soc.*, 40, 33-42, 1973.
- Turcotte, D.L., Flexure, *Advances in Geophysics*, 21, 51-86, 1979.
- Turcotte, D.L., D.C. MacAdoo, and J.G. Caldwell, An elastic-perfectly plastic analysis of the bending of the lithosphere at a trench, *Tectonophysics*, 47, 193-205, 1978.
- Turcotte, D.L., and G. Schubert, *Geodynamics, Application of continuum physics to geological problems*, John Wiley & Sons, Inc., New York, 450 pp. 1982.
- Vandecar, J.C., Upper-mantle structure of the Cascadia Subduction Zone from non-linear teleseismic travel-time inversion, ph.D. dissertation, Univ. of Washington, Seattle, 165pp, 1991.
- Vassiliou, M. S. and B. H. Hager, Subduction zone earthquakes and the stress in slabs, *PAGEOPH*, 128, 547-624, 1988.
- Vogt, P.R., Subduction and aseismic ridges, *Nature*, 241, 189-191, 1972.
- Weaver, C.S., and G.E. Baker, Geometry of the Juan de Fuca Plate beneath Washington and northern Oregon from seismicity, *Bull. Seismol. Soc. Am.*, 78, 264-275, 1988.
- Weaver, C.S., and C.A. Michaelson, Seismicity and volcanism in the Pacific Northwest: evidence for the segmentation of the Juan de Fuca plate, *Geophys. Res. Letters.*, 12, 215-218, 1985.
- Yamaoka, K., Y. Fuako, and M. Kumazawa, Spherical shell tectonics: Effects of sphericity and inextensibility on the geometry of the descending lithosphere, *Rev. Geophys.*, 24, 27-55, 1986.
- Yamaoka, K., and Y. Fuako, Why do island arcs form cusps at their junctions ?, *Geology*, 15, 34-36, 1987.
- Yorath, C.J., R.M. Clowes, R.D. Macdonald, C. Spencer, E.E. Davis, R.D. Hyndman, K. Rohr, J.F. Sweeney, R.G. Currie, J.F. Halpenny, and D.A. Seemann, Marine multichannel seismic reflection, gravity, and magnetic profiles-Vancouver Island continental margin and Juan de Fuca Ridge: *Geological Survey of Canada Open-File Report 1661*, 1987.
- Zhou, H.-W., Observations on earthquake stress axes and seismic morphology of deep slabs, *Geophys. J. Int.*, 103, 377-401, 1990.

Zienkiewicz, O.C., *The Finite element method*, 3rd ed. McGraw-Hill Book Comp., London, 787 pp., 1977.

Appendix A On the shear deformation parallel to slab surface

Consider an ideal situation as shown in figure A.1, when a slab with half width h is falling vertically with a terminal velocity w_0 into the surrounding mantle. The viscosity of the mantle is assumed to be μ_2 while the slab has a constant viscosity of μ_1 , the density anomaly of the slab is $\Delta\rho$ compared to the surrounding mantle.

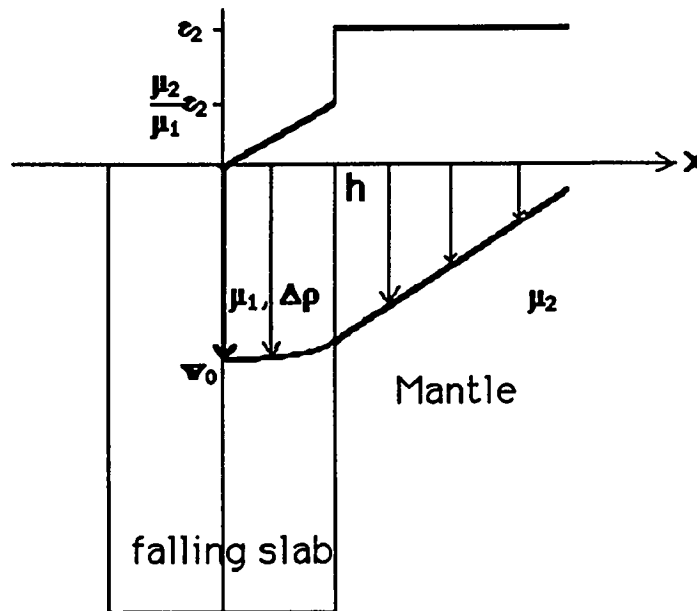


Figure A.1 An ideal slab with viscosity μ_1 is falling vertically into the surrounding mantle with viscosity μ_2 . The bold line in the lower half of the diagram shows the falling velocity profile while the upper bold line shows the strain-rate distribution at corresponding sites.

Assuming the flow behaves according to the Newtonian rheology, the governing equations for the highly simplified velocity distribution $w(x)$ are then:

$$\Delta\rho \cdot g = \mu_1 \frac{d^2 w}{dx^2}, \quad \text{within the slab} \quad \text{_____} \quad \text{(A.1)}$$

and

$$0 = \mu_2 \frac{d^2 w}{dx^2}, \quad \text{in the mantle} \quad \text{-----} \quad \text{(A.2)}$$

the strain-rate $\frac{dw}{dx}$ in the mantle is thus a constant, say it is ϵ_2 . The boundary conditions at the interface $x=h$ requires the continuity of velocity w and the shear stress:

$\mu_1 \epsilon_1 = \mu_2 \epsilon_2$; which then leads to $\epsilon_1(h) = \frac{\mu_2}{\mu_1} \epsilon_2$. Since by Equation (A.1), the variation of ϵ_1 within the slab is linear and by the symmetry of the problem

$\left. \frac{dw}{dx} \right|_{x=0} = 0$, the strain-rate distribution as shown in the upper part of the diagram in Figure A.1 clearly indicates that the maximum shear strain-rate within the slab is a factor of μ_2/μ_1 lower as compared with the surrounding mantle. Also, the dissipation power $\mu \epsilon^2$ would also have a contrast ratio of

$$\left[\mu_1 \left(\frac{\mu_2}{\mu_1} \epsilon_2 \right)^2 \right] / [\mu_2 \epsilon_2^2] = \frac{\mu_2}{\mu_1}$$

Since $\mu_1 \gg \mu_2$ from our assumption, the shear strain-rate parallel to the slab surface is then much less within the slab as compared to those in the mantle and the contrast might even be an under-estimate since toward the center of the cold core of the slab, the shear strain-rate is even lower. In summary, the assumption that the slab viscosity is orders of magnitude higher than the surrounding mantle would then allow us to make the simplification that the shear deformation parallel to the slab surface would essentially be taken up by the surrounding mantle.

The density contrast and viscosity contrast of slab versus the surrounding mantle are mainly controlled by the temperature contrast. Vassiliou and Hager (1988) gave a brief review of the existing temperature models showing that as the slab reaches 700 km depth, the core of the slab is still much colder than the surrounding mantle, the contrast ranges from 300° (McKenzie, 1969) to 800° (Schubert et al, 1975) among different models. They plotted the viscosity contrast as governed by

$$\frac{\eta_{T_1}}{\eta_{T_0}} = \frac{T_1}{T_0} e^{\frac{E}{R} \left[\frac{T_0 - T_1}{T_0 T_1} \right]} \quad \text{(A.3)}$$

where T_1 is the estimated slab temperature, T_0 is assumed initial mantle temperature, E is the activation energy for creep and a value of 5.2×10^4 J/mol for Olivine is used, and R is the universal gas constant. Figure A.2 shows the viscosity ratio redrawn from Vassiliou and Hager (1988), which shows that the viscosity contrast of the cold core of the slab is essentially infinite with respect to the mantle. They then argue that although the microscopic viscosity of the slab as shown in the plot is very high, other evidence from studies on the topography of the outer arc bulge and the trench, and from post-glacial rebound studies suggest that the macroscopic viscosity contrast might be lower and adopt a contrast ratio of ten as comparing the slab viscosity to the surrounding mantle. In their modeling of subduction flow, however, they point out that for Power-Law rheology ($n=3$), contrasts of 10^5 is needed to generate reasonable subduction flow velocity.

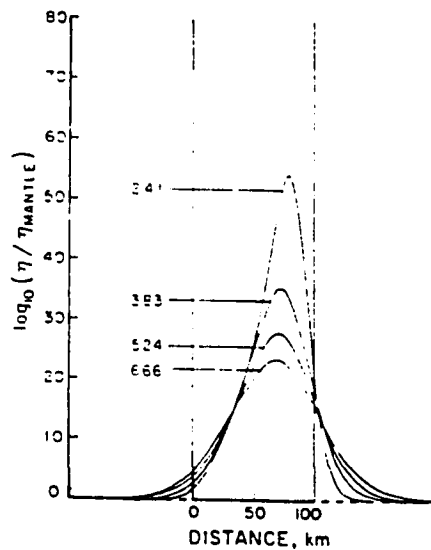


Figure A.2 Viscosity ratio of slab versus the ambient mantle, after Vassiliou and Hager (1988).

We believe that the slab viscosity is probably at least two orders of magnitude higher than the surrounding mantle, based on our previous discussions, this would then make the shear strains parallel to the slab surface occur within the slab to be at least two orders of magnitude lower than those taken up by the ambient mantle. An order of magnitude estimate of the shear deformation in the mantle induced by the subduction process can be done by noting that the shear strain-rate scales as (v/R) where v is the convergence rate and R is the curvature of the slab (Davis, 1984). This yields a strain-rate value of the order of 10^{-14} which would then give a 10^{-16} shear strain rate within the slab. As shown in Chapter III, IV and V, this value is usually at least one order of magnitude lower than the in-plane deformation that we are interested in, this then justify our ignoring the shear deformation that is parallel to slab surface.

In fact, the shear strain rate is one important mechanism at least in the dynamics of the subduction (dynamically, it relates to the so called *viscous drag* that usually enter into the force balance of the subduction process). The point we are making here is that first of all, it can be shown that this deformation is relatively unimportant as compared to the in-plane deformation; secondly, this part of the deformation relies on the variation of the flow away from the mid-surface of the slab where we evaluate the membrane deformation, not on the surface-flow itself. In other words, it is not directly constrained by the geometric configuration c.f the slab. Since our goal in this study is to quantify the least amount of deformation required simply by the geometric configuration of the slab. It is then reasonable for us to first focus on the membrane deformation as discussed in chapter 2 before any attempt to explore the more complete picture of the dynamics of the subduction process.

Appendix B. Notes on the non-linear optimization.

The scheme used to proceed with iterations on the non-linear optimization of this study as described in chapter 2 is essentially a more general form of the popular Levenberg-Marquardt's method widely used in attacking non-linear least-square problems. There are lots of well established schemes for general multidimensional optimization problems, usually, to choose one of this schemes depends on how expensive to evaluate the function and its first and second derivatives and the numerical robustness and the efficiency to converge, e.g. steepest descent method, conjugate gradient methods like Plak-Ribiere scheme and Quasi-Newton methods (also known as the variable metric methods) like: DFP (Davidon-Fletcher-Powell) scheme and BFGS (Broyden-Fletcher-Goldfarb-Shanno) scheme all needs only informations on the first derivative of the target functions being minimized. Gill et. al. (1981) and Scales (1985) give excellent review on this topic. In the formulation described in chapter 2, the second derivatives of the dissipation power functional with respect to the parameters of flow field and slab geometry (i.e. the Hessian matrix) can be evaluated analytically, it's also very sparse as a result of proper node labelling of the finite element mesh and it doesn't cost too much extra work along with the computation of the the dissipation power functional value. Since second derivative method (methods that use the knowledge of the Hessian matrix) are usually more reliable and take fewer iterations to converge (Murray, 1972), It is then an obvious choice in this study to choose an optimization scheme among this particular group.

To minimize a function $F(\vec{x})$ in the n-dimensional Euclidean space; $\vec{x} \in E^n$. Define the gradient vector $\vec{g} = \vec{\nabla} F$; and the Hessian matrix $H = \vec{\nabla} \vec{\nabla} F$. If $F(\vec{x})$ is a general functional then the $\vec{\nabla}$ operation is the Frechet derivatives. Notice that rewriting the dissipation power functional I of the form in Section 2.4.1 to Equation (D.2a) enables I to be analytically Frechet differentiable. General iterative schemes to solve this optimization problem is then; For the k -th iteration:

$$F_k = F(\vec{x}_k)$$

update \vec{x} by $\vec{x}_{k+1} = \vec{x}_k + \alpha_k \vec{p}_k$

such that $F_{k+1} < F_k$ _____(B.1)
 where α_k is a scalar, \vec{p}_k is the new search direction.

Method of steepest descent

Since by Taylor's expansion,

$$F(\vec{x}_k + \alpha_k \vec{p}_k) \approx F(\vec{x}_k) + \alpha_k \vec{g}_k^T \vec{p}_k \quad \text{_____ (B.2)}$$

For $\alpha_k > 0$, the necessary condition for (B.1) to be true is then

$$\vec{g}_k^T \vec{p}_k < 0$$

the obvious choice is then

$$\vec{p}_k = -\vec{g}_k$$

This simple and stable scheme unfortunately has a very slow rate of convergence for general functions. In fact, only if in the vicinity of a strong local minima of $F(\vec{x})$ can be approximated by

$$F(\vec{x}) \approx \frac{\beta}{2} \vec{x}^T \mathbf{I} \vec{x} + \vec{b}^T \vec{x}, \quad \beta \text{ is a scalar, } \mathbf{I} \text{ is the identity matrix.} \quad \text{_____ (B.3)}$$

that the steepest descent direction would be pointing to the minima (say the direction \vec{c}).

In Figure B.1, the more ellipsoidal the contours of F may be, the more would the direction of steepest descent be biased away from the direction \vec{c} and the slower the convergence. Only when (B.3) is true, the contour will tend to be hyperspherical and the steepest descent direction coincides with \vec{c} .

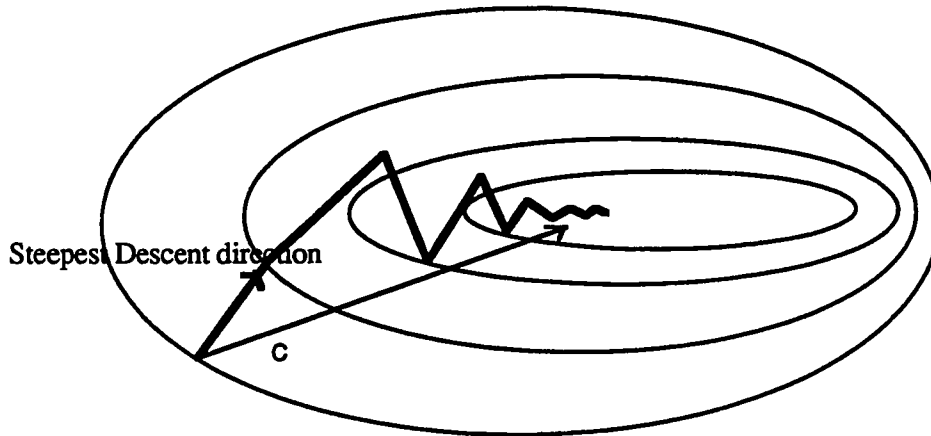


Figure B.1 Zigzag path of the steepest descent direction (the bold line) on a quadratic function. \mathbf{c} is the direction pointing to the minima.

Newton's method

All second derivative methods are basically variants of Newton's method. It is designed to take advantage of the knowledge on Hessian matrix to achieve quadratic termination, and in a sense, it is an improvement on the drawbacks of the steepest descent method mentioned above. During the k -th iteration, the search direction is defined by

$$\vec{\mathbf{p}}_k = -\mathbf{H}_k^{-1} \vec{\mathbf{g}}_k \quad \text{_____} \quad (\text{B.4})$$

which is then a steepest descent direction for the norm $\|\vec{\mathbf{x}}\| = \vec{\mathbf{x}}^T \mathbf{H} \vec{\mathbf{x}}$. In other words, near the vicinity of a local minima, $F(\vec{\mathbf{x}})$ is approximate by

$$F(\vec{\mathbf{x}}) \approx \frac{1}{2} \vec{\mathbf{x}}^T \mathbf{H} \vec{\mathbf{x}} + \mathbf{b}^T \vec{\mathbf{x}} \quad \text{_____} \quad (\text{B.5})$$

Clearly, if \mathbf{H} is positive definite, then

$$\vec{\mathbf{g}}_k^T \vec{\mathbf{p}}_k = - \vec{\mathbf{g}}_k^T \mathbf{H}^{-1} \vec{\mathbf{g}}_k < 0$$

and $\vec{\mathbf{p}}_k$ is thus a descent direction. Also, by including \mathbf{H} in (B.5) as compared to (B.3), the convergent rate of Newton's method is now of second order if \mathbf{H} is positive definite. Unfortunately, this is not always true. Not only that the positive-definiteness of \mathbf{H} is not guaranteed, it can sometimes be nearly singular for a weak minima or ill-conditioned minima. Also, near a saddle point, $\|\vec{\mathbf{g}}_k\| = 0$, and a new descent direction can not be found by (B.4).

Modified Newton's method

Generally, modified Newton's method try to replace the Hessian matrix by a positive definite matrix whenever the original matrix is not positive definite, and otherwise close to the original matrix. Such algorithms preserve the fast asymptotic rate of convergence of Newton's method near well behaved minima and are otherwise robust and numerically stable. In other words, if we examine the eigenvalue-spectrum of the matrix, the essence of the modification is to alter the small and negative eigenvalues of the Hessian matrix while preserving other eigenvalues to guarantee both the resulting search direction is a proper descent direction and also, the computation is numerically robust.

Gill & Murray's algorithm

Proposed by Gill and Murray (1974), this algorithm first use Cholesky's algorithm to factorize the Hessian matrix:

$$\begin{aligned} \mathbf{H}_k &= \mathbf{L}_k \mathbf{D}_k \mathbf{L}_k^T \\ d_{jj} &= g_{jj} - \sum_{k=1}^{j-1} d_{kk} l_{jk}^2 \\ l_{ij} &= (g_{ij} - \sum_{k=1}^{j-1} d_{kk} l_{ik} l_{jk}) / d_{jj} \end{aligned} \tag{B.6}$$

The descent direction is then calculated by

$$\begin{aligned} \mathbf{L}_k \vec{\mathbf{q}}_k &= -\vec{\mathbf{g}}_k \\ \mathbf{L}_k^T \vec{\mathbf{p}}_k &= \mathbf{D}_k^{-1} \vec{\mathbf{q}}_k \end{aligned} \quad \text{(B.7)}$$

The essence of this algorithm is that (B.6) can only be done for symmetric positive definite matrix. It is straightforward to monitor the value of d_{jj} as the factorization proceed, the non-positiveness of this value indicates that the matrix is not positive definite. Whenever this situation should occur, the corresponding value can be replaced by a small positive number. In the end this is equivalent to perform the factorization on a modified Hessian matrix:

$$\widetilde{\mathbf{H}}_k = \widetilde{\mathbf{L}}_k \widetilde{\mathbf{D}}_k \widetilde{\mathbf{L}}_k^T, \quad \widetilde{\mathbf{H}}_k = \mathbf{H}_k + \mathbf{E}_k$$

where \mathbf{E}_k is a diagonal matrix. As mentioned in Scales (1985), one thing worth noticing is that it is not sufficient for the modified eigenvalues of $\widetilde{\mathbf{H}}_k$ to be merely positive, because it might results in a very large condition number and might produce severe rounding errors in the computation of the descent direction. Gill and Murray (1974) gives details of how to make sure the condition number of the modified Hessian matrix is bounded. It can also be shown that the deviation of the modified matrix from the original Hessian matrix is minimized. Detecting saddle point and provide "negative curvature" direction as an alternative descent direction turns out to be quite trivial when utilizing this method. Overall, the method is robust and computationally efficient. The factorization needs to be done only once for each iteration, and (B.7) can be solved by straight forward forward and backward substitutions.

Levenberg-Marquardt's algorithm

This method was originally proposed to solve non-linear least square problems (Marquardt, 1963) and is sometimes called "ridge regression" or "damped least square method". In this type of optimization problem, the function to be minimized usually take a special form of

$$F(\vec{\mathbf{x}}) = \sum_{i=1}^m f_i^2(\vec{\mathbf{x}}) \quad \text{or} \quad F(\vec{\mathbf{x}}) = \mathbf{f}^T(\vec{\mathbf{x}}) \mathbf{f}(\vec{\mathbf{x}})$$

the gradient vector is then

$$g_j = 2 \sum_{i=1}^m f_i \frac{\partial f_i}{\partial x_j} \quad \text{or} \quad \vec{g}(\vec{x}) = 2\mathbf{J}^T(\vec{x}) \vec{f}(\vec{x})$$

with

$$\mathbf{J}_{m \times n} = \left[\frac{\partial f_i}{\partial x_j} \right]$$

and the Hessian matrix

$$H_{kj} = 2 \sum_{i=1}^m \left[\frac{\partial f_i}{\partial x_k} \frac{\partial f_i}{\partial x_j} + f_i \frac{\partial^2 f_i}{\partial x_k \partial x_j} \right] \quad \text{or} \quad \mathbf{H} = 2 [\mathbf{J}^T \mathbf{J} + \mathbf{S}]$$

with

$$S_{kj} = 2 \sum_{i=1}^m f_i \frac{\partial^2 f_i}{\partial x_k \partial x_j}$$

Newton's method is then

$$(\mathbf{J}_k^T \mathbf{J}_k + \mathbf{S}_k) \vec{p}_k = -\mathbf{J}_k^T \mathbf{f}_k$$

$$\vec{x}_{k+1} = \vec{x}_k + \vec{p}_k \quad \text{_____} \quad (\text{B.8a})$$

the so-called Gauss-Newton method is to ignore \mathbf{S}_k and (B.8a) thus becomes

$$\mathbf{J}_k^T \mathbf{J}_k \vec{p}_k = -\mathbf{J}_k^T \mathbf{f}_k \quad \text{_____} \quad (\text{B.8b})$$

This is the popular least-square solution when we linearize the functions f_i .

The Levenberg-Marquardt's algorithm is to replace (B.8b) by

$$(\mathbf{J}_k^T \mathbf{J}_k + \lambda_k \mathbf{I}) \vec{p}_k = -\mathbf{J}_k^T \mathbf{f}_k \quad \text{_____} \quad (\text{B.9})$$

where \mathbf{I} is the identity matrix and λ_k is some positive scalar.

Similar to Gill & Murray's algorithm, this modification guarantees the positive definiteness of the matrix to be inverted and stabilize the numerical computation when the

matrix is nearly singular. When λ_k is small the decent direction \vec{p}_k is simply the Gauss-Newton vector, as λ_k gets very big, \vec{p}_k is close to the steepest descent direction. Between these two extremes, both $\|\vec{p}_k\|$ and the angle between \vec{p}_k and $-\vec{g}_k$ decrease monotonically as λ_k increases. The most non-trivial part of this method is to determine a proper λ_k for each iteration. Marquardt (1963) proposed to start λ_k at a relatively small value and then increase it by some factor when the descent direction fails to decrease the function value that is being minimized. The disadvantage is that for each trial of a new λ_k the complete Equation (B.9) needs to be solved. This then makes it relatively more expensive than Gill & Murray's algorithm. Methods utilizing truncation of smaller eigenvalues to determine the optimal λ_k had been proposed, but to compute the eigenvalue spectrum of a matrix of large size is too expensive and impractical.

In this study, both the Levenberg-Marquardt's algorithm and the Gill & Murray's algorithm are implemented. The main equations to be solved in each iteration step are always of the form

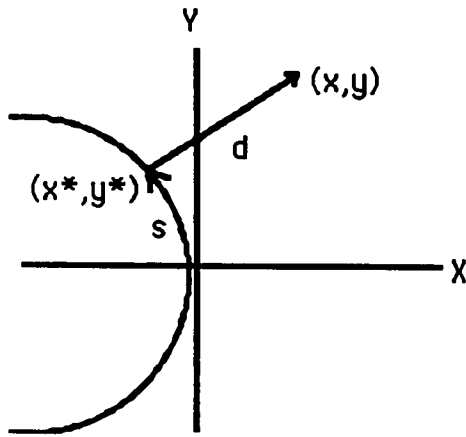
$$(\mathbf{H}_k + \mathbf{E}_k) \vec{p}_k = -\vec{g}_k \quad \text{_____} \quad (\text{B.10})$$

i.e. in implementing the Levenberg-Marquardt's algorithm, instead of linearize the in-plane strain rate tensor w.r.t the nodal variables to utilize Equation (B.9) we use Equation (B.10) since the Hessian matrix \mathbf{H} are analytically available and that it have been reported (Scales, 1985) that only for small residual problem that ignoring the \mathbf{S} matrix are justifiable. Equation (B.10) is then exactly the same as the damping regularization of Equation (2.4.3.a.10a) as described in chapter 2. when \mathbf{E}_k is replaced by $\lambda_k \mathbf{I}$ where \mathbf{I} is the identity matrix. It turns out that the Hessian matrix of this problem are usually not well-behaved in that, during the iteration, positive definiteness of the matrix are usually exceptions rather than regular. Both of the two algorithms thus numerically stabilize the computation. The main difference is that in Levenberg-Marquardt's algorithm, determining the proper λ_k in each step is handled in a more or less brutal force fashion in the sense that you usually start with a small value of λ_k , increase it by certain factor when the resulted search direction fails in finding a new lower value of the functional that is being minimized until the search direction that does reduce the functional value is found and that step of iteration is thus complete. This process of trial and error involves

with solving a big system of equations in each step of trial and is thus relatively expensive. Also, it is still possible to encounter a matrix of very big condition number along the trial process which might then cause overflow problems. The Gill & Murray's algorithm, on the other hand, accomplishes the estimation of the proper \mathbf{E}_k for each iteration during the Cholesky's decomposition, and is done in a single pass. This then makes it more efficient and less expensive. The fact that \mathbf{E}_k is still a diagonal matrix although not of the form $\lambda_k \mathbf{I}$ can be interpreted in the context of the regularization discussed in chapter II as having different weighting on each different variables.

Appendix C. Mesh generation for curved-shape trench

It is quite straightforward to generate triangular grids used in the Finite Element interpolation if the region of interest is of relative simple shape. Since the trench usually takes curved shape, a transformation is devised here so that we can automate the mesh generation process by constructing the mesh in a regular rectangular domain and then by using this transformation to map the grid points to the transformed domain to make the selected boundary of the mesh match the shape of the trench. Suppose we have a curved trench that can be characterized by a single-value function in a chosen coordinate system, i.e. $x=f(y)$. We can then define a new set of coordinate (d,s) for any point (x,y) such that d is the normal distance to the trench and s is the distance along the trench from some reference point.



$$d=\sqrt{\alpha} \quad , \quad \alpha=(x-x^*)^2+(y-y^*)^2$$

$$x^*=f(y^*), \quad f'=\frac{df}{dy} \Big|_{y=y^*}, \quad f''=\frac{d^2f}{dy^2} \Big|_{y=y^*}$$

$$s=\int_0^{y^*} \sqrt{\beta} dy \quad , \quad \beta=\sqrt{1+f'^2}$$

$$D=f''(x^*-x)+(f')^2+1$$

Figure C.1 Configuration and parameters used in mapping a curved boundary into a straight one.

To avoid ambiguity for points located on the concave side of the trench, d cannot be greater than the local radius of curvature of the trench. Fortunately, this is usually true for modelling subducting slabs.

From the definition above, for any function z defined in the x - y domain $z=z(x,y)=z(x(s,d), y(s,d))$, the following expressions can be derived, such that all the

calculations in the (x,y) domain can be done in the (d,s) domain and then be transformed back, this is very useful for complicated trench shapes.

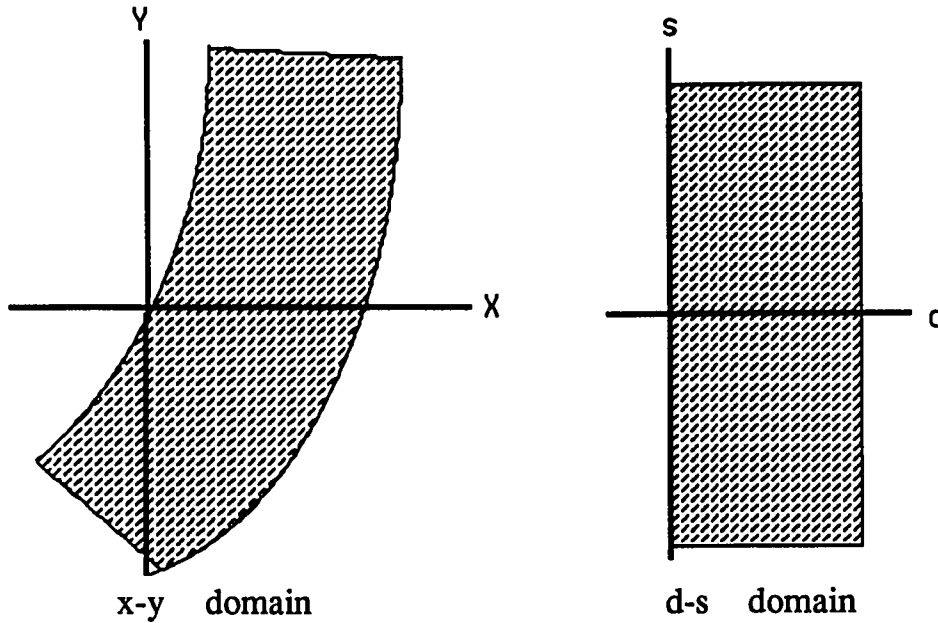


Figure C.2 Mapping between x-y domain and d-s domain

$$\begin{bmatrix} \frac{\partial z}{\partial x} \\ \frac{\partial z}{\partial y} \end{bmatrix} = \begin{bmatrix} R_{11} & R_{12} \\ R_{21} & R_{22} \end{bmatrix} \begin{bmatrix} \frac{\partial z}{\partial d} \\ \frac{\partial z}{\partial s} \end{bmatrix}$$

$$\begin{bmatrix} \frac{\partial^2 z}{\partial x^2} \\ \frac{\partial^2 z}{\partial x \partial y} \\ \frac{\partial^2 z}{\partial y^2} \end{bmatrix} = \begin{bmatrix} T_{11} & T_{12} & T_{13} \\ T_{21} & T_{22} & T_{23} \\ T_{31} & T_{32} & T_{33} \end{bmatrix} \begin{bmatrix} \frac{\partial^2 z}{\partial d^2} \\ \frac{\partial^2 z}{\partial d \partial s} \\ \frac{\partial^2 z}{\partial s^2} \end{bmatrix} + \begin{bmatrix} Q_{11} & Q_{12} \\ Q_{21} & Q_{22} \\ Q_{31} & Q_{32} \end{bmatrix} \begin{bmatrix} \frac{\partial z}{\partial d} \\ \frac{\partial z}{\partial s} \end{bmatrix}$$

with

$$R_{11} = \frac{\partial d}{\partial x} = \frac{x-x^*}{d} = \frac{1}{\beta}$$

$$R_{12} = \frac{\partial s}{\partial x} = f' \frac{\partial s}{\partial y} = \frac{f'\beta}{D}$$

$$R_{21} = \frac{\partial d}{\partial y} = \frac{y-y^*}{d} = \frac{-f}{\beta}$$

$$R_{22} = \frac{\partial s}{\partial y} = \frac{\beta}{D}$$

$$T_{11} = \left(\frac{\partial d}{\partial x}\right)^2 = (R_{11})^2, \quad T_{12} = 2\left(\frac{\partial d}{\partial x}\right)\left(\frac{\partial s}{\partial x}\right) = 2(R_{11})(R_{12}), \quad T_{13} = \left(\frac{\partial s}{\partial x}\right)^2 = (R_{12})^2$$

$$T_{21} = \left(\frac{\partial d}{\partial x}\right)\left(\frac{\partial d}{\partial y}\right) = R_{11}R_{21}, \quad T_{22} = \frac{\partial d}{\partial x}\frac{\partial s}{\partial y} + \frac{\partial d}{\partial y}\frac{\partial s}{\partial x} = R_{11}R_{22} + R_{12}R_{21}, \quad T_{23} = \frac{\partial s}{\partial x}\frac{\partial s}{\partial y} = R_{12}R_{22}$$

$$T_{31} = \left(\frac{\partial d}{\partial y}\right)^2 = (R_{21})^2, \quad T_{32} = 2\left(\frac{\partial d}{\partial y}\right)\left(\frac{\partial s}{\partial y}\right) = 2(R_{21})(R_{22}), \quad T_{33} = \left(\frac{\partial s}{\partial y}\right)^2 = (R_{22})^2$$

$$Q_{11} = \frac{\partial^2 d}{\partial x^2} = \frac{1}{d} - \frac{(f')^2}{Dd} - \frac{(x-x^*)^2}{d^3}, \quad Q_{12} = \frac{\partial^2 s}{\partial x^2} = f'(Q_{22})^2 + \frac{f''}{D}R_{12}$$

$$Q_{21} = \frac{\partial^2 d}{\partial x \partial y} = -\frac{f'}{Dd} - \frac{(x-x^*)(y-y^*)}{d^3}, \quad Q_{22} = \frac{\partial^2 s}{\partial x \partial y} = \frac{1}{D^2} \left\{ \frac{(f')^2 f''}{\beta} - \frac{\beta f'}{D} [f'''(x^*-x) + 3f'f''] + \beta f'' \right\}$$

$$Q_{31} = \frac{\partial^2 d}{\partial y^2} = \frac{1}{D} - \frac{1}{Dd} - \frac{(y-y^*)^2}{d^3}, \quad Q_{22} = \frac{\partial^2 s}{\partial y^2} = \frac{1}{D^2} \left\{ \frac{f' f''}{\beta} - \frac{\beta}{D} [f'''(x^*-x) + 3f'f''] + \beta f'' \right\}$$

Appendix D. Computing matrix α^e and vector β^e .

Let

$$\mathbf{Q} = \begin{bmatrix} 1+z_y^2 & -z_x z_y & z_x \\ -z_x z_y & 1+z_x^2 & z_y \\ z_x & z_y & z_x^2+z_y^2 \end{bmatrix} \quad \text{(D.1a)}$$

and

$$\mathbf{T} = \mathbf{Q}\mathbf{G}\mathbf{Q} + (\mathbf{Q}\mathbf{G}\mathbf{Q})^T \quad \text{(D.1b)}$$

\mathbf{G} is the gradient tensor of the velocity field defined in Equation (2.4.1.4). The projection operator \mathbf{P} as defined in Section 2.3.3 can be written as

$$\mathbf{P} = \mathbf{A}^{-2}\mathbf{Q}$$

where A is the area element of $z(x,y)$ at point (x,y) also defined in Equation (2.4.1.4). The membrane strain rate tensor $\mathbf{D}^{pp}(x,y)$ can now be written as

$$\mathbf{D}^{pp} = (\mathbf{A}^{-4}/2)\mathbf{T}$$

The integrated total dissipation power for power-law rheology with n th power in a single element is thus

$$I = \iint 2^{-(1+\frac{1}{n})} J \, dx dy \quad \text{(D.2a)}$$

with

$$J = A^{-3} \frac{4}{n} [T_{ij}T_{ij} + (T_{ii})^2] \frac{1+1/n}{2}, \quad T_{ii} = T_{11} + T_{22} + T_{33} \quad \text{(D.2b)}$$

As mentioned in Section 2.4.3.c, integration (D.2a) can be done numerically with schemes of the form

$$I = (2^{-1-1/n}) \sum_{i=1}^N w_i J_i$$

where N is the number of sampling points, w_i is the weighting coefficient for the sampling point i and J_i is J defined in Equation (D.2) evaluated at the i -th sampling point.

Since w_i depends only on the shape of the element, we have

$$\frac{\partial I}{\partial \phi_k} = (2^{-1-1/n}) \sum_{i=1}^N w_i \frac{\partial J_i}{\partial \phi_k} \quad \text{(D.3a)}$$

where ϕ_k is one of the 15 degrees of freedom in an element described in Section 2.4.3.c, i.e.

$$\phi^T = [u^1, v^1, z^1, z_x^1, z_y^1, u^2, v^2, z^2, z_x^2, z_y^2, u^3, v^3, z^3, z_x^3, z_y^3]$$

Rewrite

$$J = A^{-3} \frac{4}{n} B^{\frac{1+1/n}{2}}, \quad B = T_{ij} T_{ij} + (T_{ii})^2 \quad \text{(D.3b)}$$

and then

$$\frac{\partial J}{\partial \phi_k} = J \left\{ \left(-3 - \frac{4}{n}\right) A^{-1} \frac{\partial A}{\partial \phi_k} + \left(\frac{1+1/n}{2}\right) B^{-1} \frac{\partial B}{\partial \phi_k} \right\} \quad \text{(D.3c)}$$

Now

$$\frac{\partial A}{\partial \phi_k} = A^{-1} \left(z_x \frac{\partial z_x}{\partial \phi_k} + z_y \frac{\partial z_y}{\partial \phi_k} \right) \quad \text{(D.4)}$$

$$\frac{\partial B}{\partial \phi_k} = 2 \left(T_{ij} \frac{\partial T_{ij}}{\partial \phi_k} + T_{mm} \frac{\partial T_{mm}}{\partial \phi_k} \right) \quad \text{(D.5)}$$

$$\frac{\partial T_{ij}}{\partial \phi_k} = \frac{\partial}{\partial \phi_k} (Q_{is} G_{st} Q_{jt} + Q_{it} G_{st} Q_{js}) \quad \text{(B.6)}$$

$$\frac{\partial Q_{ij}}{\partial \phi_k} = \frac{\partial Q_{ij}}{\partial z_x} \frac{\partial z_x}{\partial \phi_k} + \frac{\partial Q_{ij}}{\partial z_y} \frac{\partial z_y}{\partial \phi_k} \quad (D.7a)$$

From Equation (D.1)

$$\frac{\partial Q_{ij}}{\partial z_x} = \begin{bmatrix} 0 & -z_y & 1 \\ -z_y & 2(z_x) & 0 \\ 1 & 0 & 2(z_x) \end{bmatrix}, \quad \frac{\partial Q_{ij}}{\partial z_y} = \begin{bmatrix} 2(z_y) & -z_x & 0 \\ -z_x & 0 & 1 \\ 0 & 1 & 2(z_y) \end{bmatrix} \quad (D.7b)$$

From the definition of G in Section 2.4.1 and the interpolation scheme summarized in Equation (2.4.3.c.2), we have

$$G = \begin{bmatrix} u_x & v_x & w_x \\ u_y & v_y & w_y \\ 0 & 0 & 0 \end{bmatrix} = \begin{bmatrix} \frac{\partial N^1_i}{\partial x} u_i & \frac{\partial N^1_i}{\partial x} v_i & \frac{\partial N^2_j}{\partial x} w_j \\ \frac{\partial N^1_i}{\partial y} u_i & \frac{\partial N^1_i}{\partial y} v_i & \frac{\partial N^2_j}{\partial y} w_j \\ 0 & 0 & 0 \end{bmatrix} \quad (D.8)$$

where i sum through 1 to 3, j sum through 1 to 6, N^1_i are linear element shape functions, and N^2_j are quadratic shape functions.

By Equations (D.8), (2.4.3.c.2), it is thus straightforward to calculate quantities like $\frac{\partial G_{11}}{\partial \phi_k}$, $\frac{\partial z_x}{\partial \phi_k}$, $\frac{\partial z_y}{\partial \phi_k}$... etc. For example,

$$\frac{\partial G_{11}}{\partial \phi_k} = \frac{\partial}{\partial \phi_k} \left[\frac{\partial N^1_i}{\partial x} u_i \right] = \frac{\partial N^1_i}{\partial x} \frac{\partial u_i}{\partial \phi_k} = \frac{\partial N^1_i}{\partial x} \delta_{ik} = \begin{bmatrix} \frac{\partial N^1_k}{\partial x}, & \text{for } k=1,6,11 \\ 0, & \text{for } k \neq 1,6,11 \end{bmatrix}$$

$$\frac{\partial z_x}{\partial \phi_k} = \frac{\partial N^3_1}{\partial x} \frac{\partial z_1}{\partial \phi_k} = \begin{bmatrix} \frac{\partial N^3_1}{\partial x} \delta_{1k} = \frac{\partial N^3_k}{\partial x}, & \text{for } k=(n_0-1) \times 5 + n_1 + 2, n_0, n_1=1,2,3 \\ 0, & \text{otherwise} \end{bmatrix}$$

These expressions can then be plugged back into Equations (D.6), (D.5), (D.4) and (D.3) successively and complete the computation for β^e .

Similarly, from Equation (D.3), we can compute

$$\begin{aligned}
 \frac{\partial^2 J}{\partial \phi_j \partial \phi_j} &= \frac{\partial}{\partial \phi_j} \left[J \left[\left(-3 \frac{4}{n} \right) A^{-1} \frac{\partial A}{\partial \phi_k} + \left(\frac{1+1/n}{2} \right) B^{-1} \frac{\partial B}{\partial \phi_k} \right] \right] \\
 &= \frac{J}{AB} \left[\frac{B}{A} \left(\frac{3n+4}{n} \right) \left(\frac{4n+4}{n} \right) \frac{\partial A}{\partial \phi_j} \frac{\partial A}{\partial \phi_k} + \frac{A}{B} \left(\frac{1+n}{2n} \right) \left(\frac{1-n}{2n} \right) \frac{\partial B}{\partial \phi_j} \frac{\partial B}{\partial \phi_k} \right. \\
 &\quad \left. - \left(\frac{3n+4}{n} \right) \left(\frac{n+1}{2n} \right) \left(\frac{\partial A}{\partial \phi_j} \frac{\partial B}{\partial \phi_k} + \frac{\partial B}{\partial \phi_j} \frac{\partial A}{\partial \phi_k} \right) \right. \\
 &\quad \left. - \left(\frac{3n+4}{n} \right) B \frac{\partial^2 A}{\partial \phi_j \partial \phi_k} + \left(\frac{n+1}{2n} \right) A \frac{\partial^2 B}{\partial \phi_j \partial \phi_k} \right] \quad \text{_____ (D.9)}
 \end{aligned}$$

Also, from Equation (D.4)

$$\begin{aligned}
 \frac{\partial^2 A}{\partial \phi_j \partial \phi_k} &= \frac{\partial}{\partial \phi_j} \left[A^{-1} \left(z_x \frac{\partial z_x}{\partial \phi_k} + z_y \frac{\partial z_y}{\partial \phi_k} \right) \right] \\
 &= A^{-1} \left[- \frac{\partial A}{\partial \phi_j} \frac{\partial A}{\partial \phi_k} + z_x \frac{\partial^2 z_x}{\partial \phi_j \partial \phi_k} + z_y \frac{\partial^2 z_y}{\partial \phi_j \partial \phi_k} \right. \\
 &\quad \left. + \frac{\partial z_x}{\partial \phi_j} \frac{\partial z_x}{\partial \phi_k} + \frac{\partial z_y}{\partial \phi_j} \frac{\partial z_y}{\partial \phi_k} \right] \quad \text{_____ (D.10)}
 \end{aligned}$$

From Equation (D.5),

$$\begin{aligned}
 \frac{\partial^2 B}{\partial \phi_j \partial \phi_k} &= 2 \frac{\partial}{\partial \phi_j} \left(T_{pq} \frac{\partial T_{pq}}{\partial \phi_k} + T_{mm} \frac{\partial T_{nn}}{\partial \phi_k} \right) \\
 &= 2 \left[\frac{\partial T_{pq}}{\partial \phi_j} \frac{\partial T_{pq}}{\partial \phi_k} + T_{pq} \frac{\partial^2 T_{pq}}{\partial \phi_j \partial \phi_k} + \frac{\partial T_{mm}}{\partial \phi_j} \frac{\partial T_{nn}}{\partial \phi_k} + T_{mm} \frac{\partial^2 T_{nn}}{\partial \phi_j \partial \phi_k} \right] \quad \text{_____ (D.11)}
 \end{aligned}$$

From Equation (D.6),

$$\frac{\partial^2 T_{pq}}{\partial \phi_j \partial \phi_k} = \frac{\partial^2}{\partial \phi_j \partial \phi_k} (Q_{ps} G_{st} Q_{tq} + Q_{qs} G_{st} Q_{tp})$$

and

$$\begin{aligned} \frac{\partial^2}{\partial \phi_j \partial \phi_k} (Q_{ps} G_{st} Q_{tq}) &= \frac{\partial Q_{ps}}{\partial \phi_j} \frac{\partial G_{st} Q_{tq}}{\partial \phi_k} + \frac{\partial Q_{ps}}{\partial \phi_k} \frac{\partial G_{st} Q_{tq}}{\partial \phi_j} \\ &+ \frac{\partial Q_{ps}}{\partial \phi_j} G_{st} \frac{\partial Q_{tq}}{\partial \phi_k} + \frac{\partial Q_{ps}}{\partial \phi_k} G_{st} \frac{\partial Q_{tq}}{\partial \phi_j} \\ &+ Q_{ps} \frac{\partial G_{st}}{\partial \phi_j} \frac{\partial Q_{tq}}{\partial \phi_k} + Q_{ps} \frac{\partial G_{st}}{\partial \phi_k} \frac{\partial Q_{tq}}{\partial \phi_j} \\ &+ \frac{\partial^2 Q_{ps}}{\partial \phi_j \partial \phi_k} G_{st} Q_{tq} + Q_{ps} \frac{\partial^2 G_{st} Q_{tq}}{\partial \phi_j \partial \phi_k} + Q_{ps} G_{st} \frac{\partial^2 Q_{tq}}{\partial \phi_j \partial \phi_k} \end{aligned}$$

$$\frac{\partial^2 Q_{ps}}{\partial z_x^2} = \begin{bmatrix} 0 & 0 & 0 \\ 0 & 2 & 0 \\ 0 & 0 & 2 \end{bmatrix}, \quad \frac{\partial^2 Q_{ps}}{\partial z_x \partial z_y} = \begin{bmatrix} 0 & -1 & 0 \\ -1 & 0 & 0 \\ 0 & 0 & 0 \end{bmatrix}, \quad \frac{\partial^2 Q_{ps}}{\partial z_y^2} = \begin{bmatrix} 2 & 0 & 0 \\ 0 & 0 & 0 \\ 0 & 0 & 2 \end{bmatrix}$$

$$\frac{\partial^2 Q_{pq}}{\partial \phi_j \partial \phi_k}, \quad \frac{\partial^2 G_{pq}}{\partial \phi_j \partial \phi_k}$$

We can thus compute both

For example, if both j, k are among 3,4,5,8,9,10,13,14,15, i.e. ϕ_j, ϕ_k are both parameters concerning z interpolation (z, z_x, z_y) then

$$\begin{aligned} \frac{\partial^2 Q_{pq}}{\partial \phi_j \partial \phi_k} &= \frac{\partial^2 Q_{pq}}{\partial z_x^2} \left(\frac{\partial z_x}{\partial \phi_j} \frac{\partial z_x}{\partial \phi_k} \right) + \frac{\partial^2 Q_{pq}}{\partial z_y^2} \left(\frac{\partial z_y}{\partial \phi_j} \frac{\partial z_y}{\partial \phi_k} \right) \\ &+ \frac{\partial^2 Q_{pq}}{\partial z_x \partial z_y} \left(\frac{\partial z_x}{\partial \phi_j} \frac{\partial z_y}{\partial \phi_k} + \frac{\partial z_y}{\partial \phi_j} \frac{\partial z_x}{\partial \phi_k} \right) \end{aligned}$$

otherwise,

$$\frac{\partial^2 Q_{pq}}{\partial \phi_j \partial \phi_k} = 0$$

Again, successively plug these expression back into Equation (D.9), the computation of α^e are complete similar to expression (D.3a).

Vita

Chiao, Ling-Yun

Date of birth: 8 July 1955

Place of birth: Kaoshiung,
Taiwan, Republic of China

Educational background:

Kaoshiung Senior High School, Kaoshiung, Taiwan, R.O.C., diploma, June 1973

National Taiwan University, Taipei, Taiwan, R.O.C., B.S. Geology, June 1977

National Taiwan University, Taipei, Taiwan, R.O.C., M.S. Geophysics, June 1981

University of Washington, Seattle, Washington, Ph.D. Geophysics, October 1991